Turbulent flows over canopies

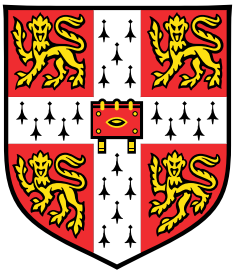

Akshath Sharma

Department of Engineering
University of Cambridge

This dissertation is submitted for the degree of
Doctor of Philosophy

Churchill College

July 2019

Declaration

I hereby declare that except where specific reference is made to the work of others, the contents of this dissertation are original and have not been submitted in whole or in part for consideration for any other degree or qualification in this, or any other university. This dissertation is my own work and contains nothing which is the outcome of work done in collaboration with others, except as specified in the text and Acknowledgements. This dissertation contains fewer than 65,000 words including appendices, bibliography, footnotes, tables and equations and has fewer than 150 figures.

Akshath Sharma
July 2019

Acknowledgements

I want to express my deepest gratitude towards my supervisor Dr Ricardo García-Mayoral, for his support throughout my time here. His guidance and knowledge have been pivotal in shaping my work and my thinking. I feel truly fortunate to have done my PhD under his supervision.

I would also like to thank all the members of the Fluids group, past and present, for making my time at the office truly memorable, especially Andrea, Antoine, Francesco, Francisco, James, Kshitij, and those in Ricardo's group Chris, Nabil, Garazi, Joe, Wenxiong and Dharma. I am forever indebted to Garazi for her help, both personal and professional, throughout my time here.

I want to thank my parents for their unwavering support and motivation for all my endeavours. A special mention to Shambhavi for bearing with me for as long as she has.

Finally, I would also like to acknowledge the Cambridge, Commonwealth, European and International Trust for providing me with the award that allowed me to pursue my studies at Cambridge.

Abstract

In this thesis, turbulent flows over canopies in the sparse and dense regimes are examined using direct numerical simulation. The term 'canopy' is used to refer to tall roughness elements in the flow. Sparse canopies typically have large element spacings and allow turbulent eddies to penetrate between the elements, whereas dense canopies have small spacings and preclude the penetration of turbulent eddies within them.

In sparse canopies, we consider layouts with rigid elements and spacings larger than the characteristic scales of near-wall turbulence, $s^+ \gtrsim 100$. We focus on the effect of the canopy on the background turbulence, the part of the flow that remains once the element-induced flow is filtered out. In channel flows, the distribution of the total stress is linear with height. Over smooth walls, the total stress is only the 'fluid stress' τ_f, the sum of the viscous and the Reynolds shear stresses. In canopies, in turn, there is an additional contribution from the canopy drag, which can dominate within. We find that, for sparse canopies, the ratio of the viscous and the Reynolds shear stresses in τ_f at each height is similar to that over smooth-walls, even within the canopy. From this, a height-dependent scaling based on τ_f is proposed. Using this scaling, the background turbulence within the canopy shows similarities with turbulence over smooth walls. This suggests that the background turbulence scales with τ_f, rather than with the conventional scaling based on the total stress. This effect is essentially captured when the canopy is substituted by a drag force that acts on the mean velocity profile alone, aiming to produce the correct τ_f, without the discrete presence of the canopy elements acting directly on the fluctuations. The proposed mean-only forcing is shown to produce better estimates for the turbulent fluctuations compared to a conventional, homogeneous-drag model. The present results thus suggest that a sparse canopy acts on the background turbulence primarily through the change it induces on the mean velocity profile, which in turn sets the scale for turbulence, rather than through a direct interaction of the canopy elements with the fluctuations. The effect of the element-induced flow, however, requires the representation of the individual canopy elements.

The dense canopies studied consist of rigid, prismatic filaments with small spacings. The effect of the height and spacing of the canopy elements on the flow is studied. The flow is composed of an element-coherent, dispersive flow and an incoherent flow, which includes contributions from the background turbulence and from the flow arising from the

Kelvin–Helmholtz-like, mixing-layer instability typically reported over dense canopies. For the present canopies, with spacings $s^+ \approx 3$–50, the background turbulence is essentially precluded from penetrating within the canopy. As the elements are 'tall', with height-to-spacing ratios $h/s \gtrsim 1$, the roughness sublayer of the canopy is determined by their spacing, extending to $y \approx 2$–$3s$ above the canopy tips. The dispersive velocity fluctuations are observed to also depend mainly on the spacing, and are small deep within the canopy, where the footprint of the Kelvin–Helmholtz-like instability dominates. The instability is governed by the canopy drag, which sets the shape of the mean velocity profile, and thus the shear length near the canopy tips. For the tall canopies considered here, this drag is governed by the element spacing and width, that is, the planar layout of the canopy. The mixing length, which determines the lengthscale of the instability, is essentially the sum of its height above and below the canopy tips. The former remains roughly the same in wall-units and the latter is linear with s for all the canopies considered. For very small element spacings, $s^+ \lesssim 10$, the elements obstruct the fluctuations and the instability is inhibited. Within the range of s^+ of the present canopies, the obstruction decreases with increasing spacing and the signature of the Kelvin–Helmholtz-like rollers intensifies. For sparser canopies, however, the intensification of the instabilities ceases as the assumption of a spatially homogeneous mean flow breaks down. For the present, dense configurations, the canopy depth also has an influence on the development of the instability. For shallow canopies, $h/s \sim 1$, the lack of depth blocks the Kelvin–Helmholtz-like rollers. For deep canopies, $h/s \gtrsim 6$, the rollers do not perceive the bottom wall and the effect of the canopy height on the flow saturates.

Two approaches based on linear stability analysis are proposed to capture the Kelvin–Helmholtz-like instability over dense canopies. The first approach models the canopy as an anisotropic permeable substrate whose wall-normal permeability, K_y, is larger than its streamwise permeability, K_x. This model predicts that the instability over canopies is governed by the geometric mean of the two permeabilities, $\sqrt{K_x^+ K_y^+}$. We also use this model to study the effect of the mean inclination of the canopy elements on the instability. The second approach models the canopy using a drag force in the momentum equation. This model shows that two competing effects, originating from the canopy drag, govern the growth of the instability. Increasing the canopy drag results in a stronger inflection point in the mean velocity profile, which enhances the instability, while at the same time, it also inhibits fluctuations within the canopy, suppressing the instability. We also analyse the stability of the mean profiles obtained from the DNS of dense canopy flows. Using this analysis, we show that the shear-layer thickness within the canopy, which determines the streamwise wavelength of the instability, also scales with the element spacing.

Table of contents

Nomenclature

Roman Symbols

a_i, b_i Coefficients to determine wall-normal grid stretching

C_{dc} Drag coefficient used for representing permeable canopy elements

C_{dh}, C_x Homogenised streamwise canopy drag coefficient

C_i Homogenised canopy drag coefficient in the i^{th} direction

C_y Homogenised wall-normal canopy drag coefficient

D Discretised divergence operator, or first derivative with respect to y

D Mean canopy drag force

G Discretised gradient operator

h Height of canopy

i $\sqrt{-1}$

j Wall-normal grid index

$\boldsymbol{K}$ Permeability tensor

K_{ij} $(i,j)^{th}$ element of the permeability tensor $\boldsymbol{K}$

$k_x k_z E_{uu}$ Premultiplied spectral energy density of streamwise fluctuations

$k_x k_z E_{uv}$ Premultiplied spectral energy density of Reynolds shear stresses

$k_x k_z E_{vv}$ Premultiplied spectral energy density of wall-normal fluctuations

$k_x k_z E_{ww}$ Premultiplied spectral energy density of spanwise fluctuations

K_x Streamwise permeability

k_x Streamwise wavenumber

K_y	Wall-normal permeability
k_z	Spanwise wavenumber
L	Discretised Laplacian operator
l_h	Height of the head of the T-shaped sparse canopy elements
L_p	Penetration depth of flow within the canopy
L_s	Shear-layer thickness, $U/(\mathrm{d}U/\mathrm{d}y)$
l_s	Height of the stem of sparse canopy element
l_x	Streamwise width of sparse canopy element
L_{xz}	Discretised Laplacian operator in streamwise and spanwise directions
L_y	Discretised Laplacian operator in wall-normal direction
l_z	Spanwise width of sparse canopy element
N	Discretised non-linear operator
N	Number of wall-normal grid points
N_c	Number of wall-normal grid points within the canopy region
N_x	Number of streamwise grid points
n_x	Number of streamwise grid points in one periodic element of the canopy
N_z	Number of spanwise grid points
n_z	Number of spanwise grid points in one periodic element of the canopy
P	Mean pressure
p	Pressure
Re	Bulk Reynolds number, $U_b\delta/\nu$
Re_τ	Friction Reynolds number, $u_\tau\delta/\nu$
s	Canopy element spacing
t	Time
$\boldsymbol{u}$	Velocity vector with associated components u, v and w

$\mathbf{u}_*$ Intermediate velocity vector in fractional step method

U Mean streamwise velocity

u Streamwise velocity

U_b Channel bulk velocity

u_τ Friction velocity

v Wall-normal velocity

w Spanwise velocity

w Width of dense canopy elements

x Streamwise coordinate

y Wall-normal coordinate

y_c Location of the peak of the vorticity gradient in smooth-wall flows

z Spanwise coordinate

Greek Symbols

α Streamwise wavenumber

α_k Runge–Kutta coefficient for the implicit viscous term

β Impedance coefficient relating pressure and wall-normal velocity

β_k Runge–Kutta coefficient for the explicit viscous term

δ Channel height/half-height

Δt Timestep

Δx Streamwise grid resolution

Δy Wall-normal grid resolution

Δz Spanwise grid resolution

γ_k, ζ_k Runge–Kutta coefficients for the advective term

∇ Gradient operator

κ_{Br} Equivalent permeability for substrate governed by Brinkman's equation

κ_{Da} Equivalent permeability for substrate governed by Darcy's equation

λ_f Roughness frontal density

λ_p Roughness plan area ratio

λ_x Streamwise wavelength

λ_z Spanwise wavelength

ν Kinematic viscosity

ν_T Turbulent eddy viscosity from Cess (1958)

$\widetilde{\nu}$ Effective macroscale viscosity

ω Angular frequency of a wave

ω_i Growth rate of a wave, imaginary part of ω

ω_r Phase velocity of a wave, real part of ω

ϕ Change in pressure

ρ Density

τ Total stress

τ_f Sum of viscous and Reynolds shear stresses

τ_w Wall shear stress

θ Angle of rotation of canopy element

Superscripts

$(\cdot)'$ Full fluctuating component, or first derivative with respect to y

$(\cdot)''$ Background turbulent fluctuating component

$(\cdot)^*$ Variable scaled in local friction units

$(\cdot)^n$ Timestep index

$(\cdot)^+$ Variable scaled in friction units

Subscripts

$(\cdot)_{max}$ Maximum value

$(\cdot)_k$ Runge–Kutta substep index

Other Symbols

$\hat{(\cdot)}$ Variable in Fourier space

$\langle(\cdot)\rangle$ Quantity averaged in x and z

$\overline{(\cdot)}$ Quantity averaged in x, z and t

$\tilde{(\cdot)}$ Element-induced component

Acronyms / Abbreviations

CFL Courant–Friedrichs–Lewy number

DNS Direct Numerical Simulation

K–H Kelvin–Helmholtz

QS Quasi-streamwise

Chapter 1

Introduction

Canopy flows are ubiquitous in both natural and artificial settings. Consequently, the study of canopy flows has wide-ranging applications. Perhaps the most extensively studied examples of these flows are those through vegetation, such as crops and forests. The applications of these studies include characterisation of the exchange of carbon-dioxide between vegetation layers and the atmosphere (Baldocchi *et al.*, 2001), preventing crop loss due to wind damage (de Langre, 2008), weather forecasting (Barlow & Coceal, 2008), and even providing better representations of plant motion in animated films (Diener *et al.*, 2006). Canopy flows are also relevant for engineering applications. Canopy-like devices such as pin-fins are used for cooling electronic components and in heat exchangers (Bejan & Morega, 1993). Recently, prototypes of piezoelectric filament mats for energy harvesting have also been developed (Slingsby, 2018). Some of the examples of canopies mentioned above are portrayed in figure 1.1, which also illustrates that canopies can span a wide range of sizes and flow conditions. In addition, the canopy parameters relevant for engineering applications may also be very different from those of the widely studied natural canopies. Canopies can be broadly classified into three regimes dense, intermediate and sparse (Nepf, 2012). Sparse canopies generally have elements that are widely spaced and behave like independent obstacles in the flow. Dense canopies, on the other hand, have closely packed elements, which act on the overlying flow in a homogeneous fashion. The intermediate, or transitional, regime lies between these two extremes. Although there is no fixed parameter to classify canopies into these regimes effectively, there are certain typical flow features associated with dense and sparse canopies. The flow over dense canopies is characterised by the presence of a Kelvin–Helmholtz-like, mixing-layer instability (Raupach *et al.*, 1996). Sparse canopies, however, do not exhibit this mixing-layer type behaviour (Poggi *et al.*, 2004).

In the present work, we analyse turbulent flows over canopies using direct numerical simulation. The aim is to understand how canopies in the sparse and dense regimes affect turbulence within and above them and identify the key canopy parameters that govern their interaction. For flows over sparse canopies, we separate the contribution of the element-

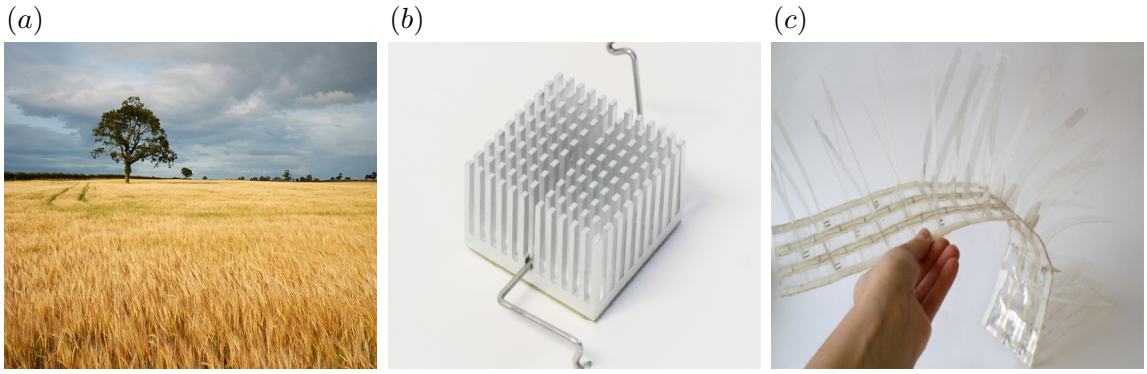

FIGURE 1.1 Examples of natural and artificial canopies. (a) natural crop canopy[1], (b) pin-fin heat sink[2]and (c) piezoelectric filaments[3].

induced flow from the remaining background turbulence and study them separately. Particular emphasis is placed on the properties of the background-turbulence fluctuations. In dense canopy flows, we also explore the effect of the canopy parameters on the Kelvin–Helmholtz-like instability and propose simplified models based on linear stability analysis to capture them. These instabilities are known to increase mixing of the flow within and over the canopy and may, therefore, be beneficial for the engineering applications mentioned above.

In the remainder of this chapter, we provide a summary of prior research into turbulent flows over canopies and provide further details about the particulars of the present work. In §1.1, we discuss wall-bounded turbulent flows in the near-wall region. In §1.2, we discuss the existing literature on sparse and dense canopy flows. In §1.3, we discuss studies on linear stability analysis of canopy flows. The aims and the structure of the thesis are discussed in §1.4.

1.1 Wall-bounded turbulent flows

Turbulent flows in the vicinity of walls have different characteristics compared to flows far away from any boundaries (Tennekes & Lumley, 1972). The no-slip and impermeability conditions at the wall in viscous flows result in the near-wall turbulence being highly anisotropic. In such flows, four major regions can be identified based on the distance from the wall. Very close to the wall is the viscous sublayer, where the size of the turbulent eddies scales with the viscous lengthscale, ν/u_τ, where ν is the fluid kinematic viscosity and $u_\tau = \sqrt{\tau_w/\rho}$ is the friction velocity based on the wall shear-stress, τ_w. Variables scaled with the viscous lengthscale and the wall friction velocity are said to be in wall or friction units and are indicated by the superscript '+'. The size of the viscous sublayer is $y^+ \lesssim 5$, where y is the wall-normal coordinate. In the region $5 < y^+ \lesssim 100$, both viscous and inertial effects are

[1] "Cornfield tree" by nagillum, licensed under CC BY 2.0
[2] wikipedia.org/wiki/Heat_sink
[3] "Moya Power" by Charlotte Slingsby, image from jamesdysonawards.com

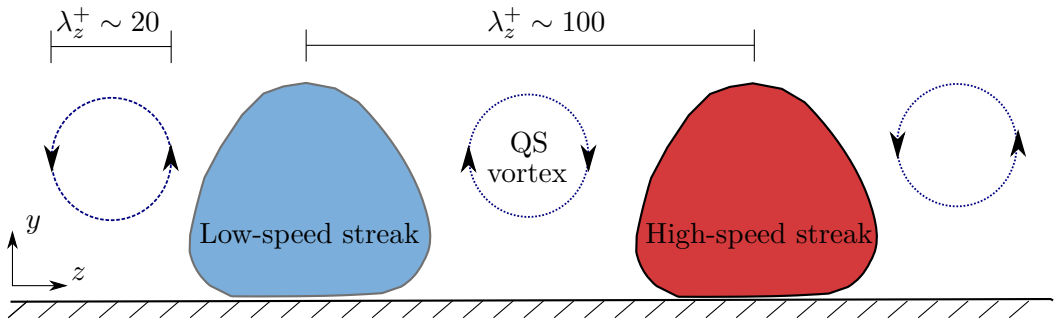

FIGURE 1.2 Schematic of structures associated with the near-wall turbulence cycle, adapted from Gómez-de-Segura (2019).

important, and this region is termed as the buffer layer. Above the buffer layer, in the region $80 < y^+ \lesssim 0.3\delta$, the size of the turbulent eddies scales with their distance from the wall. This region is the self-similar, logarithmic layer. The viscous sublayer, buffer layer and the beginning of the logarithmic layer are together referred to as the inner layer. Above the logarithmic layer, in the outer layer, the size of the turbulent eddies scales with the channel height, δ. The velocity scale for all these regions is set by the wall-friction velocity, u_τ. It may be noted here that variables scaled using the channel height, δ and the bulk velocity, U_b are said to be in 'outer units'. The flow in the viscous and buffer region in smooth channels has been extensively studied, and a detailed examination of the flow dynamics can be found in Jiménez & Pinelli (1999), Schoppa & Hussain (2002), Jiménez (2013), and the recent review by Jiménez (2018). In this region, the streamwise flow is organised mainly in the form of alternating high- and low-speed streaks, with streamwise and spanwise extents of $\lambda_x^+ \approx 1000$ and $\lambda_z^+ \approx 50$, respectively (Kline *et al.*, 1967; Smith & Metzler, 1983). The average spanwise separation of the streaks is of the order of a hundred wall-units. These streaks are flanked on either side by quasi-streamwise vortices that have a spanwise diameter of $\lambda_z^+ \approx 20$ (Blackwelder & Eckelmann, 1979), as illustrated in figure 1.2. The streaks and quasi-streamwise vortices are together responsible for the self-sustaining, near-wall cycle. The vortices bring in high-momentum fluid towards the wall to sustain the high-speed streak, and displace the low momentum fluid away from the wall sustaining the low-speed streak. The exact mechanism of their formation and regeneration is still somewhat unclear (Jeong *et al.*, 1997; Jiménez & Pinelli, 1999). Jiménez & Pinelli (1999) showed through a series of conceptual numerical simulations that the flow in the inner layer, $0 < y^+ \lesssim 60$, can be sustained independent of the outer layer flow, and vice versa. The streamwise coherent streaks still exist in the logarithmic region, but their streamwise and spanwise extent is larger than that of the near-wall streaks, and the vortices in the logarithmic region have a larger range of scales than those in the buffer and viscous layers (Jiménez, 2013).

Several studies have shown that complex surfaces with small texture sizes, of the order of tens of wall-units, generally interact with and modify the turbulent structures in the inner layer. Examples of these textures include conventional rough surfaces (Jiménez, 2004; Orlandi & Leonardi, 2006; Flack *et al.*, 2007; Abderrahaman-Elena *et al.*, 2019), riblets (García-Mayoral & Jiménez, 2011; García-Mayoral *et al.*, 2019) and anisotropic permeable substrates (Gómez-de-Segura & García-Mayoral, 2019). Roughness elements with very small sizes do not have a noticeable effect on the overlying turbulence, which remains smooth-wall-like for roughness heights up to $h^+ \lesssim 5$ (Nikuradse, 1933; Raupach *et al.*, 1991; Jiménez, 2004). Such rough surfaces are termed as 'hydraulically smooth'. Larger roughness elements cause an increase in the drag experienced by the overlying flow (Nikuradse, 1933) and also result in a modification of the near-wall turbulence dynamics (Jiménez, 2004; Flores & Jiménez, 2006; Flack *et al.*, 2007; Abderrahaman-Elena *et al.*, 2019). Flores & Jiménez (2006) studied the effect of introducing sinusoidal perturbations at the wall, which mimicked the behaviour of roughness on the overlying flow. They observed that the applied perturbations caused the disruption of streaks, which caused a reduction in the intensity of the streamwise fluctuations in the near-wall region. The result of these changes is often reported as the near-wall turbulence over roughness becoming more isotropic (Ligrani & Moffat, 1986; Orlandi & Leonardi, 2006). The effect of the roughness elements on the overlying flow is observed to extend up to a few roughness heights above the elements. This height is called the roughness sublayer, and the flow above it resembles canonical, smooth-wall flow in accordance with Townsend's outer-layer similarity theory (Townsend, 1976; Raupach *et al.*, 1991). The height of the roughness sublayer over cubical and sand-grain roughness has been estimated to be $y = 2\text{–}4h$ (Flack *et al.*, 2007; Abderrahaman-Elena *et al.*, 2019). However, several studies have observed that certain roughness geometries can perturb the flow beyond this height as well (Jiménez, 2004; Leonardi & Castro, 2010; Placidi & Ganapathisubramani, 2018).

1.2 Turbulent flows over canopies

Natural canopy flows have been extensively studied over the past few decades. In one of the early canopy studies, Inoue (1955) noted patches of rice crops bending in unison in response to the wind blowing over them. Inoue (1955) used the term *honami* to refer to the coherent bending. A subsequent wind tunnel experiment of model crops performed by Finnigan & Mulhearn (1978) suggested that *honami* was an imprint of large, coherent flow structures in the atmospheric boundary layer passing over the crops. Raupach *et al.* (1996) drew a connection between mixing-layer flows and canopy flows. They noted that, like mixing-layer flows, canopy flows also exhibited an inflection point in the mean velocity profile at the canopy-tip plane, which could result in the formation of a Kelvin–Helmholtz-like instability over them and cause *honami*. The formation of this instability enhances momentum exchange between the free-flow and canopy regions, and consequently, results in increased mixing

and drag (Raupach *et al.*, 1996; Finnigan, 2000; Nepf, 2012). Canopies with large element spacings, however, do not exhibit a noticeable signature of this instability (Poggi *et al.*, 2004; Pietri *et al.*, 2009; Huang *et al.*, 2009; Nepf, 2012). Based on experimental observations of flows over model aquatic canopies, Nepf (2012) provided an approximate classification for canopies into three regimes based on their roughness frontal density, λ_f, which is the ratio of the frontal area of the canopy elements and the plan area of the canopy bed. Nepf (2012) proposed that dense canopies had large roughness densities, $\lambda_f > 0.1$, and exhibited a strong signature of the Kelvin–Helmholtz-like instability. Canopies with $\lambda_f < 0.1$ were observed by Nepf (2012) to lie in the sparse regime and not trigger the instability in the flow. Canopies with intermediate densities $\lambda_f \sim 0.1$ were classified as transitional, and may or may not trigger the instability. In the following sections, we provide an overview of studies on flows in the sparse and dense canopy regimes.

1.2.1 Sparse canopies

A majority of the canopy-flow literature focusses on the dense regime, where the flow over the canopy is known to be dominated by the footprint of the Kelvin–Helmholtz-like, mixing-layer instability. As the canopy density decreases, mixing-layer dynamics eventually cease to operate over it, and such a canopy is termed as sparse (Poggi *et al.*, 2004; Huang *et al.*, 2009; Pietri *et al.*, 2009). However, there still does not seem to be a single quantitative parameter to define a sparse canopy. Raupach *et al.* (1996), who laid the foundation of the mixing-layer theory for dense canopy flows, mentioned that a sparse canopy would be one which has element spacings larger than their height. Some studies have suggested that a canopy would be sparse if the shear stress at the canopy floor is comparable in magnitude to the canopy drag, or equivalently, where the Reynolds shear stresses only approach zero at the canopy floor (Finnigan, 2000; Luhar *et al.*, 2008; Nepf, 2012). This condition essentially implies that sparse canopies would have large element spacings compared to the lengthscales of the turbulent eddies in the flow, which are responsible for generating the Reynolds stresses. These eddies could then penetrate the full height of the canopy only being restricted by the canopy floor. As mentioned previously, Nepf (2012) used the roughness frontal density, λ_f, to classify the canopies and observed that a range of aquatic canopies with $\lambda_f < 0.1$ lay in the sparse regime and did not trigger the Kelvin–Helmholtz-like instability. However, λ_f is a purely geometric parameter and does not take into account the lengthscales of the turbulent eddies. In a canopy with a fixed layout, that is, a fixed spacing and λ_f, the lengthscales of the overlying turbulent flow can be much larger than the element spacing at a particular Reynolds number, so that the turbulent eddies are precluded from penetrating within the canopy. As the Reynolds number is increased, however, the size of the turbulent eddies would eventually become comparable to the spacing and allow the eddies to penetrate within the canopy efficiently. We can therefore expect that the element spacing required

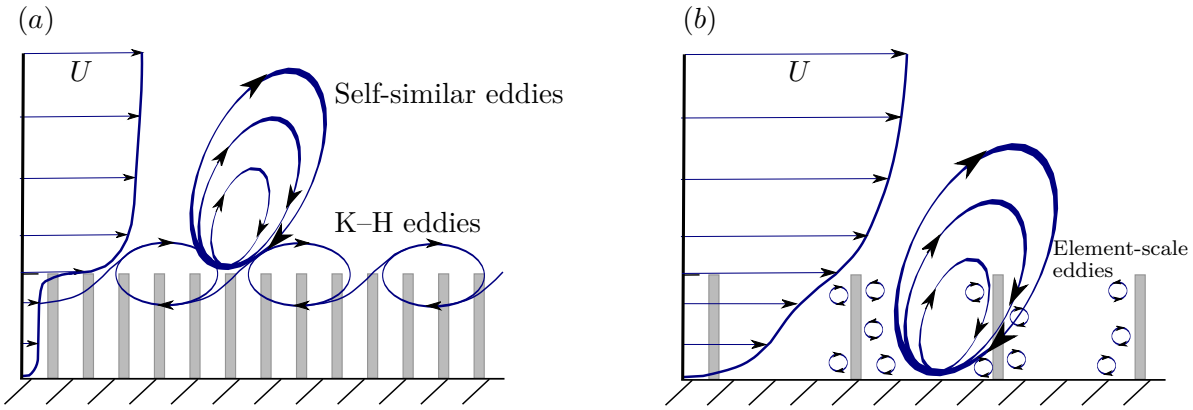

FIGURE 1.3 Schematic representation of flow regimes in (a) dense and (b) sparse canopies adapted from Poggi *et al.* (2004). K–H eddies refers to the eddies associated with Kelvin–Helmholtz-like, mixing-layer instabilities.

for the turbulent eddies to penetrate the full height of the canopy would be linked to the characteristic sizes of the eddies at a particular Reynolds number. Therefore, λ_f on its own may not be a sufficient parameter to determine the canopy regime. Poggi *et al.* (2004) carried out experimental studies of flow over a range of canopies densities to identify the characteristics of the different regimes. They proposed that the flow within the canopy could be broadly divided into three zones. The first zone, near the canopy floor, was found to be dominated by element-scale vortices originating from the wakes of the canopy elements. The second zone, near the top of the canopy, was reported to have an interplay between mixing-layer type eddies and self-similar eddies typical of the flow in the logarithmic region of a turbulent boundary layer. In the third zone, far away from the canopy, outer-layer similarity was recovered. The importance of mixing-layer type instabilities in the second zone was found to depend on the canopy density, with the flow at the top of the canopy becoming more smooth-wall-like with increasing sparsity. These ideas for the limiting cases of an extremely dense and sparse canopy are illustrated in figure 1.3. The flow within the sparsest canopy studied by Poggi *et al.* (2004), however, still showed dissimilarities from smooth-wall flows. The Reynolds shear stresses and the velocity fluctuations within this canopy were smaller than those in the near-wall region of smooth-channels, and the mean-flow profile still exhibited an inflection point at the canopy tips. Huang *et al.* (2009) conducted large-eddy simulations of canopies with densities corresponding to those studied by the experiments of Poggi *et al.* (2004), and also observed the gradual transition of the flow near the canopy top from mixing-layer-like to smooth-wall-like with increasing canopy sparsity.

In computational studies of canopy flows, the canopy elements are usually represented either using a homogenised approach or modelled explicitly as obstacles. Typically, canopies are modelled using a homogeneous drag force in the momentum equations (Dupont & Brunet, 2008; Huang *et al.*, 2009; Finnigan *et al.*, 2009; Bailey & Stoll, 2016). This model applies

a quadratic drag force, $C_{dh}\boldsymbol{u}|\boldsymbol{u}|$, where C_{dh} is the effective canopy drag coefficient and $\boldsymbol{u}$ is the local velocity, homogeneously in the region below the canopy-tip plane. The canopy drag coefficient, C_{dh}, can be a function of the canopy height, and also depends on the canopy geometry and density. This approach would only be strictly valid to represent very closely packed canopies, where the element spacing is much smaller than any lengthscale in the overlying flow, and even small flow structures perceive the canopy elements as acting collectively (Zampogna & Bottaro, 2016). Using a homogeneous drag to capture the effects of sparser canopies tends to overdamp turbulent fluctuations within the canopies (Yue *et al.*, 2007; Bailey & Stoll, 2013). This is typically attributed to the inability of homogenised models to capture the element-induced, dispersive flow, and the lack of representation of the gaps between the canopy elements, where the fluctuations would not experience any damping (Bailey & Stoll, 2013). Several studies have reported that while the dispersive component of the flow is small for dense canopies, it can constitute more than 20% of the total stress in sparse canopies (Poggi & Katul, 2008; Böhm *et al.*, 2013; Harman *et al.*, 2016). Yue *et al.* (2007) and Yan *et al.* (2017) noted certain natural canopies, such as corn crops or tree crowns, allow some flow to pass through them and, thus, they do not behave like conventional bluff bodies. Yue *et al.* (2007) proposed that the flow in such 'permeable' canopies can be represented using a local drag force of the form $C_{dc}\boldsymbol{u}|\boldsymbol{u}|$, applied only at the grid points occupied by the canopy elements. Note that C_{dc} is a local drag coefficient, which is zero outside the region occupied by the canopy elements. This local-drag representation has also been used by Bailey & Stoll (2013) to represent sparse, spanwise-aligned canopies, and has been found to provide a better representation of the flow through such canopies compared to the homogeneous-drag model, which applies a drag at all points in the region below the canopy tips. Most artificial canopies, however, such as high-aspect-ratio roughness and urban canopies, are better represented as impermeable, bluff elements (Coceal *et al.*, 2006, 2008; Sadique *et al.*, 2017). The element-induced flow within such bluff-body canopies is generally quite strong, due to the eddies generated by the sharp edges of the elements (Coceal *et al.*, 2008). Similar to the observations over sparse canopies, mixing-layer type instabilities do not seem to dominate the flow over large cube roughness, despite the presence of an inflection point in the mean velocity profile (Coceal *et al.*, 2007, 2008). Coceal *et al.* (2007) suggest that this is due to the spatial inhomogeneity in the flow within such geometries, which implies that although the spatio-temporal mean might exhibit an inflection point, it may not be representative of the mean at different locations in the canopy.

1.2.2 Dense canopies

As mentioned previously, dense canopy flows are dominated by the presence of Kelvin–Helmholtz-like, mixing-layer instabilities. The connection between mixing-layer and dense canopy flows was made by Raupach *et al.* (1996), who noted that the inflection point at

the top of the canopy could result in the formation of such instabilities. Since then, the appearance of these instabilities over a wide variety of natural canopies has been observed (Finnigan, 2000; Belcher *et al.*, 2012; Nepf, 2012). The presence of these instabilities has also been observed over other complex surfaces such as riblets (García-Mayoral & Jiménez, 2011) and permeable substrates (Jimenez *et al.*, 2001; Kuwata & Suga, 2016; Rosti *et al.*, 2018; Gómez-de-Segura *et al.*, 2018*a*; Gómez-de-Segura & García-Mayoral, 2019). Using the same classification parameters used to define sparse canopies, dense canopies can be defined as those with small element spacings compared to the size of the overlying turbulent lengthscales. The turbulent eddies would then be precluded from penetrating within the canopies, as portrayed in the schematic of figure 1.3(a), and the Reynolds shear stresses within them would be small. Such canopies typically have large roughness frontal densities, $\lambda_f \gg 0.1$ in addition to small element spacings (Poggi *et al.*, 2004; Huang *et al.*, 2009; Nepf, 2012). Kelvin–Helmholtz instabilities manifest in the flow as spanwise coherent rollers, whose streamwise scale is determined by the shear-layer thickness (Michalke, 1972; Brown & Roshko, 1974). Unlike free-shear flows, where the shear-layer thickness, and consequently, the instability wavelength grows downstream, in canopy flows their growth is limited by the canopy drag (Ghisalberti & Nepf, 2004). Therefore, a fixed instability wavelength is observed over canopy flows, whose scale is governed by the shear-layer thickness calculated at the canopy-tip plane, $L_s = U/(\mathrm{d}U/\mathrm{d}y)$, where U is the mean velocity profile (Raupach *et al.*, 1996; Finnigan, 2000; Nepf, 2012). Nepf *et al.* (2007) demonstrated that the shear-layer thickness in canopy flows is inversely proportional to the effective canopy drag coefficient, implying that denser canopies would elicit instabilities with smaller wavelengths compared to a sparser canopy. This instability is known to increase vertical momentum exchange between the canopy and the overlying flow (Finnigan, 2000; Nepf, 2012), and can, therefore, enhance mixing and heat transfer. In the case of flexible canopies, the passage of Kelvin–Helmholtz-like instabilities over them can cause the coherent bending of the canopy elements, giving the appearance of a wave passing over them. This coherent bending is referred to as *honami* in terrestrial canopies (Inoue, 1955) and *monami* in aquatic ones (Ackerman & Okubo, 1993). For certain canopy parameters, the element-waving and instability frequencies may also lock-in (Ikeda & Kanazawa, 1996; Ghisalberti & Nepf, 2002; Py *et al.*, 2006; Gosselin & De Langre, 2009). Although the Kelvin–Helmholtz-like instability in quiescent flow remains spanwise coherent, several studies have shown that they can be distorted by the presence of turbulent fluctuations, and perhaps lose their spanwise coherent nature (Rogers & Moser, 1994; Raupach *et al.*, 1996; Finnigan *et al.*, 2009; Bailey & Stoll, 2016). As discussed in §1.2.1, the importance of this instability reduces with increasing canopy spacing, and sparse canopies do not exhibit a notable signature of it. It could be expected, however, that the effect of increasing the canopy height at a fixed element spacing on the instability and the surrounding canopy flow eventually saturates. Such an effect was noted by Sadique *et al.* (2017), who examined the mean-velocity profiles in turbulent flows over high-aspect-ratio

prismatic posts. They found that the mean-velocity profile over such geometries became independent of the element heights at large element aspect ratios. They concluded that the overlying flow only interacted with the region near the element tips and that the height below this 'active' region was dormant, and did not have a significant effect on the overlying flow. For their geometries, Sadique *et al.* (2017) observed the height of this active region to be related to the element width. A similar observation was also made by MacDonald *et al.* (2018), who performed direct numerical simulations of flows over spanwise-aligned bars. They found that the gap between the bars was the relevant lengthscale for the overlying flow. Increasing the height of the bars beyond a certain height-to-gap ratio did not affect the overlying flow, or cause an increase in the drag produced by them. This saturation can be attributed to the sheltering effect of the preceding bar or roughness element on the fluid region ahead of it (Grimmond & Oke, 1999; Jiménez, 2004; Yang *et al.*, 2016). The flow overlying such geometries would then skim over the obstacles without interacting with their full height.

1.3 Linear stability analysis of canopy flows

In this section, we discuss studies that perform a stability analysis to capture the Kelvin–Helmholtz-like instability over dense canopies. This instability is a linear, inviscid phenomenon originating from the inflection point in the mean-flow (Michalke, 1972; Brown & Roshko, 1974). Several studies have shown that this instability can be captured by a mean-flow linear stability analysis (Raupach *et al.*, 1996; White & Nepf, 2007; Singh *et al.*, 2016; Zampogna *et al.*, 2016; Luminari *et al.*, 2016). The study by Raupach *et al.* (1996) that originally made the connection between canopy and mixing-layer flows used a hyperbolic tangent profile to perform this analysis, illustrated in figure 1.4(b). They showed that even though this instability was modified through non-linear interactions with the ambient turbulent fluctuations after its inception, the stability analysis was still able to provide an estimate of the scale of the instability. Raupach *et al.* (1996) showed that similar to free-shear flows, the streamwise wavelength of the instability was given by the shear length, $L_s = U/(dU/dy)$, calculated at the canopy-tip plane. As discussed previously, the study by Ghisalberti & Nepf (2004) made a distinction between canopy- and free-shear layers, in the sense that while free-shear layers continued to grow downstream, the thickness of the canopy-shear layer was bounded by the canopy drag. White & Nepf (2007) examined the stability of flows adjacent to an array of submerged cylindrical elements, with the ends of the elements protruding above the water. They showed that while the instability could be enhanced by a large difference in the canopy drag compared to the wall shear stress, too large a canopy drag could also inhibit the instability by damping the fluctuations within the canopy. White & Nepf (2007) also suggested that the wavelength of the instability depended on the shear-layer thickness associated with the boundary layer which forms outside the canopy. The full shear layer

thickness in canopy flows would, therefore, have a component above and below the canopy-tip plane, and while the latter was set by the canopy drag, the former would be a property of the boundary layer above the canopy. Shear layers in canopy flows, therefore, could have asymmetric contributions from the regions above and below the canopy-tip plane, different from the conventional piecewise-linear or hyperbolic tangent profiles conventionally used to study canopy flow stability, as illustrated in figure 1.4. More recently, Singh *et al.* (2016) have re-examined the stability of dense, aquatic canopies. They represented the canopies as a homogeneous drag force in the Navier-Stokes equations. The drag term was proportional to the square of the mean velocity, with the canopy drag coefficient assumed to be constant across the canopy height. The base flow was obtained by solving the averaged momentum equations, ignoring the effect of the Reynolds shear stresses. As a result, the flow above the canopy had a parabolic profile. Singh *et al.* (2016) observed that two instability modes existed in dense canopy flows. The first was the Kelvin–Helmholtz-like instability, and the other, a secondary instability originating from an interaction between the canopy drag and the overlying flow. The two instability modes were found to be identical for low values of canopy drag, but several differences were observed for canopies with large drag. While the Kelvin–Helmholtz mode was governed by the shear at the canopy-tip plane and remained localised to this region, the secondary instability depended on the magnitude of the canopy drag and spanned the entire width of the channel. Zampogna *et al.* (2016) proposed an alternative to the drag model to study the canopy flow instability. They modelled the flow within the canopy as a permeable substrate governed by Darcy's equation (Darcy, 1856)

$$\nu \boldsymbol{K}^{-1} \boldsymbol{u} = -\nabla p \tag{1.1}$$

where $\boldsymbol{K}^{-1}$ is the inverse permeability tensor, which can be used to account for the canopy anisotropy, $\boldsymbol{u}$ is the velocity vector, and p is the pressure. The flow within the canopy is solved analytically, and the solution is used as a boundary condition for the overlying flow. Zampogna *et al.* (2016) observed that this model could provide better estimates for the instability wavelength and amplification for aquatic canopy flows than representing the canopy as a drag force. Their analysis, however, represents the effect of turbulence on the mean flow using a constant eddy viscosity above the canopy, which may not be the case for turbulent channel flow. Abderrahaman-Elena & García-Mayoral (2017) also considered the stability of turbulent flows over anisotropic permeable substrates governed by Darcy's equation. They considered two kinds of base flows above the permeable substrate, a piecewise linear profile, similar to the one shown in figure 1.4(a), and turbulent channel flow. They showed that the instability within such substrates was essentially governed by a single parameter, the geometric mean of the streamwise and wall-normal permeabilities. The use of Darcy's equation to model the flow within the permeable substrate, however, implies that the region of high shear within the canopy near the canopy free-flow interface could

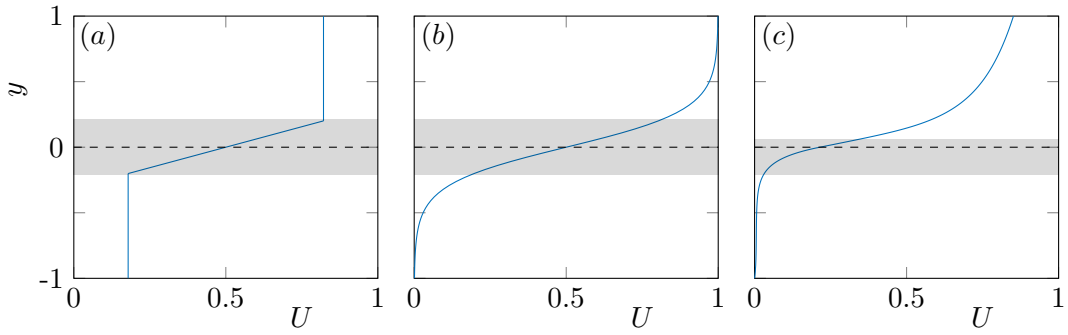

FIGURE 1.4 Velocity profiles used for studying canopy flow stability. (a) Piecewise-linear profile, (b) hyperbolic-tangent profile, and (c) schematic of mean velocity profile of turbulent flow over a dense canopy. The shaded region marks the approximate thickness of the shear layer and the dashed horizontal line marks the notional location of the canopy tips.

not be captured. In the present work we extend the analysis of Abderrahaman-Elena & García-Mayoral (2017) to include the effect of this high shear region by employing Brinkman's equation (Brinkman, 1949) to model the flow within the canopy

$$\tilde{\nu}\nabla^2\boldsymbol{u} - \nu\boldsymbol{K}^{-1} - \nabla p = 0, \tag{1.2}$$

where $\tilde{\nu}$ is the macroscale viscosity which depends on the geometry of the permeable substrate. This parameter determines how well the shear in the overlying flow can be transferred to the fluid within the permeable substrate (Abderrahaman-Elena & García-Mayoral, 2017; Gómez-de-Segura & García-Mayoral, 2019). For fibres aligned perpendicular to the flow, we can expect the flow within and above the substrate to be well connected and therefore communicate the shear across the interface efficiently. For such geometries, $\tilde{\nu}$ can be approximated as the molecular viscosity, ν (Lévy, 1983; Auriault, 2009). The height of the high shear region, or the shear length, below the canopy interface, or the 'Brinkman boundary layer', in this case, is determined by the square root of the streamwise permeability, $\sqrt{K_x}$ (Saffman, 1971; Battiato, 2012). Abderrahaman-Elena & García-Mayoral (2017) also noted that the shear layer thickness above the permeable substrate was governed by the turbulent mean velocity profile, consistent with the observation of White & Nepf (2007). Abderrahaman-Elena & García-Mayoral (2017) found that this thickness was given by the height above the substrate at which the mean vorticity gradient concentrates. They observed that for the turbulent smooth-channel flow they used as their base profile this height scaled in inner units, and had a value of $y_c^+ \approx 7$. A similar observation was also made by García-Mayoral & Jiménez (2011), who performed a stability analysis of turbulent flows over riblets, which also elicit Kelvin–Helmholtz-like instabilities.

The studies of Py *et al.* (2006) and, more recently, Wong *et al.* (2019) have also explored how the waving of flexible canopy elements affects the instability. Py *et al.* (2006) showed through their stability analysis that it was possible for the waving frequency of the canopy elements to lock in with the frequency of the instability, leading to more intense canopy waving. However, Dupont *et al.* (2010) performed a large eddy simulation of the domain studied by Py *et al.* (2006) and did not observe the predicted lock-in phenomenon. They concluded that the distortion of the instability by the ambient turbulence was the likely reason for the element waving not locking-in with the instability. Wong *et al.* (2019), in addition, showed that canopies with highly flexible elements could also inhibit the instability. In the present study, however, we only analyse the flow over rigid canopies.

Similar to the studies of Jimenez *et al.* (2001), Dupont *et al.* (2010), García-Mayoral & Jiménez (2011), Abderrahaman-Elena & García-Mayoral (2017) and Gómez-de-Segura & García-Mayoral (2019), we perform a linear stability analysis around a turbulent mean flow to capture the Kelvin–Helmholtz-like instabilities associated with dense canopy flows. Although these studies have shown that such an analysis is able to capture the Kelvin–Helmholtz-like instability observed in turbulent flows over a variety of complex surfaces, the validity of such an analysis has still not been formalised. The main issue with performing a mean flow stability analysis on a turbulent flow is that due to its unsteady nature, the spatio-temporal mean of the flow may not be representative of the velocity profile at a given instance in time. The studies of Turton *et al.* (2015) and Beneddine *et al.* (2016) have shown that such an analysis can yield meaningful results under certain conditions. Beneddine *et al.* (2016) conclude that a mean flow stability analysis can be used to capture instabilities in a turbulent flow as long as the instabilities are convective, and there is sufficient separation of scales between the energetic turbulent fluctuations and the instability. We observe in the present work, that in agreement with the results of the aforementioned studies, some features of the Kelvin–Helmholtz-like instability in turbulent flows over dense canopies can be captured by such an analysis.

1.4 Aims and organisation of the thesis

The aim of this thesis is to analyse turbulent flows over canopies in different regimes. To this effect we simulate the flow over canopies with different element geometries, spacings and heights using direct numerical simulation. The conducted simulations can be divided into two, those of sparse canopies and those of dense canopies. For sparse canopies, we place particular emphasis on the scaling of the turbulence fluctuations within the canopy. In dense canopy flows, we examine how the canopy parameters affect the Kelvin–Helmholtz-like instability over them.

This thesis is composed of six chapters, including the current, introductory chapter. The organisation and content of the remaining chapters is summarised below.

In chapter 2, we discuss the numerical method used. The methodology employed to integrate the Navier-Stokes equations is briefly discussed, followed by a description of the different methods used to represent the canopy elements in the flow. The validation studies for the numerical method are also presented.

In chapter 3, we discuss the results from the sparse canopy simulations. The sparse canopies considered have low roughness frontal densities, $\lambda_f \lesssim 0.1$, and element spacings larger than the typical scales of near-wall turbulent structures such as streaks. This ensures that the canopy is sparse from the point of view of the turbulent eddies, so they should penetrate the full height of the canopy. Canopies with different geometries and spacings are considered. Following the observations of Poggi *et al.* (2004) and Coceal *et al.* (2008), we expect the flow within such canopies to have a strong footprint of the element induced flow, rather that of the Kelvin–Helmholtz-like instability. We separate the effect of the element-induced coherent flow from the incoherent background turbulence and focus mainly on the properties of the latter. A scaling based on the local sum of the viscous and Reynolds shear stresses at each height within the canopy is proposed. While Poggi *et al.* (2004) have shown that the flow near the top of such canopies can be smooth-wall-like, in the proposed scaling the background-turbulence fluctuations within the canopy also show similarities to those of smooth-wall flows. The suggests that the sparse canopies affect the background turbulence through a change in its local scale rather than by the direct interaction of the canopy elements with the fluctuations. We show that this effect can be captured better by a drag applied on the mean-flow alone rather than a conventional homogeneous drag. Chapter 3 is divided into two major parts, the first half discusses the results from the resolved canopy simulations and introduces the local scaling and the second half presents the results from the homogeneous and mean-only drag simulations.

In chapter 4, we present the results from DNS of flows over dense canopies composed of rigid, prismatic filaments. These canopies have small element spacings and large height-to-spacing ratios. The spacings range from $s^+ \approx 2.6$ to 48 for the densest and sparsest canopy geometries considered, respectively. We assess the effect of the element height and spacing on the turbulent fluctuations within the canopies and above them. The canopy elements are represented in the flow as solid, impermeable obstacles. The canopy geometries considered here are dense enough to trigger the Kelvin–Helmholtz-like instabilities discussed earlier in this section. We also study the effect of varying the canopy parameters on this instability. The underlying objective behind this study is to explore whether such canopies can be tuned to maximise or minimise the intensity of the Kelvin–Helmholtz-like instabilities over them. Canopy parameters that elicit strong instabilities could be used to optimise or design heat exchangers or devices for energy harvesting. The chapter is also divided into two parts, the first detailing the effect of the canopy parameters on the overlying turbulent fluctuations and the second, their effect on the Kelvin–Helmholtz-like instability.

In chapter 5, we propose two *a priori* methods based on linear stability analysis to characterise the Kelvin–Helmholtz-like instability in dense canopy flows. The first represents the canopy as an anisotropic permeable substrate governed by Brinkman's equation. This is a continuation of the work of Abderrahaman-Elena & García-Mayoral (2017), who used Darcy's equation to model the flow within the substrate. The second model represents the canopy as a drag force in the momentum equations, similar to Singh *et al.* (2016). However, unlike Singh *et al.* (2016), who assumed the flow overlying the canopies to be laminar, we analyse the stability of turbulent channel flows. Both these models are used to investigate the canopy parameters that affect the formation of the Kelvin–Helmholtz-like instability. In the final part of this chapter, we analyse the stability of the mean velocity profiles obtained from the DNS of dense canopy flows which are discussed in chapter 4. We compare the predictions of the stability analysis with the instabilities observed in the DNSs. Finally, we also compare the results from the analysis of the DNS mean profiles with the analysis of corresponding profiles synthesised using the drag-force model.

In the final chapter, we present the conclusions of the present work and potential avenues for future work.

Chapter 2

Numerical method

This chapter discusses the numerical methods used in the present study. The code used to perform the DNSs has been adapted from García-Mayoral & Jiménez (2011) and Fairhall & García-Mayoral (2018), and was originally developed to study flows over riblets and superhydrophobic surfaces. This code is briefly described here, followed by the details of the immersed-boundary method used to represent impermeable canopy elements in the flow. The validation of the proposed immersed-boundary method is then presented. In the final part of the chapter, the details and implementation of drag-force models that are used in the study regarding sparse canopy flows are discussed.

Flows in either open or symmetric channels are studied, which are governed by the three-dimensional, incompressible Navier-Stokes and continuity equations

$$\frac{\partial \mathbf{u}}{\partial t} + \mathbf{u}\cdot\nabla\mathbf{u} = -\nabla p + \frac{1}{Re}\nabla^2\mathbf{u}, \tag{2.1}$$

$$\nabla\cdot\mathbf{u} = 0, \tag{2.2}$$

where $\mathbf{u}$ is the velocity vector, p is the kinematic pressure, and $Re = U_b\delta/\nu$ is the Reynolds number based on the bulk velocity, U_b, the channel half-height, δ, and the kinematic viscosity, ν. The velocity vector, $\mathbf{u}$, has the components u, v and w in the streamwise, wall-normal and spanwise directions, respectively, with the associated axes being, x, y and z, respectively. Note that we only consider incompressible flows where the density of the fluid remains constant and is set to $\rho = 1$.

2.1 Temporal discretisation

The temporal discretisation is carried out using a Runge–Kutta method, with each time step, n, divided into three substeps, denoted by k. Within each Runge–Kutta substep, the viscous

	$k=1$	$k=2$	$k=3$
α_k	4/15	1/15	1/6
β_k	4/15	1/15	1/6
γ_k	8/15	5/12	3/4
ζ_k	0	−17/60	−5/12

Table 2.1 The coefficients for the three Runge–Kutta substeps from Le & Moin (1991) used in the present work.

terms are treated semi-implicitly, and the advective terms are treated explicitly

$$\left[\mathrm{I}-\Delta t\frac{\beta_k}{Re}\mathrm{L}\right]\mathbf{u}_k^n = \mathbf{u}_{k-1}^n+\Delta t\left[\frac{\alpha_k}{Re}\mathrm{L}\mathbf{u}_{k-1}^n-\gamma_k\mathrm{N}(\mathbf{u}_{k-1}^n)-\zeta_k\mathrm{N}(\mathbf{u}_{k-2}^n)-(\alpha_k+\beta_k)\mathrm{G}(p_k^n)\right], k\in[1,3], \tag{2.3}$$

$$\mathrm{D}\mathbf{u}_k^n = 0, \tag{2.4}$$

where I is the identity matrix and L, D and G are the discretised Laplacian, divergence and gradient operators respectively. N is the dealiased advective term. Δt is the timestep, and α_k, β_k, γ_k and ζ_k are the Runge–Kutta coefficients for substep k. A fractional-step, pressure correction method is used to decouple the velocity and the pressure (Kim & Moin, 1985; Perot, 1993). An intermediate velocity, $\mathbf{u}_*$, is first obtained, which does not satisfy continuity. This velocity is used to obtain the pressure field for the subsequent substep which would be required for the velocity field to be divergence free. The obtained pressure is then used to obtain the corrected, divergence-free velocity field

$$\left[\mathrm{I}-\Delta t\frac{\beta_k}{Re}\mathrm{L}\right]\mathbf{u}_* = \mathbf{u}_{k-1}^n+\Delta t\left[\frac{\alpha_k}{Re}\mathrm{L}\mathbf{u}_{k-1}^n-\gamma_k\mathrm{N}(\mathbf{u}_{k-1}^n)-\zeta_k\mathrm{N}(\mathbf{u}_{k-2}^n)-(\alpha_k+\beta_k)\mathrm{G}(p_k^n)\right], \quad k\in[1,3], \tag{2.5}$$

$$\mathrm{DG}(\phi_k^n) = \frac{1}{(\alpha_k+\beta_k)\Delta t}\mathrm{D}(\mathbf{u}_*), \tag{2.6}$$

$$\mathbf{u}_{k+1}^n = \mathbf{u}_*-(\alpha_k+\beta_k)\Delta t G(\phi_k^n), \tag{2.7}$$

$$p_{k+1}^n = p_k^n+\phi_k^n. \tag{2.8}$$

Simens (2008) showed that solving the equations for the pressure difference, $\phi_k^n = p_{k+1}^n - p_k^n$, provides second-order accuracy for the velocities in time, compared to the first-order accuracy obtained by solving for the pressure directly. The variables of the subsequent timestep, $n+1$, are obtained at the final Runge–Kutta substep, $k=3$. The Runge–Kutta coefficients used

are from Le & Moin (1991), and are listed in table 2.1. The timestep, Δt, is adjusted to maintain the viscous and advective CFL numbers below 2.5 and 0.7, respectively. Further details about this implementation can be found in Fairhall & García-Mayoral (2018) and Fairhall (2018).

2.2 Spatial discretisation

The channels considered in the current study are periodic in x and z and a Fourier spectral discretisation is used in these directions. This method provides a much higher accuracy in calculating the derivatives when using a given number of grid points compared to finite difference methods (Canuto *et al.*, 2012). The spectral resolutions required to resolve the relevant turbulent scales in a smooth channel are $\Delta x^+ \lesssim 8$ and $\Delta z^+ \lesssim 4$ (Jiménez & Moin, 1991; Moin & Mahesh, 1998). When simulating flows over rough surfaces, however, resolving the flow induced by the roughness elements may require a higher resolution than that required to resolve the turbulent scales. In order to reduce the computational cost associated with resolving the canopy elements, the code utilises a multi-block approach. The simulation domain is split into three blocks, and the wall-parallel resolutions of each block can be varied (García-Mayoral & Jiménez, 2011). In a symmetric channel, with canopy elements on both walls, the blocks which include the canopy elements and the roughness sublayer have a finer resolution than the central, coarse block, which retains the smooth-channel resolution given above. The resolution of the fine blocks depends on the size of the canopy elements simulated. The height of the blocks is set far enough away from the canopy tips, beyond the height where the element-induced flow has decayed to zero. Whether the height of the fine blocks is sufficiently far away from the canopy tips is verified *a posteriori*. Further details about the implementation of the multi-block technique can be found in García-Mayoral (2011), Abderrahaman-Elena (2018) and Fairhall (2018).

The use of a spectral discretisation simplifies the calculation of the wall-parallel derivatives in the governing equations. In Fourier space, the derivatives of a function can be expressed as the product of the function with a wavenumber. For example, for a given streamwise wavenumber, α, the derivative of a function $f(x)$ would be $\partial \widehat{f}(\alpha)/dx = i\alpha \widehat{f}(\alpha)$, where $\widehat{(\cdot)}$ denotes variables in Fourier space. The differentiation matrices resulting from a spectral discretisation scheme are purely diagonal, with off-diagonal terms introduced by the discretisation scheme used in the wall-normal direction. In the present work, we use a second-order, centred finite difference scheme for the wall-normal direction, which overall, results in a tridiagonal matrix for the Laplacian operator in equation (2.5). Solving a tridiagonal system of equations can be performed very efficiently using Thomas' algorithm which only requires $\mathcal{O}(N)$ operations, where N is the number of Fourier modes, thereby significantly reducing the computational costs. The calculation of the non-linear products in Fourier space involves a convolution, which is an $\mathcal{O}(N^2)$ operation. In order to circumvent calculating this

convolution, we calculate the non-linear products in physical space, which involves $\mathcal{O}(N)$ operations, using the 2/3 rule for de-aliasing (Canuto *et al.*, 2012). In this process, there is an overhead of transforming the variables from Fourier to physical space and back again. A Fast Fourier Transform is used to perform these operations, which involves $\mathcal{O}(N \log_2 N)$ operations (Cooley & Tukey, 1965). The overall cost of calculating the non-linear products in physical space still reduces the computational cost significantly compared to calculating the convolution.

As mentioned previously, a second-order, centred finite difference scheme is used to discretise the wall-normal direction. In order to deal with the large gradients in the flow near the wall or the canopy tips we employ a stretched grid. In sparse canopy flows, where the shear at the base of the canopies is high, we employ a grid which has a high resolution, $\Delta y^+ \approx 0.2$, at the canopy base and gradually coarsens near the centre of the channel to $\Delta y^+ \approx 2$. The stretching function is a fifth-order polynomial, also used by García-Mayoral & Jiménez (2011), Abderrahaman-Elena *et al.* (2019) and Fairhall *et al.* (2019)

$$y(j) \quad = \quad a_1(j - N/2)^5 + a_2(j - N/2); \; j \in [0, N], \tag{2.9}$$

where y is the wall-normal coordinate, N is the total number of grid points in the wall-normal direction, and a_1 and a_2 are constants that determine the size of the channel and the variation in the grid resolution across the channel.

In dense canopies, turbulent fluctuations do not penetrate much within the canopy, and the shear is largest at the canopy tips. In these cases, the resolution near the tips is maintained around $\Delta y^+ \approx 0.33$, and gradually increased both above and below the tips. The resolution at the centre of the channel is kept at $\Delta y^+ \approx 3.3$. The resolution at the bottom of the canopy, where the flow is quiescent, is at maximum $\Delta y^+ \approx 4$ for the tallest canopy considered. The grid composed of two polynomial functions, one in the channel centre, and the other within the canopies, which join smoothly at the canopy tips

$$y(j) \quad = \quad a_1(j - N/2)^5 + a_2(j - N/2)^3 + a_3(j - N/2); \; j \in [0, N], \tag{2.10}$$

$$y(j) \quad = \quad b_1 j^3 + b_2 j - 1; \; j \in [-N_c, 0), \tag{2.11}$$

$$y(j) \quad = \quad b_1(j - N)^3 + b_2(j - N) + 1; \; j \in (N, N + N_c], \tag{2.12}$$

where y is the wall-normal coordinate, N is the number grid points between the canopy-tip planes, N_c is the number of points within the canopy elements, and a_i and b_i determine the size of the channels and the variation in the grid resolution across it. The wall-normal grid used, and the variation of the grid resolution with the channel height for the tallest dense canopy case are portrayed in figure 2.1, for reference.

When using a finite difference scheme, a convenient option is to store the velocities and the pressure at the same grid points, that is, using a 'collocated' grid. Using such a grid while

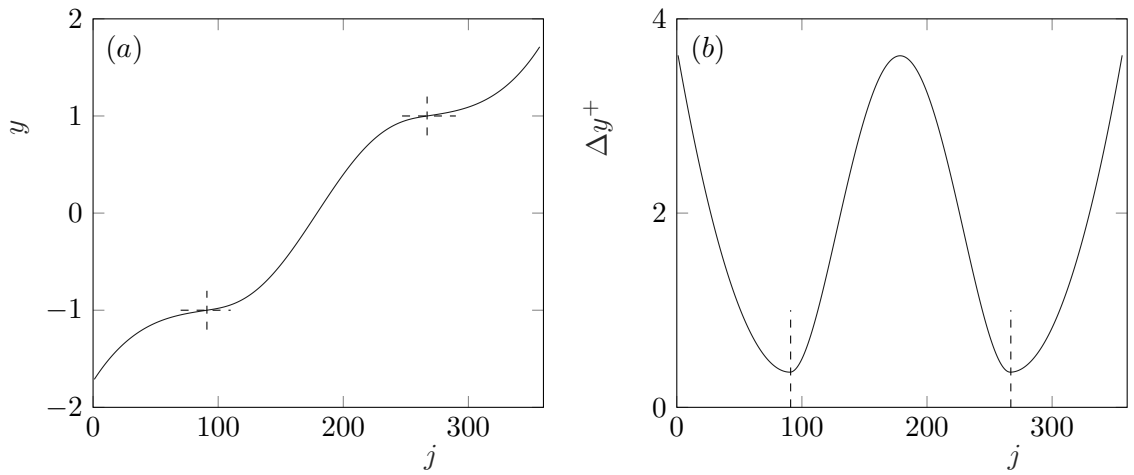

FIGURE 2.1 An example of the wall normal grid used for the dense canopy simulations. (a) shows the variation of the wall-normal coordinate with an equispaced auxiliary variable, j, and (b) shows the variation in the grid resolution with j. The dashed lines mark the location of the canopy-tip planes. Note that canopy elements extend below $y = -1$ and above $y = 1$.

also employing a second-order, centred finite difference scheme, however, can lead to the 'chequerboard' problem when solving the Poisson equation for the pressure, equation (2.6) (Ferziger & Peric, 2012). This occurs if the divergence of the gradient of pressure at any point j, depends on the values of the pressure at j and two grid points away from it, $j-2$ and $j+2$, rather than the adjacent ones. This can lead to two decoupled pressure fields that exist on alternating grid points. There are several strategies to mitigate this effect. García-Mayoral & Jiménez (2011) and Abderrahaman-Elena *et al.* (2019), for example, use a collocated grid with weakly-enforced continuity (Nordström *et al.*, 2007). In the present code, this issue was dealt with by using a staggered grid, implemented by Fairhall & García-Mayoral (2018), where the pressure and velocity grid points are offset by half a grid spacing, and values of pressure at the adjacent grid points are used when calculating the divergence of its gradient in equation (2.6). The grid is only staggered in the wall-normal direction, as a Fourier spectral discretisation is used in the wall-parallel directions.

2.3 Immersed-boundary method

In this section, the details of the immersed boundary method used to represent the canopy element geometries in the flow are discussed. The method of immersed boundaries is used over other methods, such as fitted grids, as it allows us to retain a uniform, cartesian grid in the wall-parallel directions, and thus also retain the Fourier spectral discretisation. In the code used here, a modified version of the immersed boundary algorithm proposed by García-Mayoral & Jiménez (2011) is used. The algorithm of García-Mayoral & Jiménez (2011) was

based on a direct-forcing approach, which applies a body force within the immersed-boundary points to drive the velocity at these points to zero (Mittal & Iaccarino, 2005). The condition to implement at the points within the canopy elements is

$$\frac{\mathbf{u}^{n+1} - \mathbf{u}^{n}}{\Delta t} = \frac{-\mathbf{u}^{n}}{\Delta t} \tag{2.13}$$

Following García-Mayoral & Jiménez (2011), this condition can be approximated by modifying the right-hand-side of equation (2.5)

$$\left[\mathrm{I} - \Delta t \frac{\beta_k}{Re}\mathrm{L}\right] \mathbf{u}_k^n = -\Delta t \frac{\beta_k}{Re}\mathrm{L}\mathbf{u}_{k-1}^n. \tag{2.14}$$

In the present work, a modification of this implementation is proposed, which offers an improvement in the accuracy for the velocities within the immersed boundary regions. This implementation is summarised below. The Laplacian operator on the left-hand-side of equation (2.5) is first split into its wall-parallel and wall-normal components following Kim & Moin (1985)

$$\left[\mathrm{I} - \Delta t \frac{\beta_k}{Re}\mathrm{L}\right] \mathbf{u} \approx \left[\mathrm{I} - \Delta t \frac{\beta_k}{Re}\mathrm{L}_{xz}\right] \left[\mathrm{I} - \Delta t \frac{\beta_k}{Re}\mathrm{L}_{y}\right] \mathbf{u}, \tag{2.15}$$

where L_{xz} includes the wall-parallel components of L, and L_y the wall-normal one. Splitting the Laplacian in this manner still retains the second-order temporal accuracy of the code (Kim & Moin, 1985). Equation (2.5) can then be written as

$$\left[\mathrm{I} - \Delta t \frac{\beta_k}{Re}\mathrm{L}_{y}\right] \mathbf{u} \;= \left[\mathrm{I} - \Delta t \frac{\beta_k}{Re}\mathrm{L}_{xz}\right]^{-1} \mathrm{RHS}. \tag{2.16}$$

The right-hand-side of equation (2.16) is then transformed to physical space, and modified to satisfy the following conditions within the immersed boundary points

$$\left[\mathrm{I} - \Delta t \frac{\beta_k}{Re}\mathrm{L}_{y}\right] \mathbf{u}_k^n = \begin{cases} -\Delta t \frac{\beta_k}{Re}\mathrm{L}_y \mathbf{u}_{k-1}^n, & y = y_{interface} \\ 0, & y \neq y_{interface}. \end{cases} \tag{2.17}$$

where $y_{interface}$ denotes any wall-normal plane where the solid geometry being represented has an interface with the fluid region. These interface planes for the two element geometries, a prismatic post and a 'T'-shaped geometry, are illustrated in figure 2.2. At the interfaces, the condition imposed by equation (2.17) yields $\mathbf{u}_k^n = \mathcal{O}(\Delta t^2)$, which is of the order of the temporal discretisation error of the code. As a staggered grid is used, the wall-normal grid points for the streamwise velocities are offset by half a grid spacing from those of the wall-normal velocity. The element tips are aligned with the grid for the streamwise velocity. For the wall-normal velocity, the interface condition is set at the last wall-normal grid point within the element, which, through continuity, yields near-zero wall-normal velocity at the element tips. Away from the interfaces, within the immersed boundary region, the condition set by

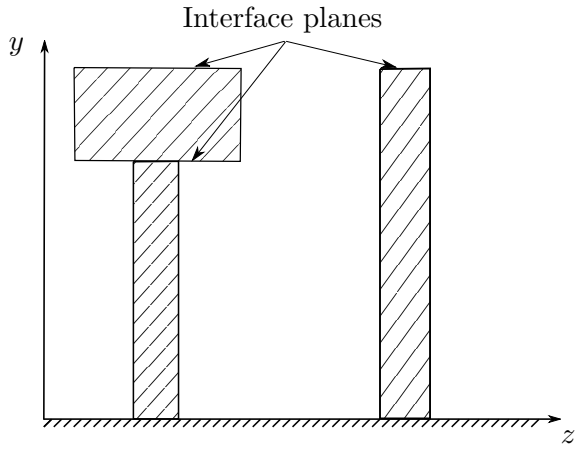

FIGURE 2.2 Schematic representation of 'T'-shaped and prismatic-post canopy element geometries, with the location of the wall-normal solid-fluid interfaces marked.

equation (2.17) results in an exponential decay of the velocity in the wall-normal direction. To illustrate this decay, the results from a simple, one-dimensional implementation of this algorithm are shown in figure 2.3. The velocity is assumed to vary only in the wall-normal direction, and two geometries are considered. The first is analogous to a one-dimensional cut through the middle of either of the geometries shown in figure 2.2. The second geometry is analogous to taking a cut through the overhang regions of the 'T'-shaped elements. For these test cases, random initial conditions are used to mimic turbulent fluctuations in the flow. The velocity fields obtained for these cases, after one timestep, using the immersed boundary conditions of equation (2.17) are compared to those obtained using equation (2.14) in figure 2.3. Although both algorithms result in small velocities within the solid regions, the implementation proposed here results in a smoother decay of the velocity within the solid. In the DNS code, however, the velocity correction step introduces an error of order Δt^2 in all the immersed boundary points. Even so, in experience it was observed that the proposed algorithm is a more stable numerical implementation of the immersed boundaries compared to the one proposed by García-Mayoral & Jiménez (2011). This is likely due to the present method not generating sharp gradients in the velocity field within the solid obstacles at the pressure calculation step (see equation 2.6). The velocity within the canopy elements, or the permeability error, in the DNSs is observed to be less than $0.1u_\tau$, for all the conducted simulations. Randomly selected instantaneous velocity fields from one of the simulations are portrayed in figure 2.4 to illustrate the permeability error. It can also be noted from figure 2.4 that the velocity within the canopy elements is much smaller than the velocity in the surrounding region.

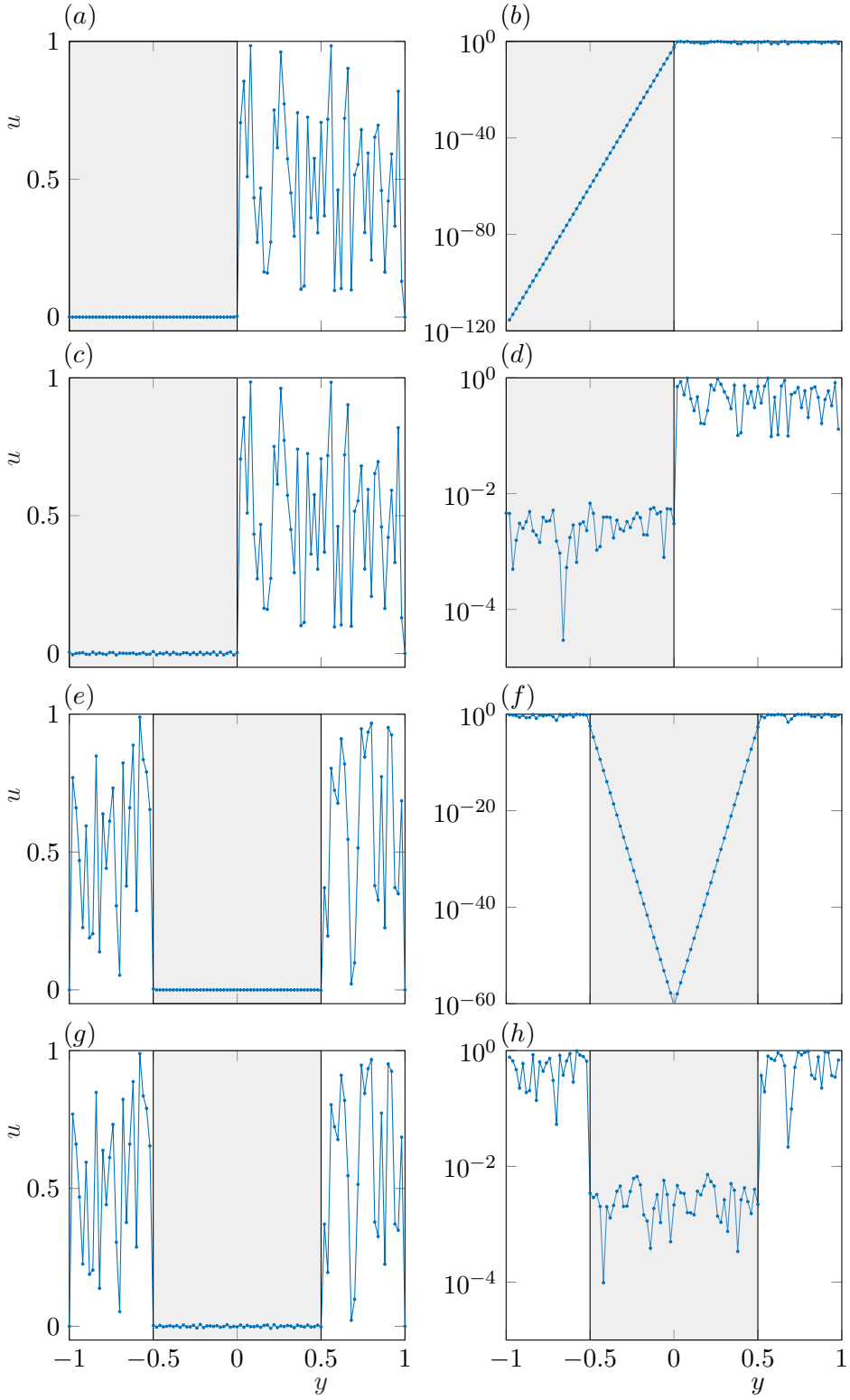

FIGURE 2.3 Velocity profiles obtained using the two immersed boundary algorithms described in §2.3, after one time step, starting from random initial conditions. (a,b,e,f) show results obtained from algorithm proposed here, given by equation (2.17), and (c,d,g,h) those from using equation (2.14). The shaded regions mark the location of the solid obstacles. The same data is plotted in the left and right columns, except that the right column portrays the velocities in a logarithmic scale.

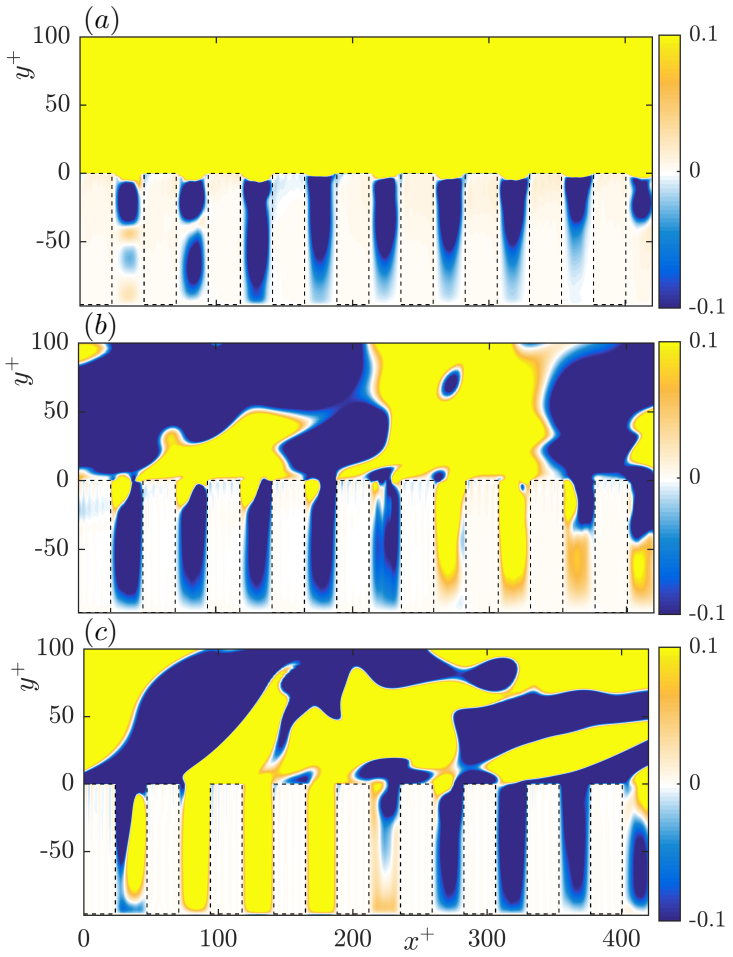

FIGURE 2.4 Instantaneous realisations of the (a) streamwise, (b) wall-normal and (c) spanwise velocities in a plane passing through the middle of the canopy elements, scaled with the friction velocity.

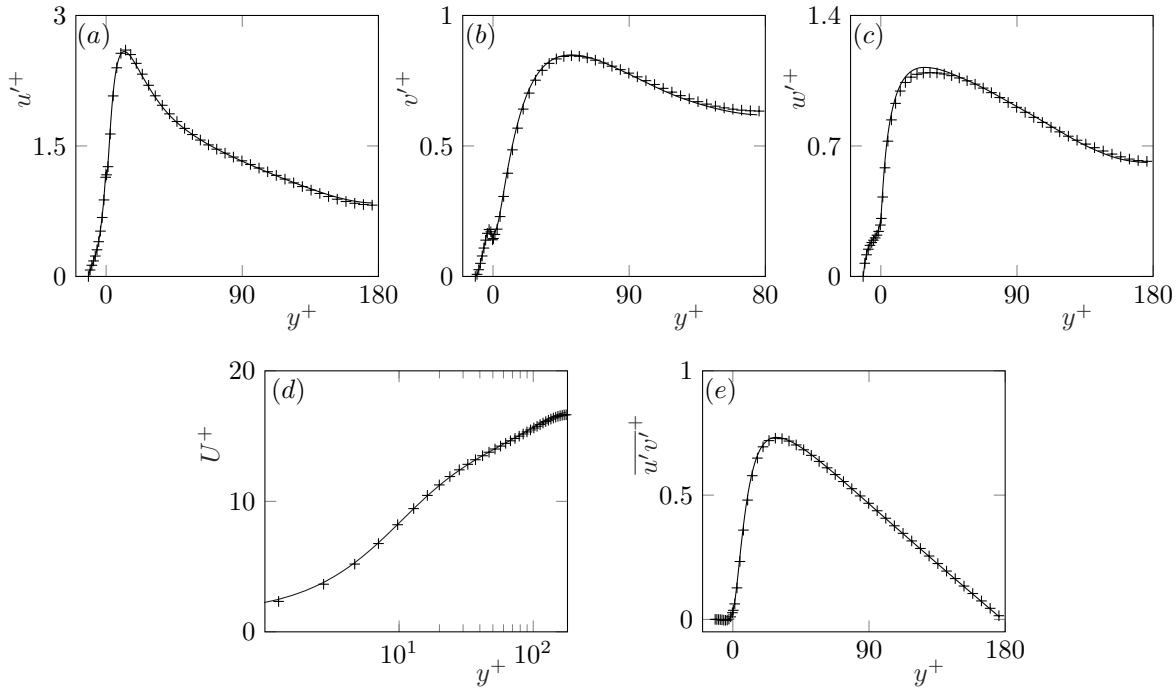

FIGURE 2.5 Rms velocity fluctuations, mean velocity and Reynolds shear stress profiles. The solid lines represent the results obtained from the present code, and the + symbols represent the data from Abderrahaman-Elena *et al.* (2019).

2.4 Validation

The numerical method used in the code, summarised in sections 2.1 and 2.2 has been validated by Fairhall & García-Mayoral (2018) and Fairhall *et al.* (2019). From the implementation of Fairhall & García-Mayoral (2018), only the immersed boundary algorithm has been added to the code. In order to validate the implementation of the immersed boundaries, we replicate the flow over the collocated roughness elements with height $h^+ \approx 12$ of Abderrahaman-Elena *et al.* (2019). The mean velocity profiles, rms fluctuations and the Reynolds shear stresses obtained from the present simulations show good agreement with the results of Abderrahaman-Elena *et al.* (2019), as shown in figure 2.5.

2.4.1 Grid independence

In the dense canopy simulations, the resolution requirements to adequately represent the coherent flow induced by the canopy elements is far more stringent than that required to resolve the turbulent scales. In order to determine the optimum resolution required to effectively represent the element induced flow, a grid independence study is conducted. Dense canopies with two plan-area ratios, λ_p, which is the ratio of the plan view area of the canopies to that of the full domain, are considered. For the representative canopy with $\lambda_p = 1/4$,

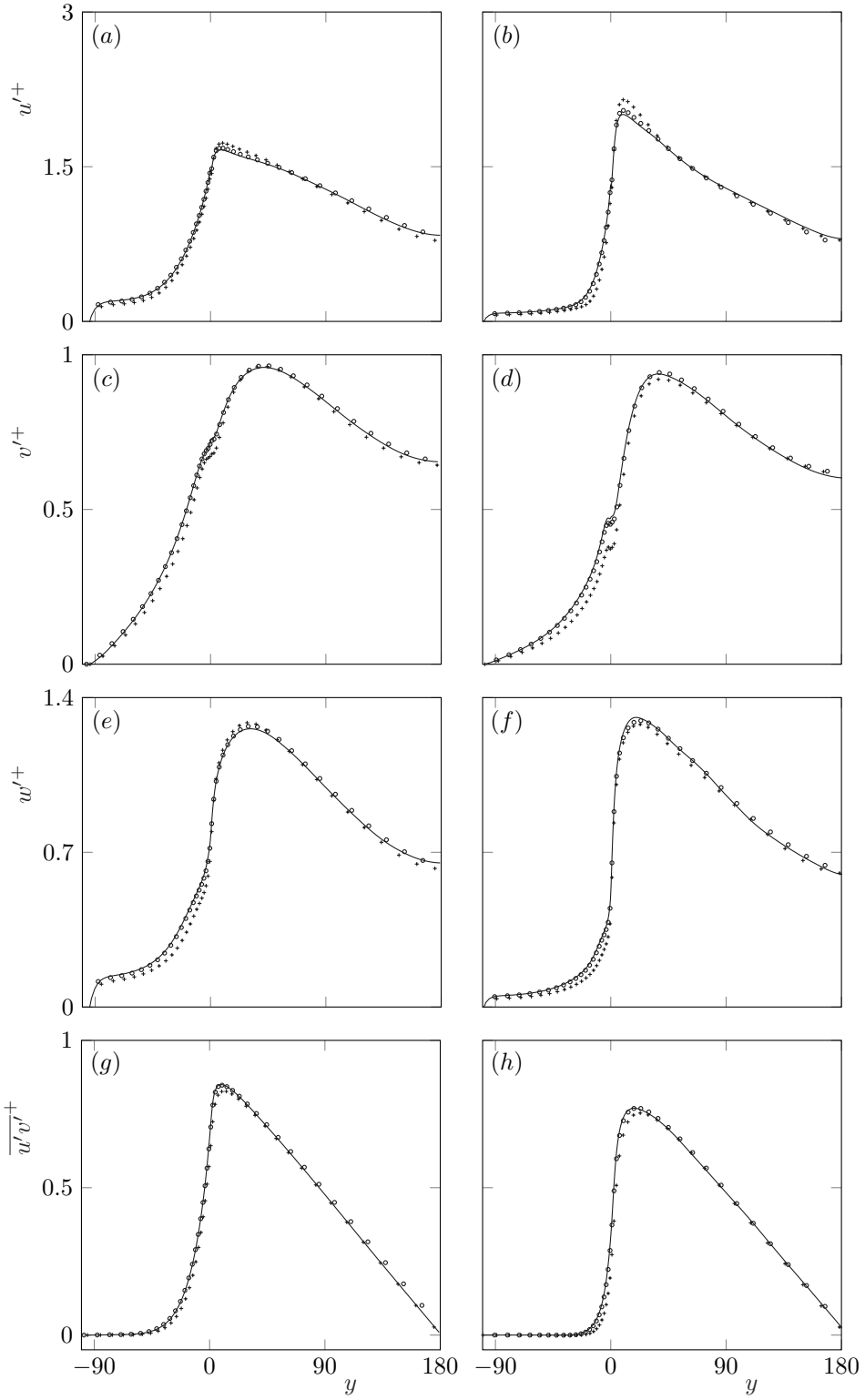

FIGURE 2.6 Rms velocity fluctuations and Reynolds shear stress profiles. The panels first column represent case G100 and those in the second column represent case S48. The solid lines in (a,c,e,g) represent the results from using 27 points per spacing; the symbols ○, 18 points; and +, 9 points per spacing. The solid lines in (b,d,f,h) represent the results from using 36 points per spacing; the symbols ○, 24 points; and +, 12 points per spacing.

resolutions per element spacing of 12, 24 and 36 points are considered. For the canopy with $\lambda_p \approx 1/20$, resolutions per element spacing of 9, 18 and 27 points are considered. The rms velocity fluctuations obtained from these simulations are portrayed in figure 2.6. The simulation results are grid independent at a resolution of 24 points per element spacing for the geometry with $\lambda_p = 1/4$, and 18 points per spacing for the geometry with $\lambda_p \approx 1/20$. The simulations with 9 and 12 points per spacing tend to under-predict the fluctuations within the canopies, with the maximum deviation observed in the wall-normal fluctuations of 20%. This difference reduces to 4% outside the canopy. These resolutions are only used for the densest canopy cases, where the fluctuations within the canopy are already very small and therefore, higher resolution simulations would not change the trends observed.

2.5 Drag-force methods

In the work concerning sparse canopies, in addition to representing the canopies using the immersed boundary method described in §2.3, some additional simulations are conducted where the canopy elements are modelled by a drag term which is a function of the local or mean velocity. There are two main types of drag-force simulations conducted, one where the drag is applied only within the region occupied by the canopy elements, and the other where the drag is applied homogeneously below the canopy-tip plane. We describe these models and their implementation in the DNS code here.

2.5.1 Representing permeable canopy elements

Certain natural canopies such as bushes or tree crowns allow some flow can pass through them, and a conventional immersed-boundary method may not provide a good representation for them. These permeable canopy elements can be better represented by applying a drag force in the region occupied by the canopy elements which does not enforce zero velocity within them (Yue *et al.*, 2007; Bailey & Stoll, 2013; Yan *et al.*, 2017). Such canopies are represented by including a drag force term, D, in the Navier-Stokes equations

$$\frac{\partial \mathbf{u}}{\partial t} + \mathbf{u} \cdot \nabla \mathbf{u} = -\nabla p + \frac{1}{Re}\nabla^2 \mathbf{u} - D \tag{2.18}$$

In discretised form, this equation can be written as

$$\begin{aligned}\left[\mathrm{I} - \Delta t \frac{\beta_k}{Re}\mathrm{L}\right]\mathbf{u}_k^n = \mathbf{u}_{k-1}^n + \Delta t \Bigg[\frac{\alpha_k}{Re}\mathrm{L}\mathbf{u}_{k-1}^n - \gamma_k[\mathrm{N}(\mathbf{u}_{k-1}^n) + D_{k-1}^n] - \\ \zeta_k[\mathrm{N}(\mathbf{u}_{k-2}^n) + D_{k-2}^n] - (\alpha_k + \beta_k)\mathrm{G}(p_k^n)\Bigg], k \in [1,3]\end{aligned} \tag{2.19}$$

The drag force is applied only at the grid points that are within the canopy elements and is of the form $D = C_{dc} u_i |u_i|$, similar to Yue *et al.* (2007), Bailey & Stoll (2013) and

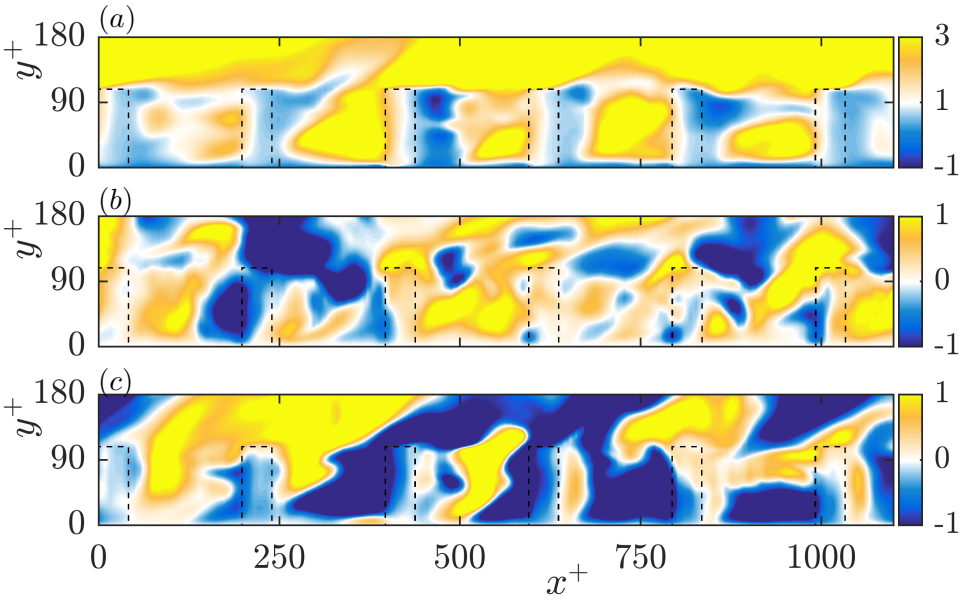

FIGURE 2.7 Instantaneous realisations of the (a) streamwise, (b) wall-normal and (c) spanwise velocities in a plane passing through the middle of the permeable canopy elements, scaled with the friction velocity.

Yan *et al.* (2017), where C_{dc} is a drag coefficient non-zero only for the grid points coincident with the canopy geometry, and u_i is the instantaneous local velocity in every i direction. C_{dc} is set such that further increasing its magnitude does not significantly increase the net drag force on the mean flow. This forcing provides a local body force opposing the flow inside the canopy elements and thus obstructs the flow within the canopy elements. Even so, the velocity of flow within the canopy elements can be up to 1–2u_τ, which is an order of magnitude larger than those within elements represented using the immersed boundary method. The flow velocities within the elements are illustrated in figure 2.7. With regard to the implementation of this drag in the code, the drag term is treated explicitly and calculated in physical space, similar to the non-linear products.

2.5.2 Homogenised-drag models

In order to explore the canopy-flow dynamics, some simulations are conducted where the canopy elements are replaced by a drag force applied homogeneously below the canopy-tip plane, and the shape of the canopy elements in the flow is not resolved. The first drag-force representation considered is a conventional, homogeneous drag model. In this case, the drag force in equation (2.18) is set to be of the form $D = C_{dh}u_i|u_i|$, where C_{dh} is a homogenised canopy drag coefficient which varies only in y. This drag force is applied homogeneously at all points below the canopy tips on all three velocity components. The method for obtaining C_{dh} is outlined in chapter 3. Although this drag is homogeneous, it is still calculated in

physical space as it too would be a convolution in Fourier space similar to the non-linear terms.

In addition, a drag force which only acts on the mean flow, and not the fluctuations is also considered. In this case, the drag applied is of the form $D = C_{dh}U|U|$, where $U(y)$ is mean in x and z of the streamwise velocity at any given timestep. While the drag used in the homogeneous-drag model, described in the previous paragraph, varies along any given wall-parallel plane depending on the local velocity, in the mean-only drag representation, the drag force is homogeneous along any given wall-parallel plane, as it depends only on the mean velocity and the drag coefficient at that height. In addition, as a statistically significant mean flow only exists in the streamwise direction in conventional channel flows, this drag is applied on the streamwise flow alone. This forcing is very simple to implement in the present code, where Fourier spectral discretisation is used for the wall-parallel directions. As all the Fourier modes are decoupled, the drag is simply calculated using and applied to the mean or zero-mode alone, leaving the other modes undisturbed.

Chapter 3

Turbulent flows over sparse canopies

In this chapter, we discuss the results obtained from direct numerical simulations of flows over sparse canopies. The canopies studied have equally spaced elements in the streamwise and spanwise directions, with spacings $s^+ \gtrsim 100$. The canopies also have low roughness frontal densities, $\lambda_f \lesssim 0.1$. The effect of the canopies on the flow both within and above the canopies is investigated. The domain considered, the canopy geometries studied and the simulations conducted are summarised in §3.1. The contribution of the flow induced by the presence of the canopy elements, referred to as the element-induced flow, is separated from the full flow. The remaining flow is termed the background-turbulence flow. For the background turbulence, the balance between the viscous and Reynolds shear stresses within the canopies is found to be similar to that over a smooth wall. Based on this, a new scaling based on the local sum of the Reynolds and viscous shear stresses at every height, τ_f, is proposed. In this local scaling, we observe that even the background-turbulence fluctuations show some similarities to smooth-wall flows. This scaling and the effect of the canopies on the surrounding turbulence are discussed in §3.2. The results suggest that the major effect of the canopies on the background turbulence is through a change in scale for the fluctuations, and that this scale is set by τ_f. In order to further investigate the canopy-flow dynamics, we also conduct some simulations where the canopy elements are substituted by a drag force. These simulations fall into two major categories, one where a homogenised drag force is used, which damps all the scales in the canopy region, and the other where the drag is only applied on the mean-flow alone and does not affect the fluctuations directly. Using these simulations, we show that τ_f, and consequently the background-turbulence fluctuations, can be captured by applying a drag on the mean-flow alone and not the fluctuations. These simulations provide support to the idea that a sparse canopy acts on the background turbulence mainly through a change it induces on the mean flow, which in turn determines τ_f. We also explore two modifications

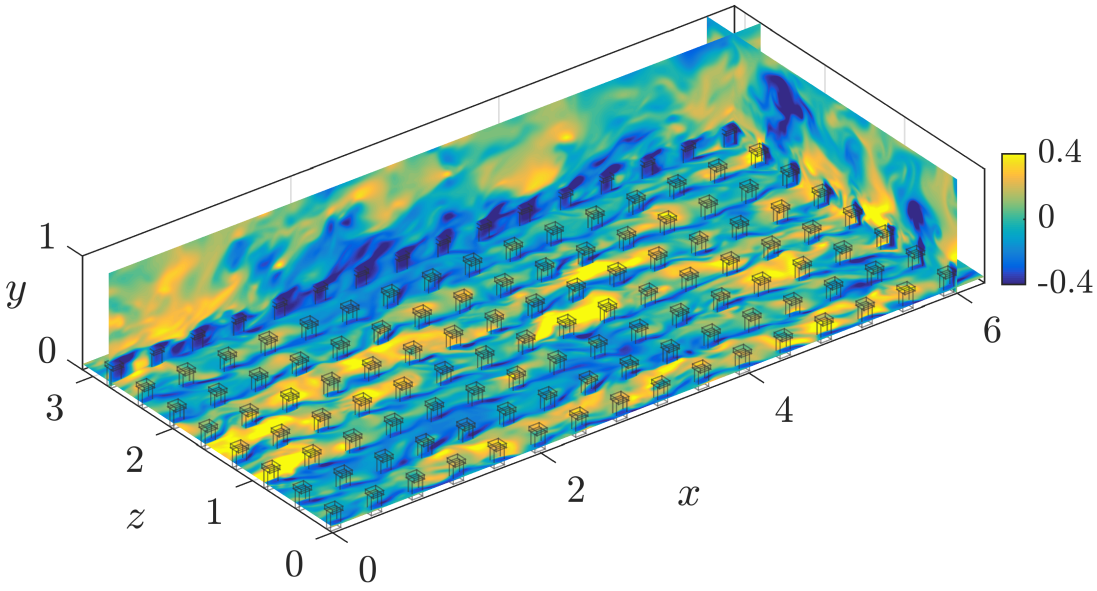

FIGURE 3.1 Schematic of the numerical domain. An instantaneous field of the fluctuating streamwise velocity from case TP1 is shown in three orthogonal planes.

of the mean-only drag. The first distributes this drag in a low-order representation of the canopies to capture a part of the element-induced flow. The second prescribes a mean velocity profile from a resolved canopy simulation and obtains the mean-only drag required to obtain this profile *a posteriori*. The results from these drag-force simulations are discussed in §3.3.

3.1 Numerical simulations

We conduct direct numerical simulations of an open channel with canopy elements protruding from the wall. The size of the simulation domain is $2\pi\delta \times \delta \times \pi\delta$, with the channel height $\delta = 1$. This box size has been shown to be adequate to capture one-point statistics up to the channel height for the friction Reynolds numbers used in the present study (Lozano-Durán & Jiménez, 2014). A schematic representation of the numerical domain is shown in figure 3.1. The domain is periodic in the x and z directions. No-slip and impermeability conditions are applied at the bottom boundary, $y = 0$, and free slip and impermeability at the top, $y = \delta$. It is shown in §3.2 that the height of the roughness sublayer for the canopies studied here extends to only half of the domain height, so the top boundary of the channel does not interfere with the canopy flow. As mentioned in chapter 2, the flow is incompressible with the density set to unity. All simulations are run at a constant mass flow rate, with the viscosity adjusted to obtain a friction Reynolds number based on the total stress $Re_\tau = u_\tau\delta/\nu \approx 520$.

	Case	$N_x \times N_z$	u_τ	Re_τ	s^+	λ_f	$\int D^+$	Δx^+	Δz^+
Smooth	S	–	0.055	538.8	–	–	–	8.8	4.4
Impermeable prismatic elements	P0	32×16	0.182	532.5	104	0.22	0.94	4.36	4.36
	P0-H	–	0.203	594.2	–	–	0.93	9.72	4.86
	P0-H0	–	0.227	549.4	–	–	0.90	8.99	4.49
	P1	16×8	0.138	520.3	204	0.05	0.79	4.26	4.26
	P1-H0	–	0.147	553.8	–	–	0.80	9.06	4.53
	P2	8×4	0.093	529.4	416	0.01	0.57	4.33	4.33
	P2-H0	–	0.092	522.9	–	–	0.57	8.55	4.28
Impermeable T-shaped elements	T1	16×8	0.133	505.6	199	0.07	0.80	4.14	4.14
	T1-H	–	0.160	503.3	–	–	0.85	11.00	5.50
	T1-H0	–	0.165	519.9	–	–	0.82	11.34	5.67
	T2	8×4	0.090	513.3	403	0.02	0.58	4.20	4.20
	T2-H0	–	0.097	527.4	–	–	0.60	8.63	4.31
Permeable T-shaped elements	TP1	16×8	0.160	505.5	199	0.07	0.81	8.27	4.14
	TP1-L	–	0.167	527.1	207	–	0.81	8.62	4.31
	TP1-H0F	–	0.205	646.0	–	–	0.883	10.57	5.28

Table 3.1 Simulation parameters. N_x and N_z are the number of canopy elements in the streamwise and spanwise directions, respectively, u_τ is the friction velocity based on the net drag scaled with the channel bulk velocity, Re_τ is the friction Reynolds number based on u_τ and δ. The element spacing is denoted by s and the roughness frontal density by λ_f. $\int D^+$ is the net canopy drag force scaled with u_τ, that is, the proportion of the total drag on the fluid exerted by the canopy elements, with the remainder being the friction at the bottom wall. The grid resolutions in the streamwise and spanwise directions are Δx^+ and Δz^+, respectively.

3.1.1 Canopy-resolving simulations

In these simulations, the canopy elements are assumed to be solid obstacles, and their geometry is resolved using an immersed-boundary method discussed in §2.3. The simulation parameters for the different cases studied here are summarised in table 3.1. Case S is an open channel with a smooth-wall floor. The canopy-resolving simulations include two canopy geometries, as portrayed in figure 3.2, with varying element spacings. The first geometry, denoted by the letter 'P', consists of collocated prismatic-posts with a square top-view cross-section with sides $l_x^+ = l_z^+ \approx 20$, and height $l_s^+ \approx 110$. The spacing between the canopy elements in the wall-parallel directions for cases P0, P1 and P2 are $s^+ \approx 100,\ 200$ and 400, respectively. The second geometry, denoted by the letter 'T', consists of frontally-extruded T-shaped canopies, as portrayed in figures 3.2(b) and (c). The head of these canopy elements has dimensions $l_x^+ = l_z^+ \approx 40$ in the wall-parallel directions. The base of the canopy elements has $l_x^+ \approx 40$ and $l_z^+ \approx 20$. The heights of the base and the head are $l_s^+ \approx 80$ and $l_h^+ \approx 30$, respectively. The canopy elements are in a collocated arrangement, and the spacing between the elements for cases T1 and T2 is $s^+ \approx 200$ and 400, respectively. Case TP1 has the same geometry and layout as T1, but the canopy elements are resolved using the local drag described in §2.5.1, and the resulting canopy elements allow some flow to pass through them, as shown in figure 3.2(c) and (f). The net mean drag force for this canopy is similar to that of the impermeable canopy, T1, as noted in table 3.1, in spite of the different character of the canopy elements.

The roughness densities of the canopies are given in table 3.1. All the canopies studied lie within the sparse to transitional regime empirically demarcated by Nepf (2012). As discussed in chapter 1, however, in turbulent flows, the roughness density may not a sufficient parameter to classify the canopy regimes, and the scales of the turbulent flow also need to be considered. In a smooth channel, the largest structures associated with the near-wall turbulent cycles are the streaks, which have spanwise widths of $\lambda_z^+ \approx 100$ (Kline *et al.*, 1967). The spanwise spacings between the canopy elements are therefore set to be at least $s^+ \gtrsim 100$. This implies that the canopies should be sparse from the point of view of the near-wall turbulent fluctuations as well.

3.1.2 Drag-force representations

In order to explore the canopy-flow dynamics, we also conduct simulations where the canopy is replaced by some drag force that does not resolve the geometry of the canopy elements, as discussed in §2.5.2. Sparse canopies consisting of bluff elements, such as those in the present work, are generally better characterised by a quadratic drag (Coceal *et al.*, 2008), whereas for dense canopies where viscous effects dominate a drag force proportional to the velocity would be more appropriate (Tanino & Nepf, 2008). Therefore, in the present study, the canopy

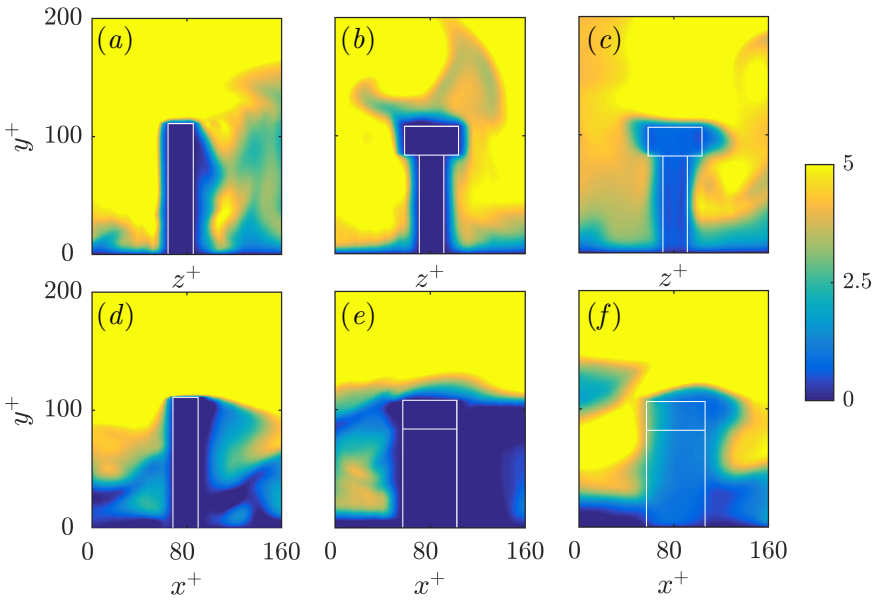

FIGURE 3.2 Contours of instantaneous streamwise velocity in planes passing through the centre of a canopy element. (a–c) represent cuts in the z–y plane, and (d–f) represent cuts in the x–y plane. (a,d) cuboidal canopy elements from case P1; T-shaped canopy elements from (b,e) case T1 and (c,f) case TP1. The white lines mark the positions of the canopy elements. The contours are scaled using the global friction velocity, u_τ, of each case.

elements are replaced by a quadratic drag force, that is, where the drag is proportional to the square of the velocity.

The drag coefficient, C_{dh}, is obtained by approximating the canopy drag force obtained from the canopy-resolving simulations, D, to a form $D \approx C_{dh}U|U|$, where U is the mean streamwise velocity. The drag coefficients obtained from cases T1, TP1 and T2 are portrayed in figure 3.3. This quadratic form provides a reasonable approximation of the drag force for $y^+ > 20$, once viscous effects are small. This is consistent with observations made in previous studies (Coceal *et al.*, 2008; Böhm *et al.*, 2013).

For the simulations labelled with the suffix '-H', the presence of the canopy is replaced by a force $C_{dh}u_i|u_i|$ applied homogeneously below the canopy tips. This is the conventional homogeneous-drag model. It also requires the prescription of drag coefficients in the spanwise and wall-normal directions. We estimate these by rescaling the streamwise drag coefficient based on the relative change in the 'blockage ratio' of the canopy elements in the different directions (Luhar *et al.*, 2008), in the spirit of the method proposed by Luhar & Nepf (2013). The blockage ratio in each direction is proportional to the frontal area of the canopy elements in that direction. In the wall-normal and spanwise directions, this would be the top-view and the side-view areas respectively. For the wall-normal drag, this assumption is particularly coarse, but Busse & Sandham (2012) have shown that the flow is relatively insensitive to moderate changes in the wall-normal drag coefficient. In the simulations labelled with the

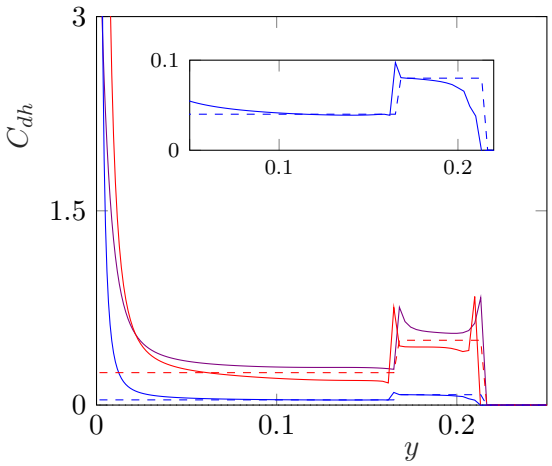

FIGURE 3.3 Drag coefficients, $C_{dh} = D/U^2$, obtained from 'T' shaped canopies. —, case T1; —, case TP1; —, case T2; - - -, cases T1-H/H0; and - - -, case T2-H0. The inset provides a magnified view of the drag coefficients for cases T2 and T2-H0.

suffix '-H0', a forcing $C_{dh}U|U|$ is applied in the region below the canopy tips, where $U(y)$ is the mean velocity profile. The drag is only applied to the mean-streamwise velocity and has no fluctuating component. The simulation labelled with the suffix '-L' applies a drag $C_{dh}U|U|$ on the streamwise mean-flow alone, as in cases H0, but distributed in a reduced-order representation of the canopy elements, which consists of a 24-mode, x-z Fourier-truncation of the canopy geometry. Finally, another variant of the mean-only drag, labelled with the suffix '-H0F', prescribes the mean velocity profile from the resolved canopy simulation, and obtains the mean-only drag required to sustain this mean profile *a posteriori* (Tuerke & Jiménez, 2013).

3.2 Canopy-resolving simulations

In this section, we present and discuss the scaling of turbulent fluctuations in sparse canopies, and compare them with those over a smooth wall. Over a smooth wall, the balance of stresses within the channel can be obtained by averaging the momentum equations in the wall-parallel directions and time and integrating in y, which yields

$$\frac{\mathrm{d}P}{\mathrm{d}x}y + \tau_w = -\overline{uv} + \nu\frac{\mathrm{d}U}{\mathrm{d}y}, \tag{3.1}$$

where τ_w is the wall shear stress, $\mathrm{d}P/\mathrm{d}x$ is the mean streamwise pressure gradient, $-\overline{uv}$ is the Reynolds shear stress, U is the mean streamwise velocity, and ν is the kinematic viscosity. At $y = \delta$, equation (3.1) yields the expression for the wall shear stress and the friction velocity,

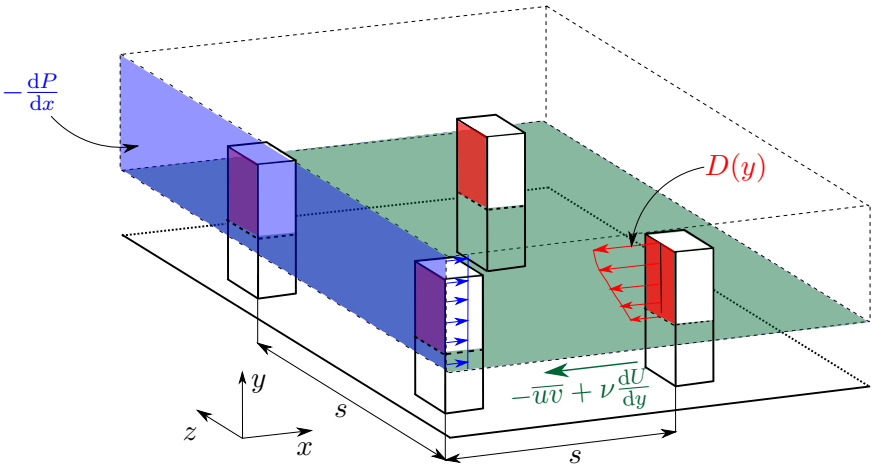

FIGURE 3.4 Schematic representation of the stress balance in a channel with canopy elements.

u_τ,

$$u_\tau^2 = \tau_w = -\delta\frac{\mathrm{d}P}{\mathrm{d}x}. \tag{3.2}$$

In the presence of a canopy, the stress balance also includes the drag exerted by the canopy elements,

$$\frac{\mathrm{d}P}{\mathrm{d}x}y + \tau_w \quad = \quad -\overline{uv} + \nu\frac{\mathrm{d}U}{\mathrm{d}y} - \int_0^y D\ \mathrm{d}y, \tag{3.3}$$

where the canopy drag averaged in x, z and time, D, is zero for $y > h$. Equation (3.3) can be rewritten as

$$\frac{\mathrm{d}P}{\mathrm{d}x}y + \tau_w + \int_0^h D\ \mathrm{d}y \quad = \quad -\overline{uv} + \nu\frac{\mathrm{d}U}{\mathrm{d}y} + \int_y^h D\ \mathrm{d}y, \tag{3.4}$$

so that the net drag, $\tau_w + \int_0^h D\ \mathrm{d}y$, is on the left-hand side, as in (3.1). From this net drag, a 'global' friction velocity can be defined,

$$u_\tau^2 = \tau_w + \int_0^h D\ \mathrm{d}y \quad = \quad -\delta\frac{\mathrm{d}P}{\mathrm{d}x}. \tag{3.5}$$

This is the equivalent of the smooth-wall u_τ of equation (3.2) for canopy flows. While in smooth-wall flows the total stress is the sum of the viscous and Reynolds shear stresses alone and is linear in y, in canopy flows that linear sum has an additional contribution from the canopy drag as evidenced by the right-hand-side of equation (3.4). This equation also portrays that, at any given height y, the sum of the streamwise shear stresses, $-\overline{uv}+\nu\mathrm{d}U/\mathrm{d}y$, and the drag from the canopy above that height, $\int_y^h D\ \mathrm{d}y$, are balanced by the force exerted by the pressure gradient above, as portrayed in figure 3.4. Outside the canopy, the drag term

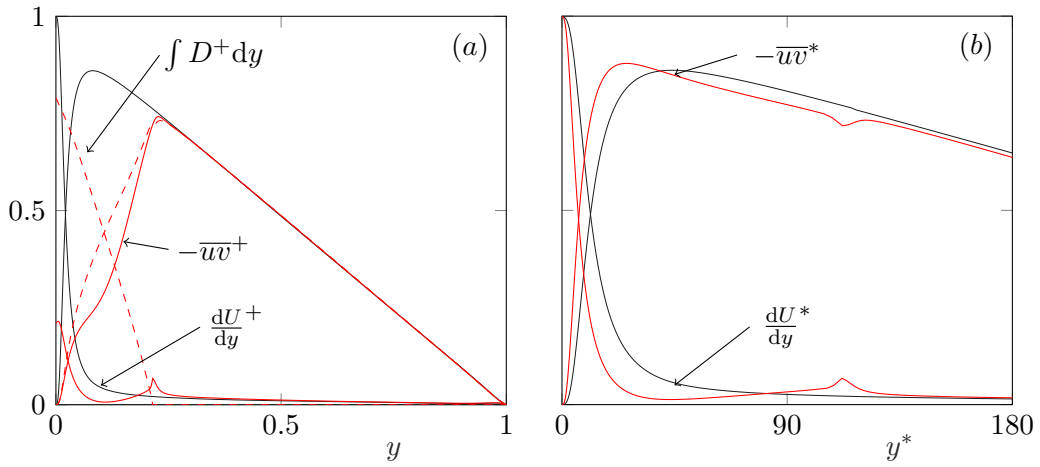

FIGURE 3.5 Stress profiles within the channel scaled with (a) u_τ and (b) u^* for case P1. Dashed and solid red lines represent the full and background turbulent Reynolds shear stresses, $-\overline{u'v'}$ and $-\overline{u''v''}$, respectively. The thin black lines represent the smooth-wall case, S.

is zero, and the magnitude of the viscous and Reynolds shear stresses is similar to that over smooth walls. Within the canopy, however, the canopy drag can dominate, and the viscous and Reynolds shear stresses are smaller than over smooth walls, as shown in figure 3.5(a).

As can be observed in figure 3.1, the presence of the canopy elements induces a coherent flow. Several studies have shown that the flow around the canopy elements and the flow far away from them have significantly different characteristics, and consequently they are typically studied separately (Finnigan, 2000; Böhm *et al.*, 2013; Bailey & Stoll, 2013). A commonly used technique to separate the element-induced flow from the background turbulence is through triple decomposition (Reynolds & Hussain, 1972)

$$\boldsymbol{u}(\boldsymbol{x},\boldsymbol{y},\boldsymbol{z},\boldsymbol{t}) = \boldsymbol{U}(\boldsymbol{y}) + \boldsymbol{u'}(\boldsymbol{x},\boldsymbol{y},\boldsymbol{z},\boldsymbol{t}), \tag{3.6}$$

$$\boldsymbol{u'}(\boldsymbol{x},\boldsymbol{y},\boldsymbol{z},\boldsymbol{t}) = \widetilde{\boldsymbol{u}}(\boldsymbol{x},\boldsymbol{y},\boldsymbol{z}) + \boldsymbol{u''}(\boldsymbol{x},\boldsymbol{y},\boldsymbol{z},\boldsymbol{t}), \tag{3.7}$$

where $\boldsymbol{u}$ is the full velocity, $\boldsymbol{U}$ is the mean velocity obtained by averaging the flow in time and space, and $\boldsymbol{u'}$ is the full space-and-time fluctuating velocity. The latter is decomposed into the element-induced, dispersive velocity, $\widetilde{\boldsymbol{u}}$, which is obtained by averaging the flow in time alone, and the incoherent, background-turbulence fluctuating velocity $\boldsymbol{u''}$. A method analogous to triple decomposition, called 'double averaging' (Raupach & Shaw, 1982), can also be used to separate the element-induced and background-turbulence flows (Finnigan, 2000; Nepf, 2012; Bai *et al.*, 2015; Giometto *et al.*, 2016; Yan *et al.*, 2017).

The intensity of the element-induced flow can vary with the shape (Balachandar *et al.*, 1997; Taylor *et al.*, 2011), permeability (Yu *et al.*, 2010; Ledda *et al.*, 2018), and distribution of the canopy elements. It is possible, however, for canopies to have different element-

induced flows but similar background turbulence. To illustrate this, we compare two canopy simulations, T1 and TP1, which have similar canopy layouts and roughly the same net drag, as shown in figure 3.6(h). The difference between the two cases is that in T1 the canopy elements are impermeable, whereas in TP1 some flow penetrates into the elements. The rms fluctuations of the full and background-turbulence velocity components for these cases are shown in figure 3.6. The magnitude of the full streamwise fluctuations within the canopy is significantly larger for T1 than for TP1. This increase, however, can be attributed essentially to the stronger element-induced fluctuations generated by the impermeable canopy elements. This is evidenced by the fact that the background-turbulence streamwise fluctuations for both cases essentially collapse, as shown in figure 3.6(b). The cross-flow fluctuations and Reynolds shear stress profiles for both these canopies are also similar. The impermeable canopy, however, has a slightly larger damping effect on the spanwise fluctuations.

The fluctuating velocities portrayed in figure 3.6 are scaled using the 'global' friction velocity defined by equation (3.5), which includes the full contribution of the canopy drag. Tuerke & Jiménez (2013) studied smooth-wall flows with artificially forced mean profiles, and observed that the turbulent fluctuations in such flows scaled with the local sum of the viscous and Reynolds shear stresses, or the local stress τ_f, at each height. This was the case even when τ_f was not linear with y due to the artificial forcing. Tuerke & Jiménez (2013) defined a 'local' friction velocity, u^*, by linearly extrapolating the local stress at each height to the wall,

$$u^*(y)^2 = \frac{\delta}{\delta - y}\tau_f(y). \tag{3.8}$$

Notice that, for a smooth unforced channel, $u^* = u_\tau$ at every height. Following Tuerke & Jiménez (2013), we define the sum of the viscous and background-turbulence Reynolds stresses as τ_f. In the present work, we only discuss the scaling of the background-turbulence fluctuations. Hence, only the contribution of the background-turbulence Reynolds shear stresses to τ_f are considered. A similar concept was also proposed by Högström *et al.* (1982) for flows over urban canopies. They scaled turbulence with a local friction velocity, defined as the square root of the magnitude of the local Reynolds shear stress, but had measurements only at heights where the contribution of the viscous stress to τ_f would be small. Using u^*, a local viscous lengthscale can also be defined, ν/u^*, and from it an effective viscous height, $y^* = yu^*/\nu$. Both u^* and y^* for the prismatic-post canopies are portrayed in figure 3.7. Near the canopy tips, where the element-induced drag is no longer present, the local friction velocity, u^* becomes equal to the global u_τ, and y^* becomes equal to y^+. Making the canopy sparser reduces the canopy drag, and hence the difference between u^* and u_τ within the canopy reduces with increasing canopy sparsity.

When scaled with u_τ, as is done conventionally, the viscous and Reynolds shear stresses near the base of the canopy are highly damped compared to smooth walls. However, the balance of these stresses in τ_f remains close to that over smooth walls. This is illustrated in

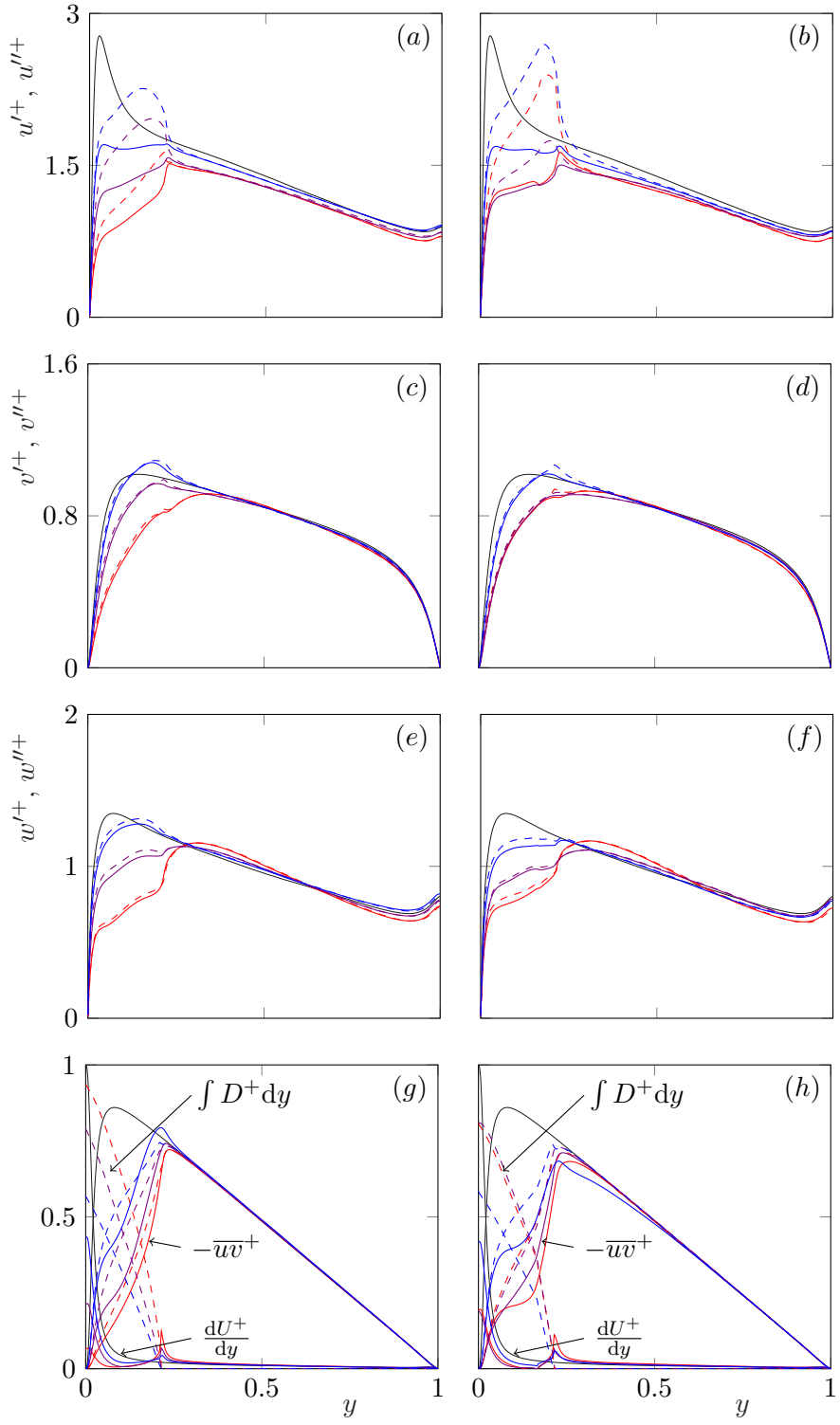

FIGURE 3.6 Rms velocity fluctuations and shear stresses scaled with the global friction velocity, u_τ, from the canopy-resolving simulations. In the left column, the lines represent —, case P0; —, case P1; and —, case P2. In the right column, the lines represent —, case T1; —, case TP1; and —, case T2. Dashed lines represent the full velocity fluctuations, $\boldsymbol{u'}$, and solid lines represent the background-turbulence fluctuations, $\boldsymbol{u''}$. The thin, solid black lines represent the smooth-wall case, S, for reference.

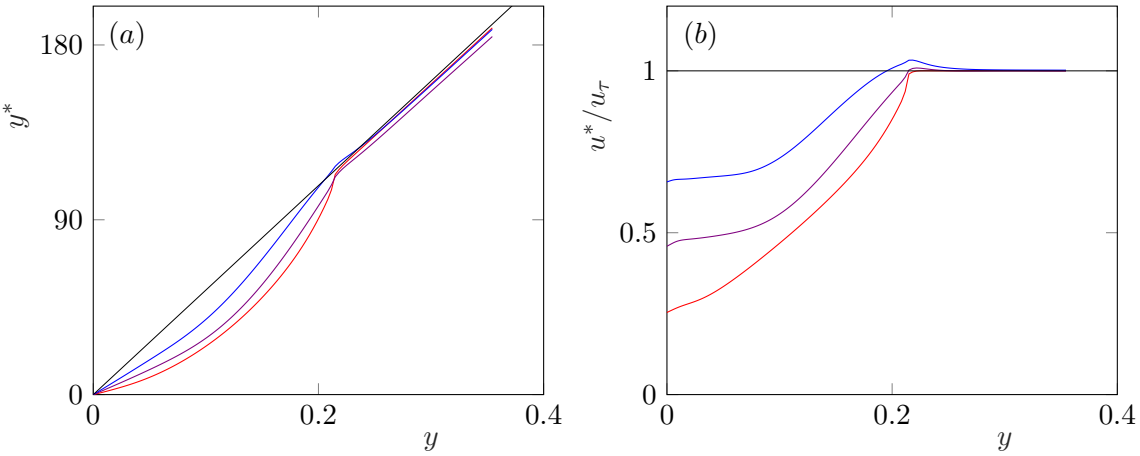

FIGURE 3.7 Variation of (a) y^*, and (b) u^* with height for the prismatic-post canopies, with sparsity increasing from red to blue. —, denser case P0; —, intermediate case P1; —, sparser case P2; and —, smooth-wall case, S.

figure 3.5, which portrays the terms in the stress balance within a channel with canopies scaled with u_τ and u^*. The similarity of the viscous and Reynolds shear stresses in the canopy-flow and smooth-wall cases suggests that the canopy acts on the background turbulence essentially through changing their local scale, rather than through a direct interaction of the canopy elements with the flow. To explore the scaling further, the background-turbulence rms fluctuations are portrayed scaled with u^* in figure 3.8. Scaling the fluctuations with the conventional u_τ shows a reduction of the fluctuations within the canopy compared to a smooth wall, as shown in figure 3.6. With our proposed scaling with u^*, in contrast, the streamwise fluctuations appear similar to those in a smooth channel. The increase in spanwise and wall-normal fluctuations, shown in figures 3.8$(c$–$f)$, suggests, however, that there is a relative increase in the intensity of the cross flow within the canopy compared to a smooth channel.

Although u''^* and $\overline{u''v''}^*$ within the canopy appear similar to those over smooth walls, there are some differences in the distribution of energy across different lengthscales in the flow, particularly in the region close to the wall. In order to examine this, we compare the spectral energy densities, at $y^* \approx 15$, for a smooth-wall and for case P1 in figure 3.9. This is the height roughly corresponding to the location at which the magnitude of the fluctuations peaks in smooth-wall flows (Jiménez & Pinelli, 1999). In global units, the energy is observed to be in larger wavelengths when compared to a smooth channel, especially in λ_z. In local scaling, however, there is a greater overlap of the regions with the highest intensity, particularly for E_{uu} and E_{uv}. In addition, the canopy case exhibits a concentration of energy at the canopy wavelengths and its harmonics. Note that the element spacing, for case P1, at $y^* \approx 15$ is reduced to $s^* \approx 100$, while in global scaling it is $s^+ \approx 200$. The increase in the energy in the canopy wavelengths is a reflection of the element-induced flow. The large streamwise

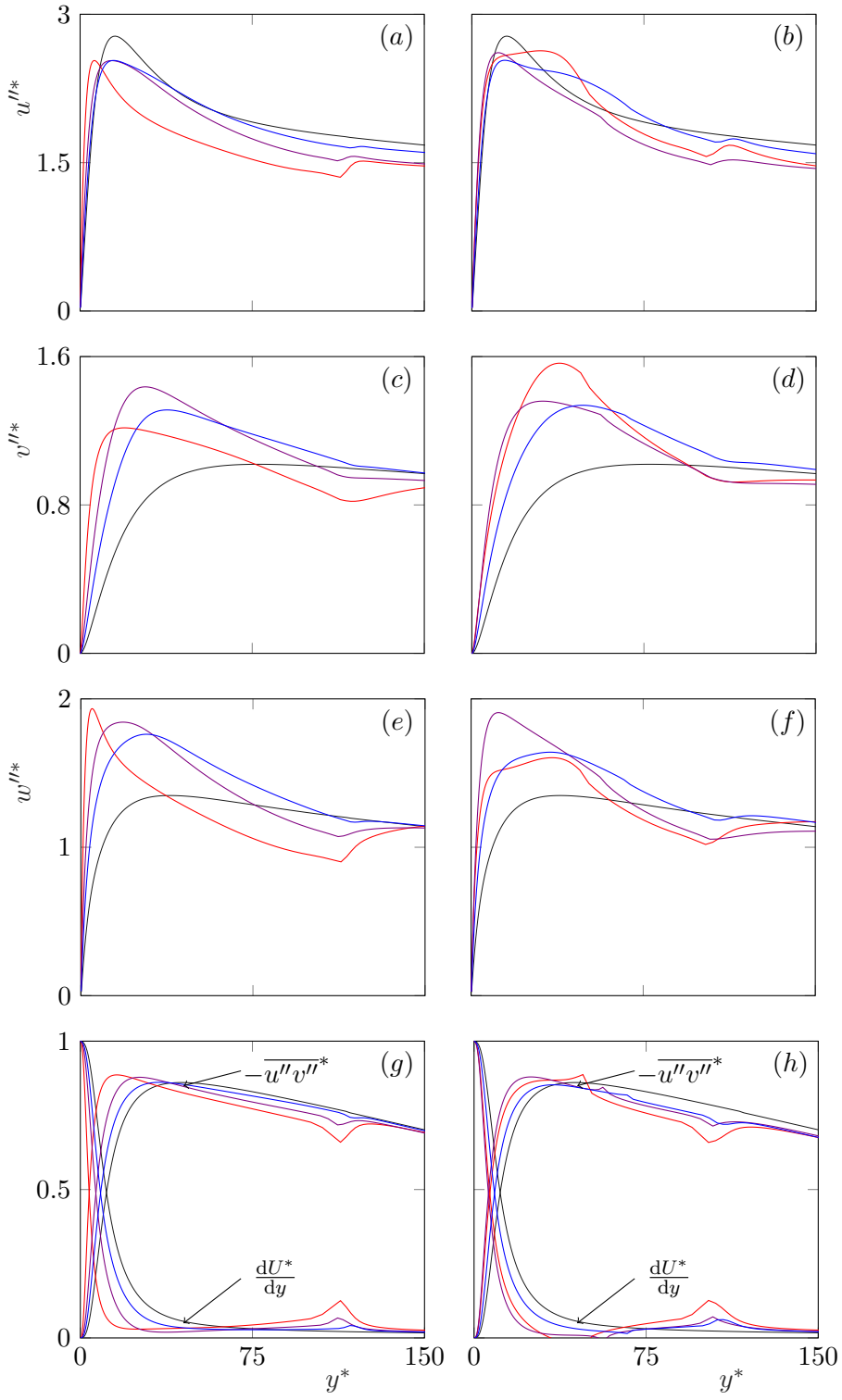

FIGURE 3.8 Rms velocity fluctuations and shear stresses for the background turbulence scaled using the local friction velocity, u^*, from the canopy-resolving simulations. The lines in the left column represent —, case P0; —, case P1; and —, case P2. In the right column, the lines represent —, case T1; —, case TP1; and —, case T2. The thin black lines represent the smooth-wall case, S.

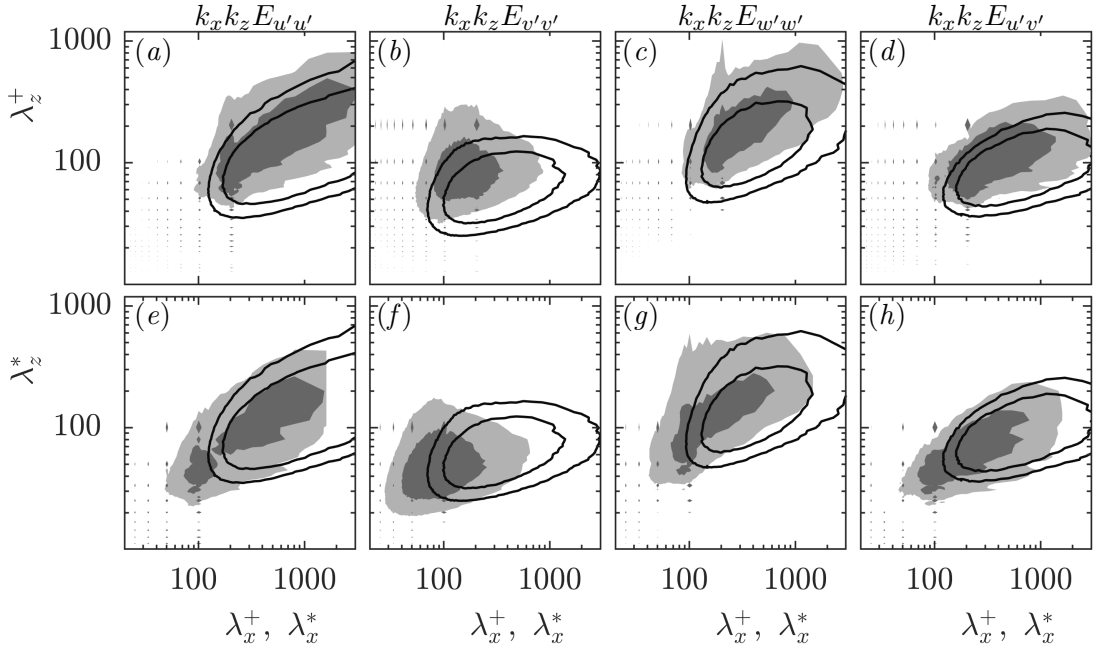

FIGURE 3.9 Pre-multiplied spectral energy densities of the full velocity fluctuations for case P1 (filled contours) and for case S (line contours) normalised with their respective rms values at (*a–d*) $y^+ \approx 15$, and (*e–h*) $y^* \approx 15$. The contours from the left to right columns are in increments of 0.03, 0.06, 0.05 and 0.06, respectively.

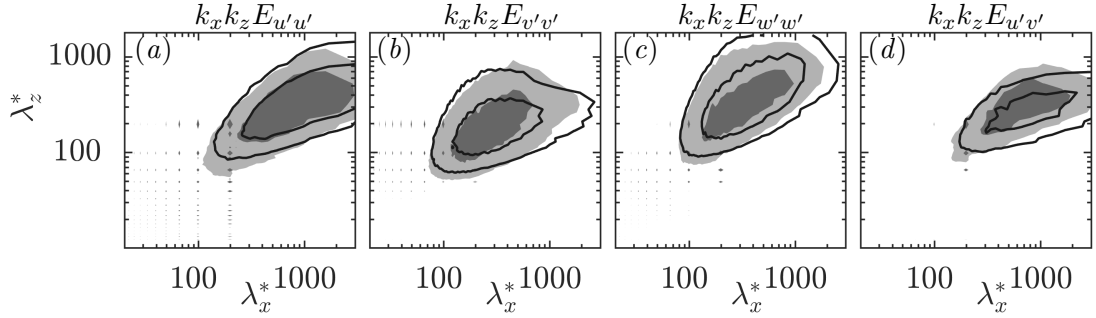

FIGURE 3.10 Pre-multiplied spectral energy densities of the full velocity fluctuations for case P1 (filled contours) and case S (line contours) at $y^* \approx 105$, normalised by their respective u^*. The contours in (*a–d*) are in increments of 0.125, 0.06, 0.075 and 0.06, respectively.

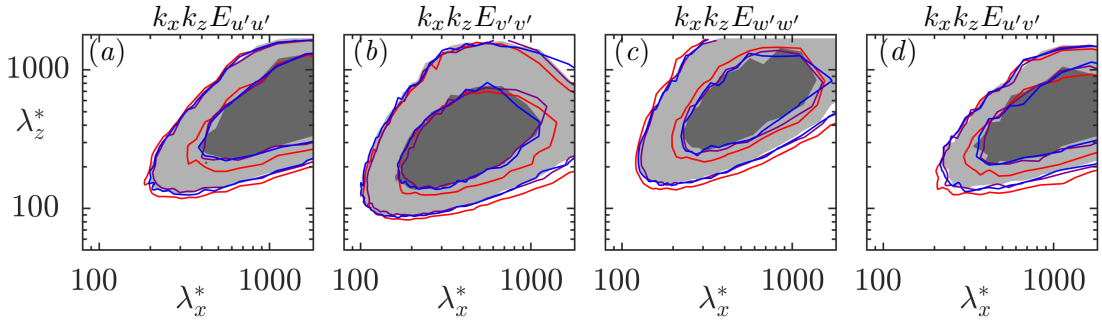

FIGURE 3.11 Pre-multiplied spectral energy densities of the full velocity fluctuations at $y^+ \approx 250$. —, case P0; —, case P1; and —, case P2, normalised by their respective u_τ. Filled contours represent case S. The contours in (a–d) are in increments of 0.075, 0.04, 0.06 and 0.03, respectively.

scales, in turn, are damped by the presence of the canopy, which results in a reduction of their energy. The differences in the energy distribution observed within the canopy eventually disappear above it. To illustrate this, figure 3.10 portrays the spectra near the canopy tips, $y^* \approx 105$. Here, the concentration of energy in the canopy wavelengths and its harmonics is weak, and the smaller scales in the flow are smooth-wall-like.

There is, however, still a deficit of energy in large streamwise wavelengths, compared to a smooth wall, associated with the damping of these scales by the canopy elements, as discussed in the previous paragraph. This effect diminishes away from the canopy, and the spectra are essentially smooth-wall-like for $y^+ \gtrsim 250$, as shown in figure 3.11, indicating that outer-layer similarity is recovered and delimiting the height of the roughness sublayer. The recovery of outer-layer similarity is also reflected in the mean-velocity profiles of the canopy flow simulations, portrayed in figure 3.12, which exhibit logarithmic-law behaviour with a standard Kármán constant when shifted by a suitable displacement height, d (Jackson, 1981).

So far, we have mainly focussed on the results for case P1, with prismatic canopy elements with spacings $s^+ \approx 200$. We now discuss the effect of changing the canopy element geometry and spacing on the flow. An increased sparsity results in an increase in the magnitude of both the full and background-turbulent velocity fluctuations, as shown in figure 3.6. In local scaling, however, the background turbulent fluctuations follow a similar trend to that observed for case P1. We observe that u''^* and $\overline{u''v''}^*$ appear smooth-wall-like, while there is a relative increase in the magnitude of the cross fluctuations. For the denser canopy of case P0, on the other hand, the fluctuations become less similar to those over smooth-walls. The streamwise fluctuations are damped more intensely within the canopy, and there are additional Reynolds shear stresses near the wall. Figure 3.13 shows that, compared to the sparser canopies, P0 has an accumulation of energy in streamwise wavelengths corresponding to the canopy harmonics but across a range of spanwise wavelengths. These regions of excess

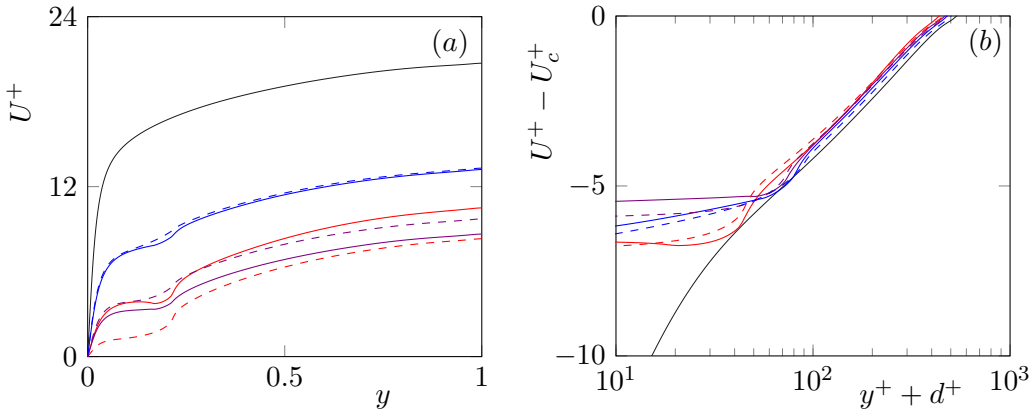

FIGURE 3.12 Mean velocity profiles, from the canopy-resolving simulations. Lines represent —, case T1; —, case TP1; —, case T2; - - -, case P0; - - -, case P1; - - -, case P2. The black lines represent the smooth-wall case, S. U_c is the mean velocity at $y = \delta$, and d is a displacement height.

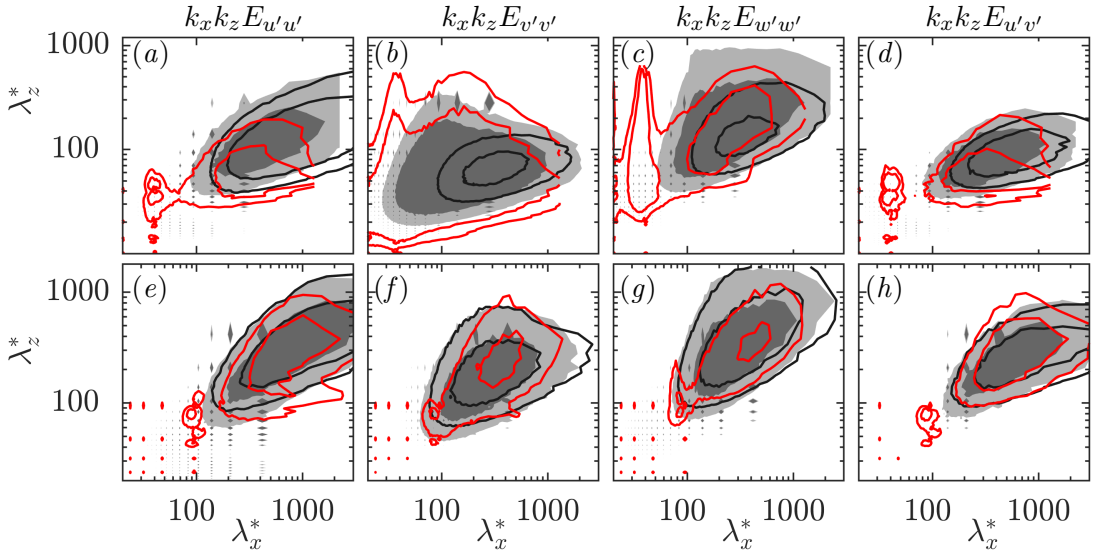

FIGURE 3.13 Pre-multiplied spectral energy densities of the full velocity fluctuations at (*a–d*) $y^* \approx 15$ and (*e–h*) $y^* \approx 105$, normalised by their respective u^*. Filled contours represent case P2; —, case S; and —, case P0. The contours in (*a–h*) are in increments of 0.3, 0.03, 0.1, 0.06, 0.12, 0.06, 0.075 and 0.05, respectively.

energy have also been noted by Abderrahaman-Elena *et al.* (2019), who studied densely packed cuboidal roughness. They noted that these regions were an imprint of the large, background-turbulence scales modulating the smaller scale coherent flow generated by the roughness. This effect diminishes as the canopy element spacing is made larger than the energetic scales in the background-turbulence, as evidenced by the lack of these regions in the spectra of the sparser canopies portrayed in figures 3.9, 3.10 and 3.13. For case P2, the spectra are already close to smooth-wall-like at the canopy tips, suggesting that both the element-induced flow and the damping of large scales are already weak at this height.

Previous studies have noted the formation of Kelvin–Helmholtz-like instabilities near the canopy tips in dense canopies (Finnigan, 2000; Nepf, 2012; Bailey & Stoll, 2016). These instabilities originate from an inflection point in the mean-velocity profile over canopies (Raupach *et al.*, 1996). The T-shaped canopies were originally designed as a flow control device, aiming to produce a strong inflection point at the canopy tips in order to generate these instabilities, while leaving the near-wall flow relatively undisturbed (Sharma & García-Mayoral, 2018). When present, these instabilities leave a distinct footprint in E_{vv} and E_{uv}, causing an increase in energy in a narrow range of streamwise wavelengths and for large spanwise wavelengths (García-Mayoral & Jiménez, 2011; Gómez-de-Segura *et al.*, 2018*a*; Abderrahaman-Elena *et al.*, 2019). However, such a footprint is not observed in the canopies studied here, consistent with the observations of Poggi *et al.* (2004) for sparse canopies. This suggests that, even if the instabilities are present over these sparse canopies, they are weak compared to the other fluctuations in the flow, and are therefore masked by them.

3.3 Simulations with artificial forcing

The results discussed so far suggest that sparse canopies affect their surrounding flow through two mechanisms, an element-induced flow, and a change in the local scale for the background-turbulence fluctuations. With respect to the second mechanism, the effect of the canopy elements would be indirect, through modifying the mean-velocity profile and thus the local stress, τ_f. The latter would, in turn, set the scale for the fluctuations. If this is the case, applying the mean drag produced by the canopy on the mean flow alone should capture the essential effects of the canopy on the background-turbulence. We test this in the simulations labelled with the suffix '-H0'. For the densest canopies simulated for each geometry, that is, P0 and T1/TP1, we also compare the mean-only-drag simulations with conventional, homogeneous drag simulations labelled with the suffix '-H'. Note that simulations T1-H0 and T1-H correspond to both the permeable and impermeable canopies of T1 and TP1, as they have similar net drags and drag coefficients. Note that the homogeneous and mean-only drag simulations do not produce an element-induced flow, that is, $\widetilde{\boldsymbol{u}} = 0$, and therefore, the full and background-turbulence components of the fluctuations for these simulations are equal, $\boldsymbol{u}' = \boldsymbol{u}''$.

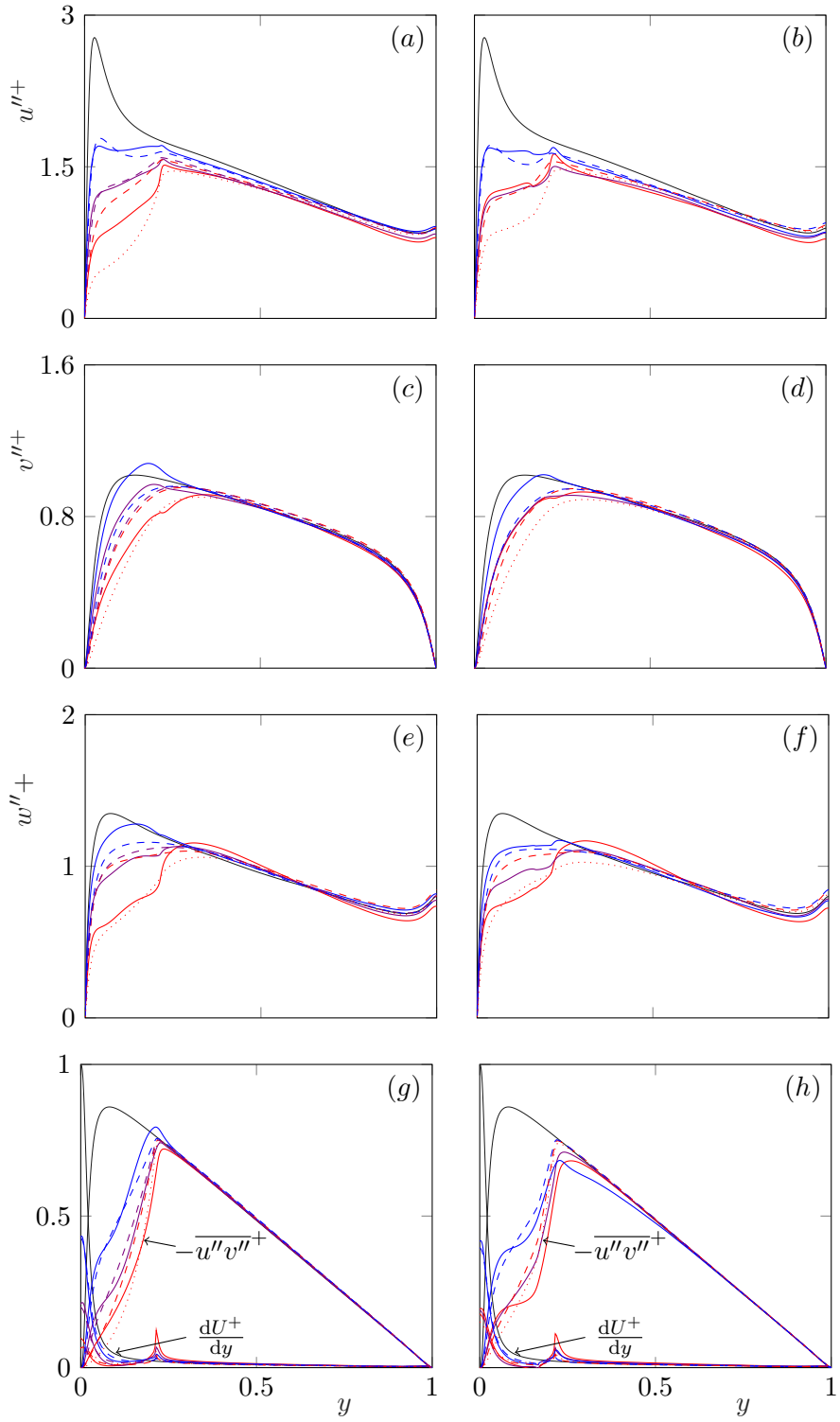

FIGURE 3.14 Rms velocity fluctuations and shear stresses for the background turbulence scaled with the global friction velocity, u_τ, of the canopy-resolving, mean-only drag and homogeneous drag simulations. In the left column, lines represent ——, case P0; - - -, case P0-H0; ·····, case P0-H; ——, case P1; - - -, case P1-H0; ——, case P2; and - - -, case P2-H0. In the right column, lines represent ——, case T1; - - -, case T1-H0; ·····, case T1-H; ——, case TP1; ——, case T2; and - - -, case T2-H0. The thin black line represents the smooth-wall case, S.

The streamwise fluctuations and the Reynolds shear stresses of the mean-only-drag simulations are in good agreement with the corresponding background-turbulence fluctuations from the resolved canopies, except for the densest canopy studied, case P0, as shown in figure 3.14. For the sparsest canopies, cases P2 and T2, the cross-flow fluctuations, particularly in the wall-normal direction, are slightly larger than their mean-only-drag counterparts. A likely reason for this discrepancy is the presence of an unsteady element-induced flow for these canopies, whose contribution cannot be filtered out by the conventional triple-decomposition technique that we have used. The fluctuating velocities scaled by the local friction velocities for the drag-force simulations show similar trends to that observed for the canopy resolved simulations, that is, u'' and $\overline{u''v''}$ show similarities to those of smooth channels, and that there is a general increase in v'' and w''. The fluctuations, in local scale, for the drag-force simulations are provided in figure 3.15, for reference.

For case P0, a homogeneous drag provides a better representation of the cross-flow fluctuations than the mean-only drag, and the streamwise fluctuations are not well represented by either forcing method. For this case, there is significant interaction between the element-induced flow and the background turbulence, as discussed in §3.2. Thus, it is not surprising that neither the mean-only drag nor the homogeneous drag is able to capture the full effect of this canopy on the background turbulence.

For the sparser canopies of T1 and TP1, compared to a mean-only drag, the homogeneous drag tends to overdamp the fluctuations within the canopy, particularly in the streamwise direction, as can be observed in figure 3.14(b). The excessive damping of fluctuations by a homogeneous drag, in comparison to a resolved canopy, was also noted by Yue *et al.* (2007) and Bailey & Stoll (2013). Figure 3.16 shows that this decrease in the intensity of fluctuations within the canopy is mainly a result of damping of the smaller streamwise wavelengths in the flow, $\lambda_x^* \lesssim 200$. The homogeneous drag simulation, T1-H, reproduces well the larger scales of the resolved canopy simulation, TP1. This suggests that scales much larger than the canopy spacing still perceive the canopy as homogeneous. Using the mean-only drag recovers some of the smaller streamwise scales, but it does not act directly on the larger scales as the actual canopy does. As the element spacing is increased, the range of scales affected in a homogenised fashion is shifted to larger scales, so that the energetic turbulent scales become less damped. This is consistent with the results portrayed in figures 3.13(e–h), which show that, near the canopy tips, the dense canopy P0 damps the energy at $\lambda_x^* \sim 1000$–2000, compared to smooth walls, while the sparse canopy P2 leaves these scales relatively undisturbed.

3.3.1 Distributed mean-only drag simulation

The accumulation of energy in the lengthscales of the order of the canopy wavelengths and its harmonics observed in the canopy-resolving simulations requires a discrete representation of the canopy elements. Hence, it cannot be captured by either the mean-only- or the

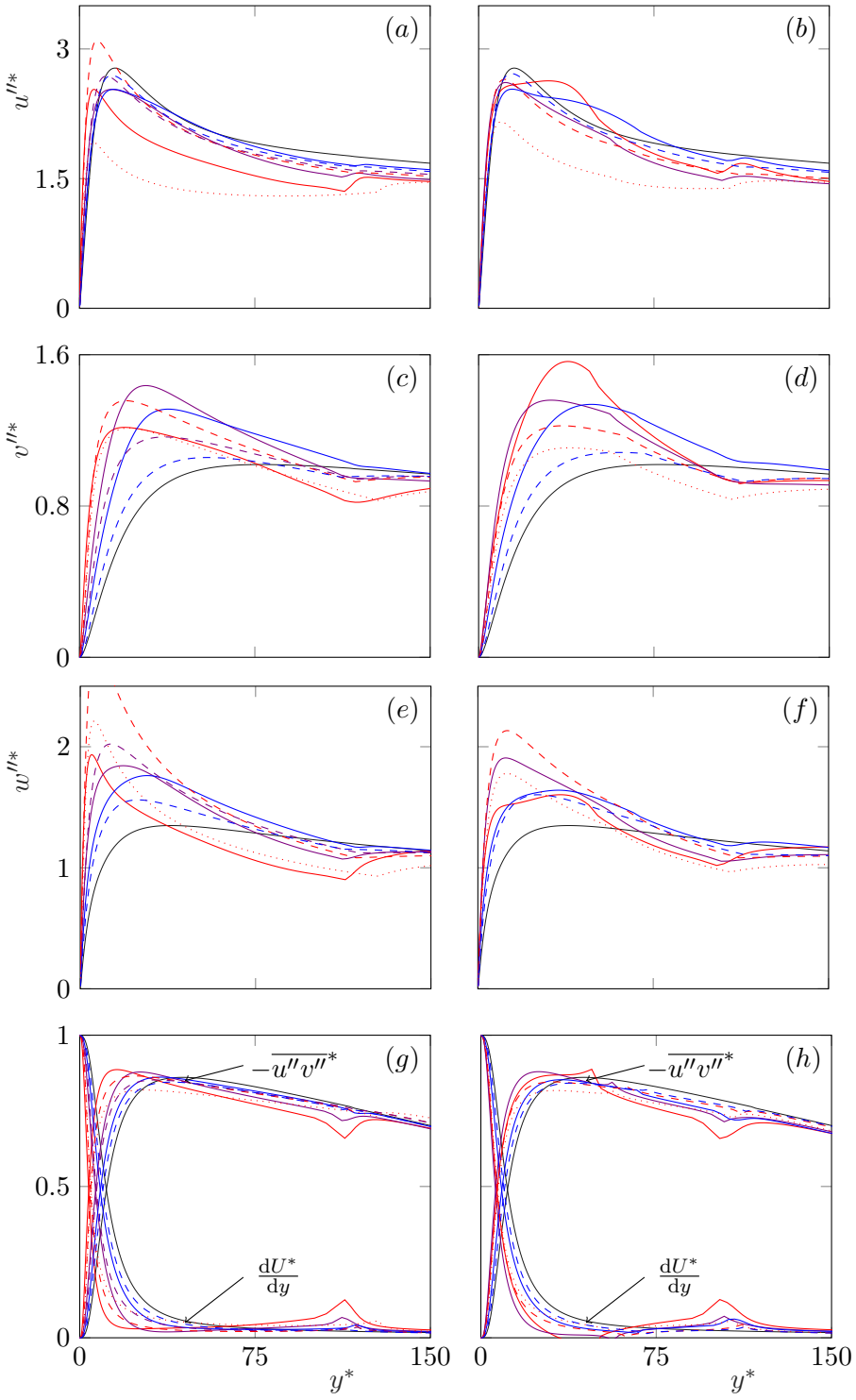

FIGURE 3.15 Rms velocity fluctuations and shear stresses for the background turbulence scaled with the local friction velocity, u^*, of the canopy-resolving, mean-only drag and homogeneous-drag simulations. In the first column, lines represent ——, case P0; - - -, case P0-H0; ·····, case P0-H; ——, case P1; - - -, case P1-H0; ——, case P2; and - - -, case P2-H0. In the second column, lines represent ——, case T1; - - -, case T1-H0; ·····, case T1-H; ——, case TP1; ——, case T2; and - - -, case T2-H0. The thin black lines represent case S.

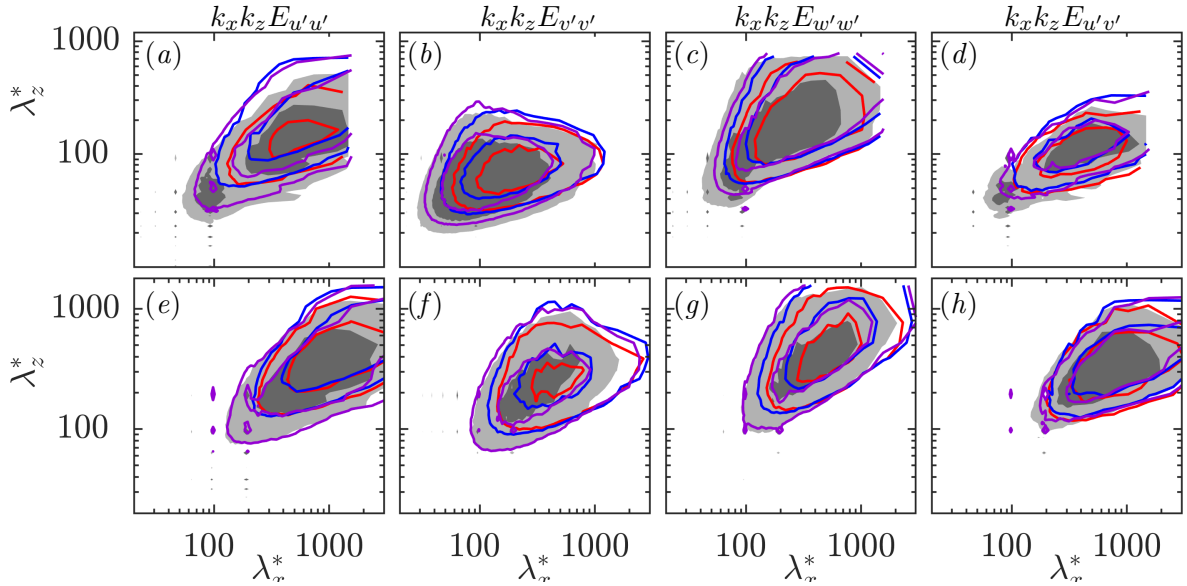

FIGURE 3.16 Pre-multiplied spectral energy densities of the full velocity fluctuations at (a–d) $y^* \approx 15$ and (e–h) $y^* \approx 105$, normalised by their respective u^*. Filled contours represent case TP1; ——, case T1-H0; ——, case T1-H; and ——, case TP1-L. The contours in (a–h) are in increments of 0.3, 0.075, 0.175, 0.075, 0.12, 0.06, 0.075 and 0.05, respectively.

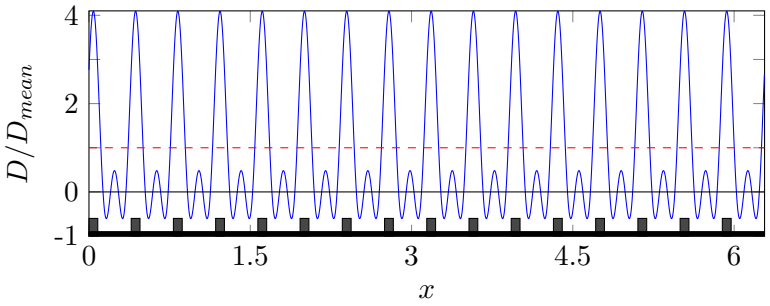

FIGURE 3.17 Drag force distribution in the streamwise direction in a plane passing through the canopy heads for case TP1-L (blue); - - -, distribution of the mean-only drag force, as in case T1-H0. The location of the canopy elements is sketched in grey at the bottom of the figure.

homogeneous-drag approaches. To introduce information of the canopy layout in the model, we distribute the drag calculated from the mean flow into a reduced-order representation of the canopy elements in case TP1-L. The representation consists of a truncation in Fourier space in x and z, of the actual layout. The procedure is illustrated in figure 3.17 by the streamwise distribution of the drag force used by this model. Note that like case TP1-H0, this model also applies a drag on the streamwise flow alone. In addition to capturing the local scaling of the flow, discussed in §3.3, this model is also able to represent the concentration of energy in the canopy scales for case TP1, as observed in figure 3.16. This is reflected by the collapse of the rms fluctuations of the full velocity components of TP1-L and TP1, as shown in figure 3.18. The magnitude of spanwise velocity fluctuations within the canopy of TP1-L is slightly larger than TP1, likely due to the fact that TP1-L does not apply any form of spanwise drag force. The drag force, although only applied in the streamwise direction, is also able to reproduce the canopy harmonics in the spectra of E_{vv} and E_{ww}, which are caused by the deflection of the streamwise flow around the canopy elements as a result of continuity. The large scales in the flow are similar to those in the mean-only drag, as the drag in this case also does not act on these scales directly. This method, however, is only able to capture the weak coherent flow generated by the permeable canopy, and still under-predicts the full streamwise velocity fluctuations of the impermeable canopy.

3.3.2 Fixed mean-velocity profile simulation

Although the distributed mean-only drag simulation described above, case TP1-L, can provide a reasonable approximation of the turbulent fluctuations for case TP1, it still does not capture the exact mean-flow profile, as illustrated in figure 3.19(a). The mean-flow profile, Reynolds shear stresses and the canopy drag all have an interdependent relationship. The sum of the stresses, $\tau = -\overline{u'v'} + \frac{1}{Re}\frac{\mathrm{d}U}{\mathrm{d}y} + \int_y^h D\ \mathrm{d}y$, is prescribed to be linear in a channel flow. The latter two terms are functions of the mean velocity profile, $U(y)$. Therefore, any deviation in the Reynolds shear stresses translates into a deviation in the mean velocity profile, and vice versa. As a conceptual experiment, we conduct a simulation, TP1-H0F, where $U(y)$ is fixed to that of case TP1, and obtain the mean-only drag required to sustain this profile *a posteriori*, similar to the simulations of Tuerke & Jiménez (2013). The aim of this simulation is to ascertain the additional mean-only drag that would be required to obtain the correct $U(y)$ of a resolved canopy simulation. The additional drag would make up for the deficit in the element-induced Reynolds shear stresses, which are not represented in the mean-only drag simulations. The resulting drag coefficient obtained is shown in figure 3.19(b), together with the drag coefficients for cases TP1, T1-H0 and T1-H. Within the canopy, the drag-coefficient required to make up for the deficit in the Reynolds shear stresses is roughly twice that of the resolved canopy. Furthermore, the force is also observed to be non-zero outside the canopy. The excess forcing just above the canopy is possibly due to the Reynolds stresses generated

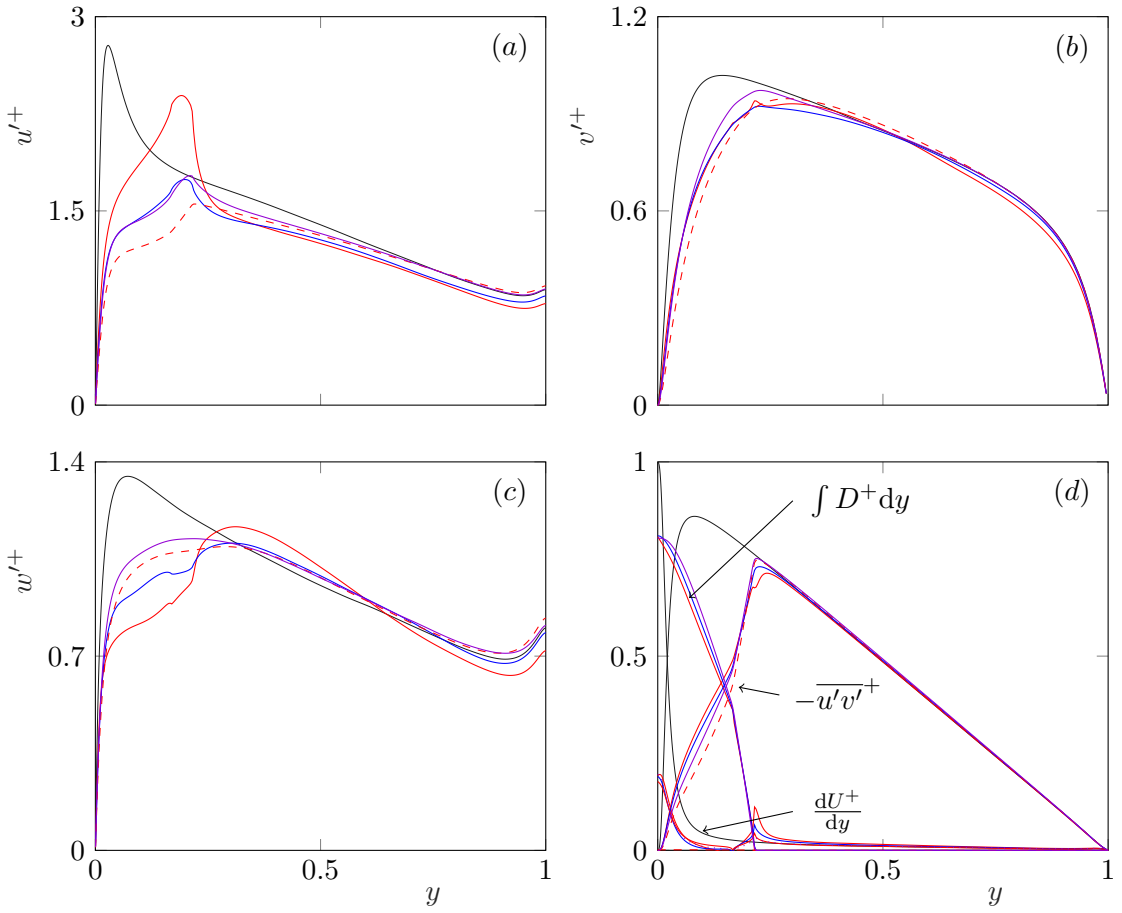

FIGURE 3.18 Rms fluctuations and shear stresses of the full flow, scaled with the global friction velocity u_τ. —, case TP1; —, case T1; - - -, case TP1-H0; —, case TP1-L. The thin black lines represent case S.

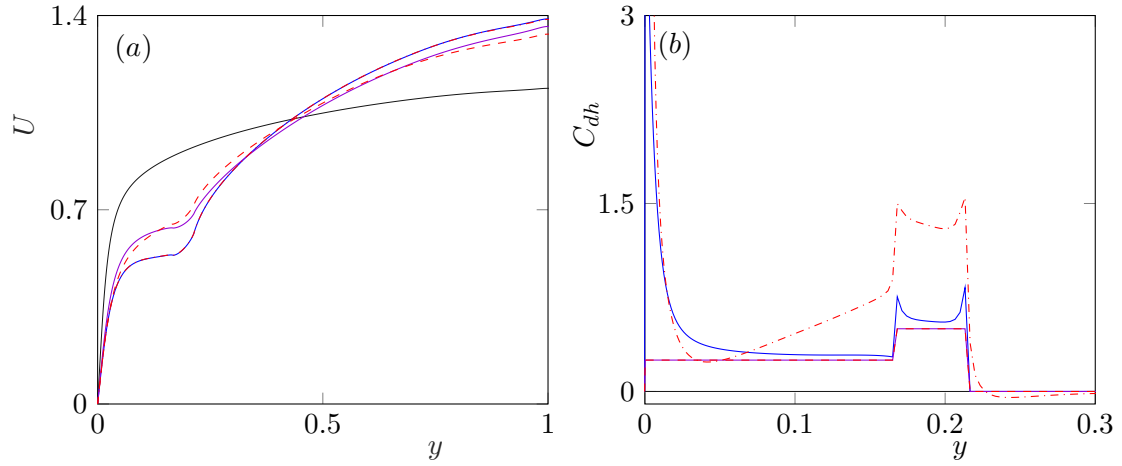

FIGURE 3.19 (a) Mean velocity profiles and (b) effective drag coefficients for —, case TP1; - - -, case TP1-H0; -·-·-, case TP1-H0F; —, case TP1-L. . The thin black lines represent case S.

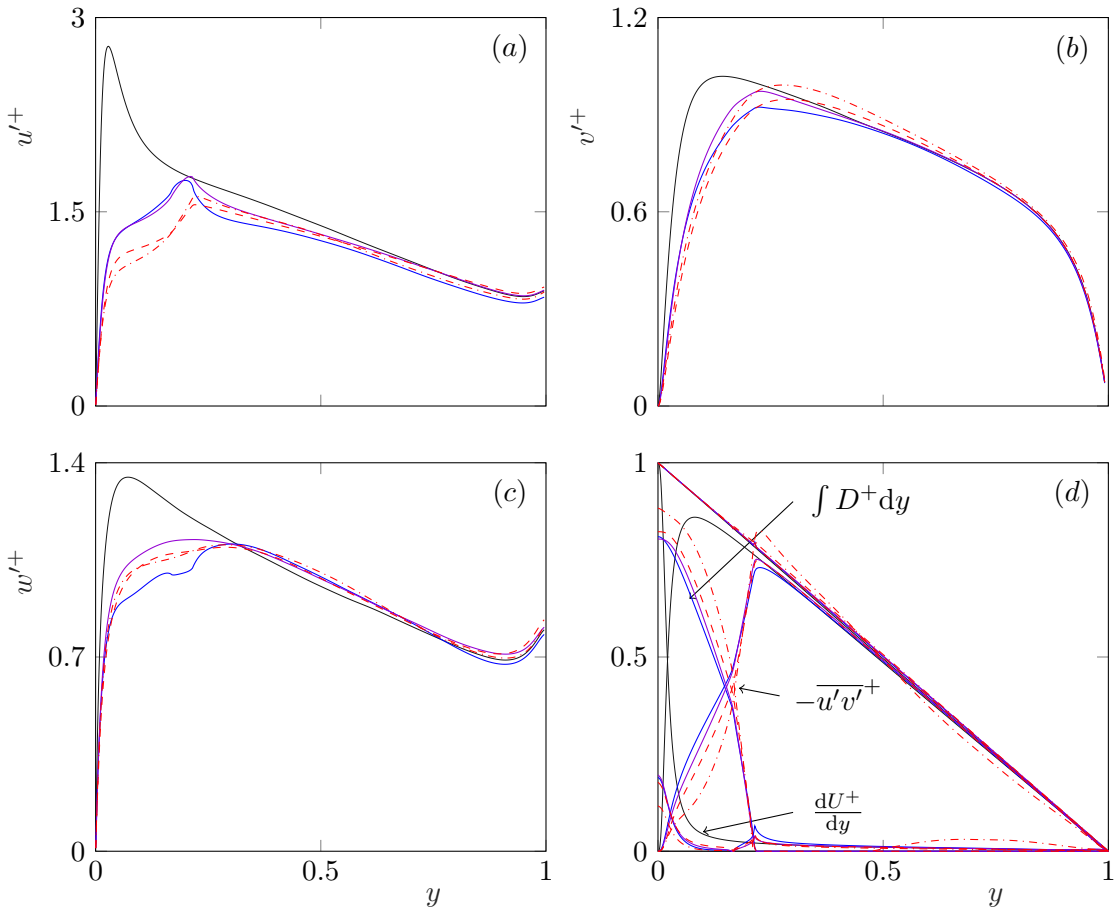

FIGURE 3.20 Rms fluctuations and shear stresses of the full flow, scaled with the global friction velocity u_τ. ——, case TP1; - - -, case TP1-H0; -·-·-, case TP1-H0F; ——, case TP1-L. The thin black lines represent case S.

by the canopy in the roughness sublayer. The rms velocity fluctuations obtained from this simulation, however, are similar to those from the mean-only-drag model in friction units, as can be observed in figure 3.20. The results, therefore, suggest that although the correct mean profile could theoretically be captured by tuning the drag coefficient, a representation of the element-induced flow would still be required to capture the velocity fluctuations.

Chapter 4

Turbulent flows over dense filament canopies

We now focus on canopies in the dense regime where we expect the flow near the top of the canopy to be dominated by the presence of the Kelvin–Helmholtz-like instability. The canopies we study consist of closely packed, rigid prismatic filaments with small element spacings, and large height-to-spacing ratios. The spacings range from $s^+ \approx 2.6$ to 48 for the densest and sparsest canopy geometries considered, respectively. The canopy heights range from $h^+ \approx 10$ to 128. The canopy geometries studied and the simulation parameters are presented in §4.1. The effect of the canopy parameters on the surrounding turbulent flow is discussed in §4.2. We find that the key parameter determining the effect of such canopies on the flow within and above them is the element spacing, and the height plays a secondary role. These canopies are also dense enough to elicit Kelvin–Helmholtz-like instabilities in the flow, which are discussed in §4.3.

4.1 Numerical simulations

We conduct direct numerical simulations of symmetric channels with rigid canopy elements on both walls. Here, unlike the previous chapter, the wall-normal origin, $y = 0$, is defined at the tip plane of the canopies protruding from the bottom wall. The canopy elements, therefore, extend below $y = 0$ and above $y = 2\delta$, and have a height h. A schematic representation of the channel is portrayed in figure 4.1. The size of the domain is a standard $2\pi\delta$ in the streamwise direction and $\pi\delta$ in the spanwise direction, with $\delta = 1$. The domain-to-canopy height ratio for most cases considered here is $(\delta + h)/h \approx 3$. We will show in §4.2 that the height of the roughness sublayer scales with the canopy spacing rather than their height, as in the configurations of Sadique *et al.* (2017) and MacDonald *et al.* (2018), and that outer-layer similarity is recovered well below the channel half-height. The channel height to

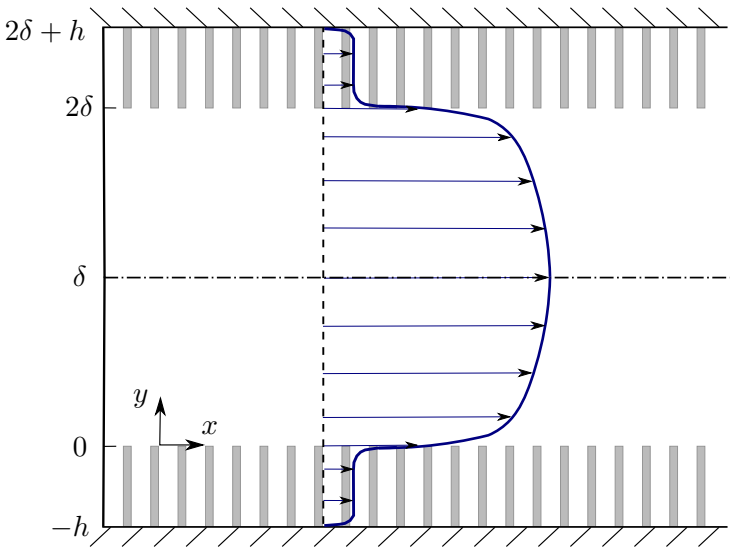

FIGURE 4.1 Schematic representation of the domain considered in the present study.

element spacing ratio for most canopies considered is $\delta/s \gtrsim 10$, and for the canopy with the largest element spacing is $\delta/s \approx 4$. The simulations are run at a constant flow rate, with the viscosity adjusted to obtain a friction Reynolds number $Re_\tau = u_\tau \delta/\nu \approx 185$, where u_τ is the friction velocity calculated at the canopy tips.

The parameters of the different simulations conducted are summarised in table 4.1. The simulation denoted by 'SC' is of a turbulent channel flow with smooth walls. The canopy-flow simulations are divided into three groups. The canopy elements studied in each group are prismatic, with a square top-view cross section, and their arrangement is illustrated in figure 4.2. The first group, denoted by the prefix 'S', consists of canopies with a fixed height, $h^+ \approx 96$, and element spacings ranging from $s^+ \approx 10$ to 48. The second group, marked by the prefix 'H', consists of canopies with a fixed element spacing, $s^+ \approx 16$, and element heights ranging from $h^+ \approx 16$ to 128. The element width-to-spacing ratio for the canopies of S and H is $w/s = 1/2$, which corresponds to a plan area ratio, $\lambda_p = 1/4$. The final group, denoted by the prefix 'G', consists of self-similar elements with a fixed height-to-spacing ratio $h/s \approx 4$, and $w/s = 2/9$ that corresponds to a plan area ratio, $\lambda_p \approx 1/20$. The heights for the canopies of G range from $h^+ \approx 10$ to 100, with the element spacings varying in proportion to their height. Two additional simulations, $\mathrm{H32}_{180}$ and $\mathrm{H32}_{400}$, are conducted to check the dependence of the results on the friction Reynolds number. The canopy geometries for both these simulations have $s^+ \approx 16$, $h^+ \approx 32$ and $w/s = 1/2$, with friction Reynolds numbers $Re_\tau \approx 180$ and 400. Note that all the canopies studied in the chapter have roughness frontal densities $\lambda_f > 0.1$, thereby placing them in the dense regime as demarcated by Nepf (2012).

	Case	$N_x \times N_z$	$n_x \times n_z$	u_τ	Re_τ	λ_f	h^+	s^+	w/s
Smooth	SC	–	–	0.064	186.3	–	–	–	–
Fixed height ($h^+ \approx 100$)	S10	108×54	12×12	0.071	176.7	4.6	95.5	10.3	$\frac{1}{2}$
	S16(H96)	72×36	24×24	0.088	187.7	3.1	101.8	16.4	
	S24	48×24	24×24	0.102	187.4	2.0	101.2	24.5	
	S32	36×18	24×24	0.112	186.4	1.5	100.7	32.5	
	S48	24×12	24×24	0.124	180.1	1.0	97.0	47.2	
Fixed spacing ($s^+ \approx 16$)	H16	72×36	24×24	0.071	184.7	0.5	17.2	16.1	$\frac{1}{2}$
	H32	72×36	24×24	0.080	188.8	1.0	34.6	16.5	
	H64	72×36	24×24	0.086	186.2	2.0	68.1	16.2	
	H96(S16)	72×36	24×24	0.088	185.7	3.1	101.8	16.4	
	H128	72×36	24×24	0.086	184.8	4.1	133.2	16.4	
Self-similar geometry ($h/s \approx 4$)	G10	432×216	9×9	0.064	175.9	0.85	10.1	2.6	$\frac{2}{9}$
	G20	216×108	9×9	0.072	190.7		22.2	5.6	
	G40	108×54	18×18	0.106	188.2		43.4	11.0	
	G60	72×36	18×18	0.127	183.3		64.7	16.0	
	G100	48×24	18×18	0.147	185.7		97.9	24.3	
Different Re_τ	$H32_{180}$	72×36	12×12	0.075	184.6	1.0	33.9	16.1	$\frac{1}{2}$
	$H32_{400}$	162×81	12×12	0.066	399.9		32.0	15.5	

Table 4.1 Simulation parameters. N_x and N_z are the number of rows of canopy elements in the streamwise and spanwise directions, respectively. The number of points used to resolve each period of the canopy in the streamwise and spanwise directions are n_x and n_z, respectively. u_τ is the friction velocity based on the shear at the canopy tips scaled with the channel bulk velocity. Re_τ is the friction Reynolds number based on u_τ and δ. The canopy roughness frontal density, height, width and spacing are λ_f, h, w and s, respectively.

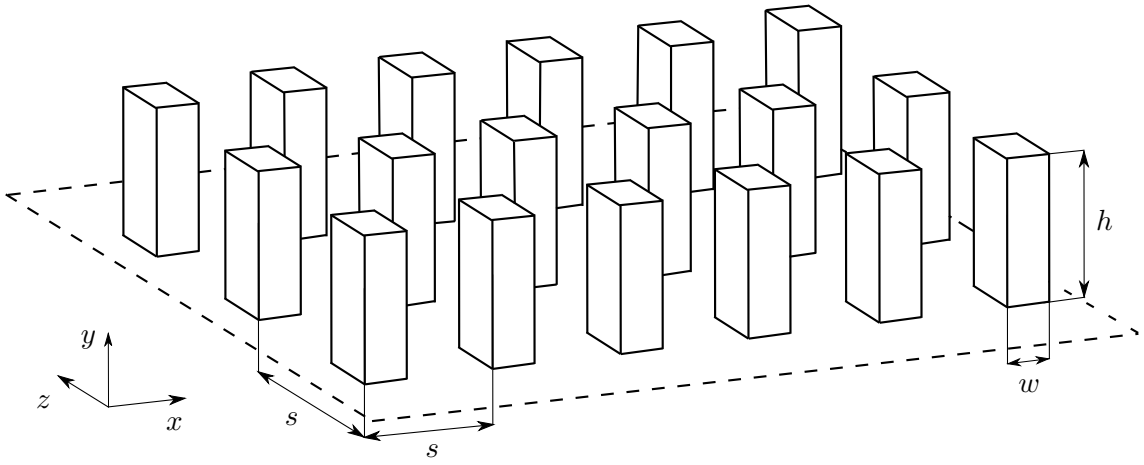

FIGURE 4.2 Schematic of the canopy layouts considered in the present study. The canopies are characterised by their element height, h, the element width, w, and the element spacing, s. Note that the element have a square top-view cross section.

4.1.1 Reynolds number effect

To analyse the influence of the Reynolds number in our subsequent DNSs, we compare the results of cases $\mathrm{H32}_{180}$ and $\mathrm{H32}_{400}$, which have the same canopy height and spacings in friction units, but different friction Reynolds numbers. The velocity fluctuations and the Reynolds shear stresses within the canopy, and above it up to a height of $y^+ \approx 10$, of these simulations essentially collapse, as shown in figure 4.3. This suggests that the flow in the region near the canopy-tip plane scales in friction units, similar to the near-wall region in smooth-wall flows (Moser *et al.*, 1999). Scaling in friction units over conventional rough surfaces has also been noted by Chan *et al.* (2015). Beyond $y^+ \gtrsim 10$, we observe that the magnitude of the peaks in the fluctuations and the Reynolds shear stresses are larger for case $\mathrm{H32}_{400}$ compared to case $\mathrm{H32}_{180}$. The increase in magnitude of the near-wall peaks in the velocity fluctuations at friction Reynolds numbers larger than $Re_\tau \approx 180$ is consistent with that observed in smooth-wall flows (Moser *et al.*, 1999; Sillero *et al.*, 2013), also included in figure 4.3 for reference. Further away from the canopy tips, at $y^+ > 50$, the rms velocity fluctuations from the canopy simulations coincide with those from the smooth-wall simulations at their corresponding Reynolds numbers, which indicates the recovery of outer-layer similarity. In addition to the rms fluctuations being similar for these simulations, the distribution of energy in different scales is also similar. This is illustrated by the pre-multiplied spectral energy densities at $y^+ \approx 15$, portrayed in figure 4.4. This height roughly corresponds to the location where the magnitude of the fluctuations peaks in smooth-wall flows (Jiménez & Pinelli, 1999). The results of $\mathrm{H32}_{180}$ and $\mathrm{H32}_{400}$ suggest that the effect of the canopy scales in friction units, and therefore the results presented in the following sections for flows at $Re_\tau \approx 180$ should also be relevant for higher Reynolds number flows.

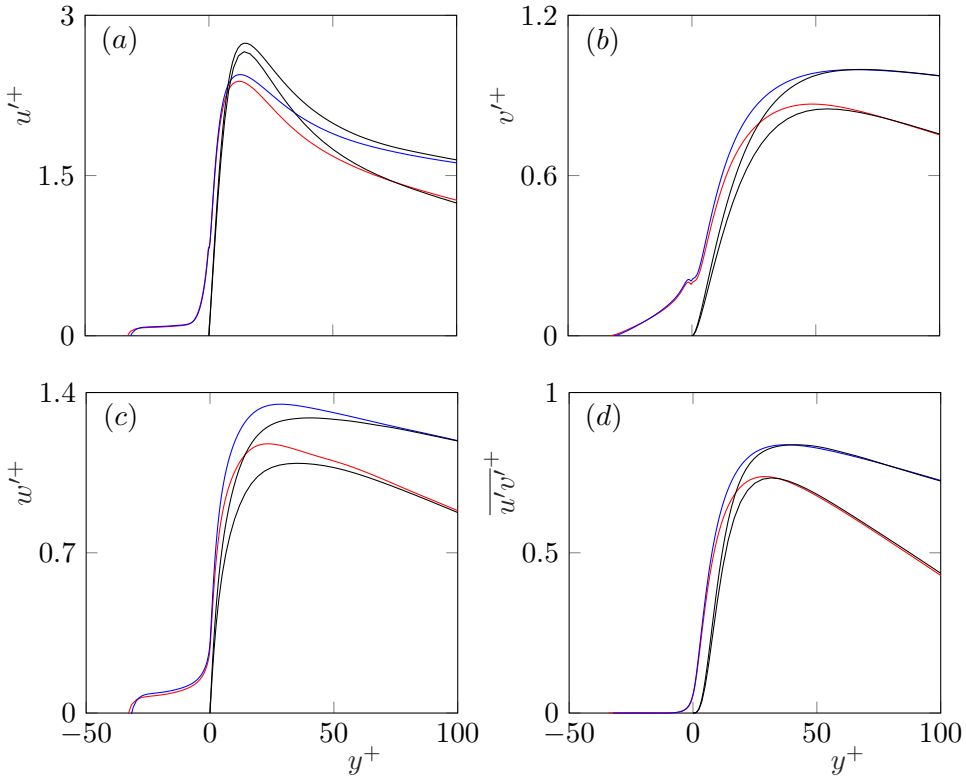

FIGURE 4.3 Rms velocity fluctuations and Reynolds shear stresses for cases $\mathrm{H32}_{180}$ in red and $\mathrm{H32}_{400}$ in blue. The black lines represent the corresponding smooth-wall cases. The data for the smooth-wall simulations at $Re_\tau \approx 400$ is taken from Moser *et al.* (1999).

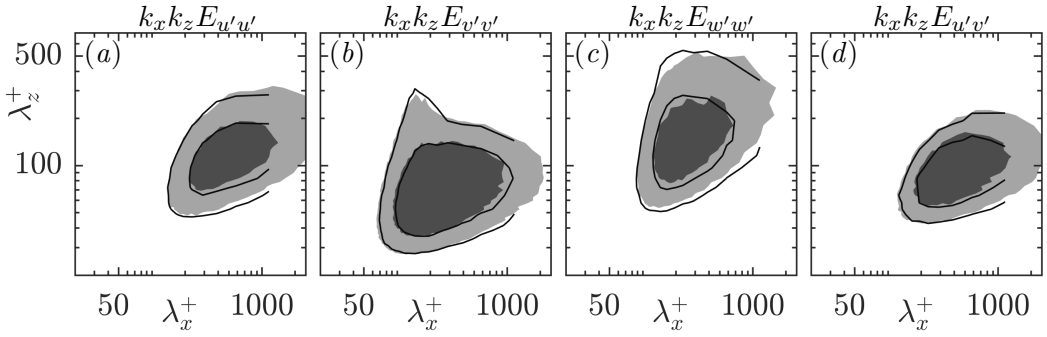

FIGURE 4.4 Pre-multiplied spectral energy densities for cases $\mathrm{H32}_{180}$ (line contours) and $\mathrm{H32}_{400}$ (shaded contours), normalised by the respective rms values, at a height $y^+ \approx 15$. Contours from (*a–d*) are in increments of 0.075, 0.06, 0.07 and 0.1, respectively.

4.2 Effect of canopy parameters on the surrounding turbulence

In this section, we discuss the effect of changing the height and spacing of the canopy elements on the velocity fluctuations within and above the canopies. Over conventional rough surfaces, with heights comparable to or smaller than their spacings, the height of the roughness sublayer is generally observed to be a function of the roughness height (Raupach *et al.*, 1991; Flack *et al.*, 2007; Abderrahaman-Elena *et al.*, 2019). Jiménez (2004) reviewed the effect of various roughness geometries on turbulent flows and noted that in flows over closely packed spanwise aligned grooves, the flow within each groove would be isolated from the overlying flow due to the 'sheltering' effect of the preceding obstacle. The overlying flow, in this case, would not interact with the full height of the groove. This sheltering effect was also noted by Sadique *et al.* (2017) for high-aspect-ratio prismatic roughness, and by MacDonald *et al.* (2018) for spanwise aligned grooves with large spacings. As the element spacings of the canopies studied here are small, this sheltering effect should result in the overlying flow only interacting with the region near the canopy-tip plane. In order to determine the height of this region, we examine the flow element-coherent flow induced by the canopy elements. The footprint of the element-induced flow can be observed in the instantaneous realisations of the velocity above the canopy-tip plane, portrayed for the canopies of families H and G in figure 4.5. As in the previous chapter, we isolate the element-induced flow using the standard triple decomposition of Reynolds & Hussain (1972)

$$\boldsymbol{u}(\boldsymbol{x},\boldsymbol{y},\boldsymbol{z},\boldsymbol{t}) = \boldsymbol{U}(\boldsymbol{y}) + \boldsymbol{u'}(\boldsymbol{x},\boldsymbol{y},\boldsymbol{z},\boldsymbol{t}), \tag{4.1}$$

$$\boldsymbol{u'}(\boldsymbol{x},\boldsymbol{y},\boldsymbol{z},\boldsymbol{t}) = \widetilde{\boldsymbol{u}}(\boldsymbol{x},\boldsymbol{y},\boldsymbol{z}) + \boldsymbol{u''}(\boldsymbol{x},\boldsymbol{y},\boldsymbol{z},\boldsymbol{t}), \tag{4.2}$$

where $\boldsymbol{u}$ is the full velocity, $\boldsymbol{U}$ is the mean velocity, and $\boldsymbol{u'}$ is the full space-and-time fluctuating velocity, decomposed into the element-induced, dispersive velocity, $\widetilde{\boldsymbol{u}}$, and the incoherent, background-turbulence fluctuating velocity $\boldsymbol{u''}$.

We observe that the element-induced velocity fluctuations, for all the canopies studied here, decay exponentially above the canopy-tip plane, and become negligible at a height of one element spacing above regardless of the canopy depth, as shown in figure 4.6. This suggests that the element spacing is the relevant lengthscale for the overlying flow. The element-induced fluctuations decay below the canopy-tip plane as well. The element-induced fluctuations within become zero well above the canopy base for the canopies G10 and S10, that is, the canopies with the smallest element spacings. For the other canopies, the fluctuations only become zero at the wall at the canopy base. The intensity of the velocity fluctuations within the canopy also depends on the element spacing. For the canopies of family H, which have a constant element spacing, the change in element height does not have a noticeable effect on the element-induced fluctuations, as shown in figures 4.6(b, e, h). For the canopies of

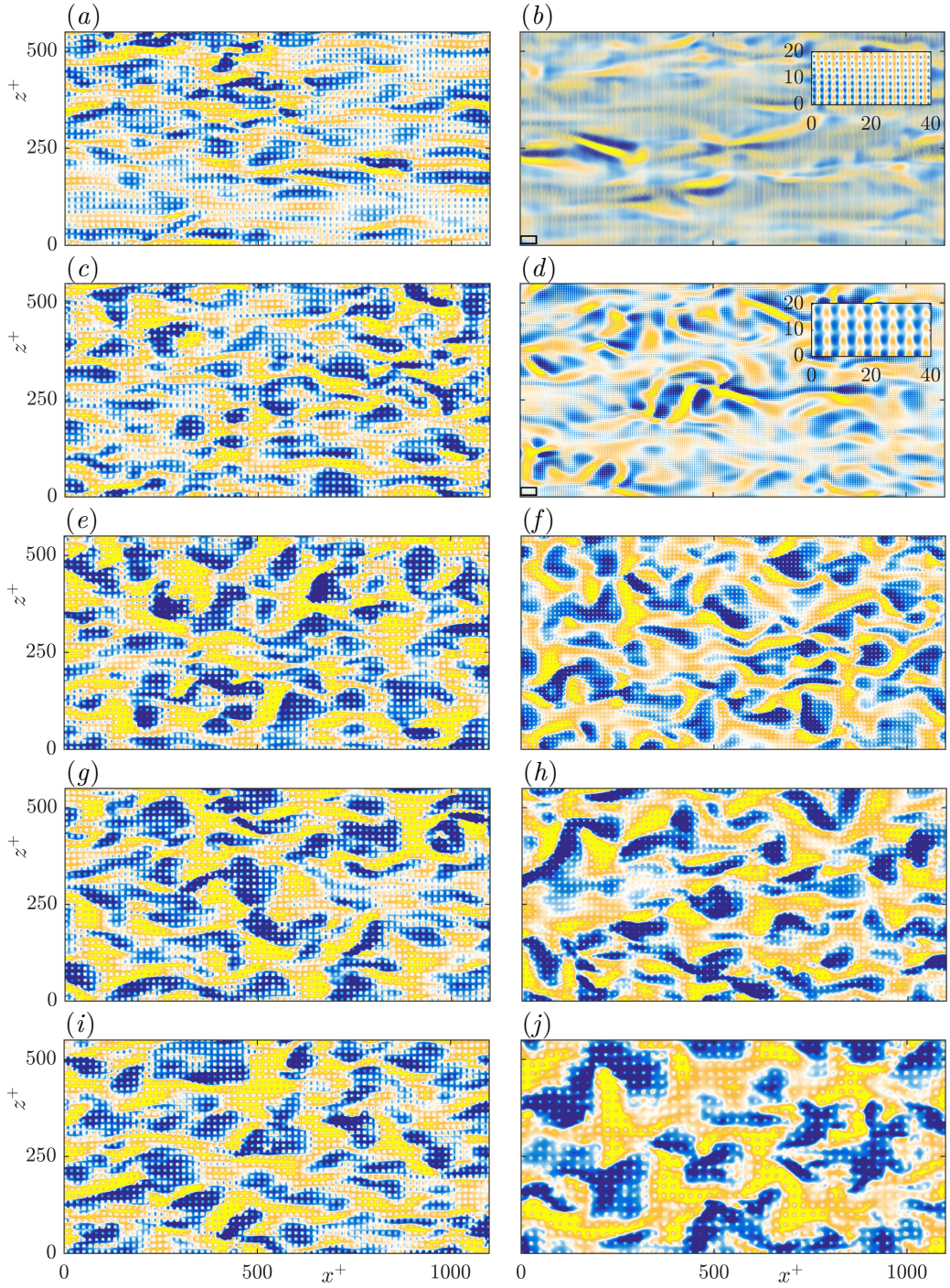

FIGURE 4.5 Instantaneous realisations of the wall normal velocity at $y \approx 0.1s$, normalised by u_τ. From top to bottom, the left column represents cases H16 to H128; and right column, cases G10 to G100. The insets in (b, d) provide a magnified view of the region in the bottom left corner of these panels, marked with a black rectangle. The clearest and darkest colours indicate intensities of ± 0.4 in the left column and, from top to bottom, $\pm(0.2, 0.4, 0.8, 0.8, 1.0)$ in the right column.

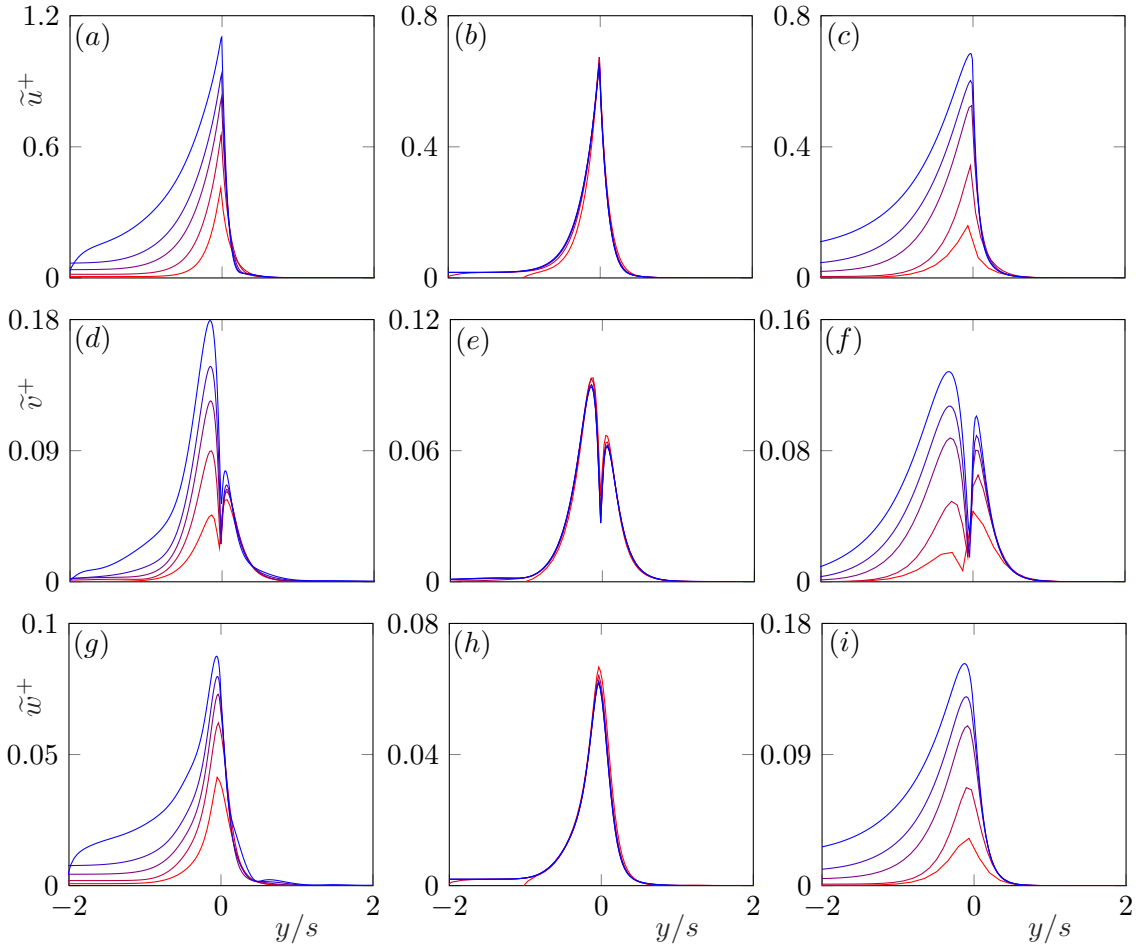

FIGURE 4.6 Root-mean-square velocity fluctuations of the element-induced flow. The lines from red to blue represent (a,d,g) cases S10 to S48; (b,e,h) cases H16 to H128; and (c,f,i) cases G10 to G100.

families S and G, the intensity of the velocity fluctuations within the canopy increases with element spacing, when scaled using either the friction velocity or the channel bulk velocity. This suggests that the intensity of the element-induced flow within the canopy also depends essentially on the canopy spacing.

Even though the element-induced fluctuations only extend to one element spacing above the canopy-tip plane, their influence on the background-turbulence extends to a height of approximately 2–3 element spacings. Abderrahaman-Elena *et al.* (2019) observed a similar effect over conventional cubical roughness, where the element-induced fluctuations only extended to $y \approx h$, but the effect of the roughness on the overlying flow extended to $y \approx 3h$ above them. At heights of $y/s >$ 2–3 above the canopy-tip plane, the full rms velocity fluctuations collapse with those of smooth-wall turbulence, as shown in figure 4.7, which is indicative of the recovery of outer-layer similarity. This is verified by a comparison of the pre-multiplied spectral energy densities of the canopy and smooth-wall cases in figure 4.8,

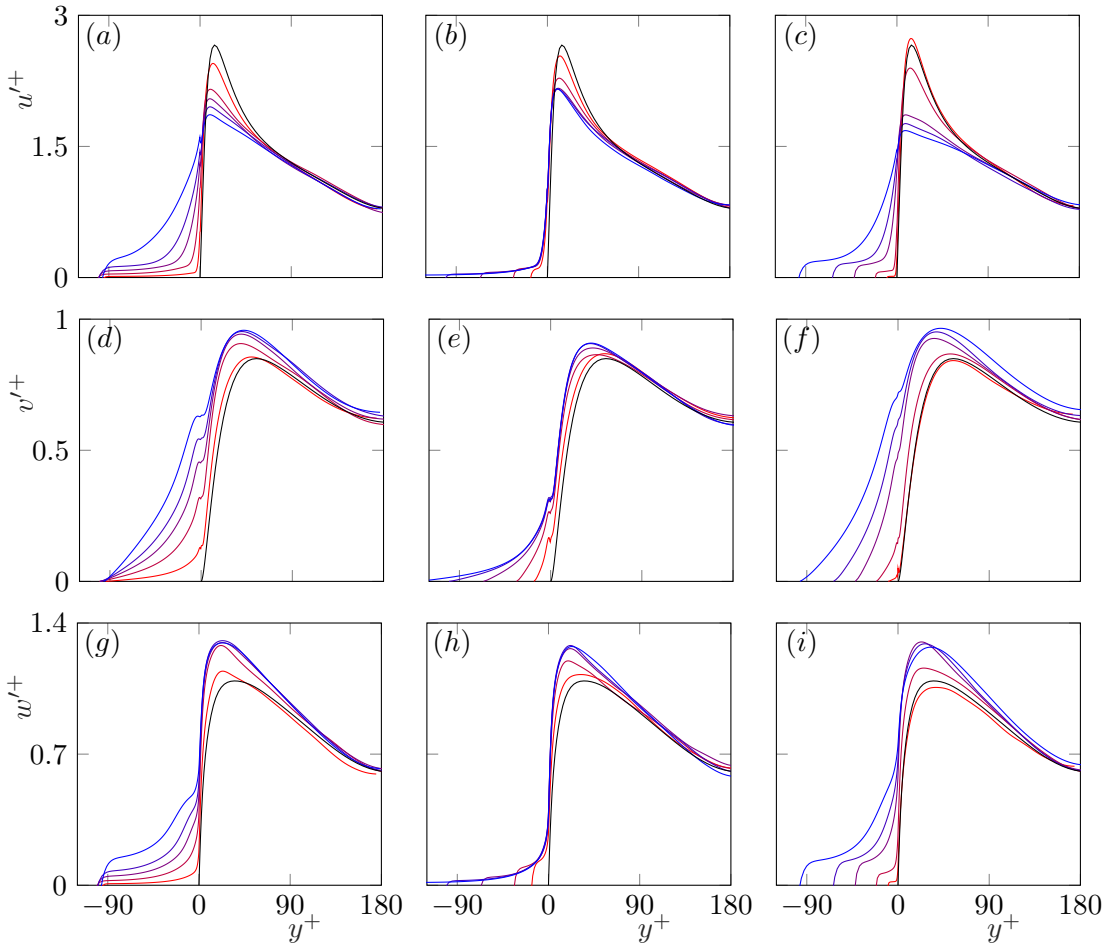

FIGURE 4.7 Rms velocity fluctuations within and above the canopies. The lines from red to blue represent (a,d,g) cases S10 to S48; (b,e,h) cases H16 to H128; and (c,f,i) cases G10 to G100. The black lines represent case SC.

which shows that the energy densities of the canopies of family S collapse with those of the smooth-wall case for $y^+ \gtrsim 90$. This corresponds to a height of about $2s$ for case S48, the canopy with the largest spacing. Although not shown here, the pre-multiplied spectral energy densities of the canopies of families H and G collapse with the smooth-wall spectra for $y/s \gtrsim 3$ as well.

In canopies with very small element spacing, the height of the roughness sublayer is small, and we would expect such canopies not to disrupt the overlying turbulence significantly, regardless of their depth. As discussed in §1.1, in the literature on conventional roughness, small roughness elements that have a negligible effect on the overlying turbulent flow are termed 'hydraulically smooth', as the flow over them remains essentially smooth-wall like (Nikuradse, 1933; Raupach *et al.*, 1991). Typically, roughness elements with a characteristic size of a few wall-units, $h^+ \lesssim 5$, fall into the hydraulically-smooth category (Raupach *et al.*, 1991; Jiménez, 2004; Flack *et al.*, 2007). Of the canopies studied here, we observe that the

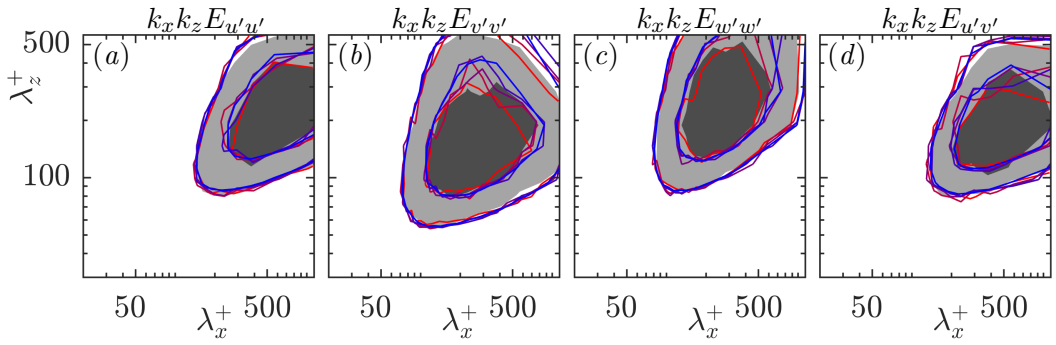

FIGURE 4.8 Pre-multiplied spectral energy densities at $y^+ \approx 90$, with line contours from red to blue representing cases S10 to S48, normalised by their respective u_τ. The filled contours represent the smooth-wall case, SC. The contours in (a–d) are in increments of 0.11, 0.04, 0.06 and 0.04, respectively.

flow over the canopy of case G10, which has an element spacing of $s^+ \approx 2.6$, is essentially smooth-wall-like. This is evidenced by the collapse of the rms velocity fluctuations, Reynolds shear stresses, and the mean velocity profile of this case with those of the smooth-wall case, as shown in figures 4.7(c, f, i) and 4.9(c, f). In addition, the magnitude of the velocity fluctuations below the canopy-tip plane is negligible. This suggests that the overlying turbulent flow essentially perceives the canopy-tip plane as an impermeable wall, and has little or no interaction with the canopy region below this plane.

For canopies with larger element spacings, we begin to observe deviations from smooth-wall-like behaviour. Above the canopy-tip plane, an increase in the element spacing causes a reduction in the intensity of the streamwise velocity fluctuations, and an increase in the intensity of the wall-normal and spanwise velocity fluctuations, as can be observed in figure 4.7 for the canopies of families S and G. For canopies with large element spacings, such as those of S48 and G100, the peak in u', typical of smooth-wall flows, is severely reduced. We also observe an increase in the Reynolds shear stresses above the canopy-tip plane with increasing element spacing, shown in figures 4.9(d, f), with an associated increase in the drag. The drag increase due to rough surfaces is generally expressed in terms of the downward shift in the logarithmic region of the mean-velocity profile compared to that for a smooth wall (Hama, 1954). This shift can be observed for the canopies of families S and G in figures 4.9(a, c). The change in the drag observed for some of the dense canopies studied here was reported in Gómez-de-Segura *et al.* (2018*b*). The decrease in u' and increase in v', w' and drag with increasing element size is commonly reported over conventional rough surfaces (Ligrani & Moffat, 1986; Orlandi & Leonardi, 2006; Abderrahaman-Elena *et al.*, 2019). Several authors have attributed the changes in the velocity fluctuations to the roughness elements modifying the near-wall turbulence cycle (Jiménez, 2004; Flores & Jiménez, 2006; Flack *et al.*, 2007; Abderrahaman-Elena *et al.*, 2019). The associated structures, such as streaks and quasi-

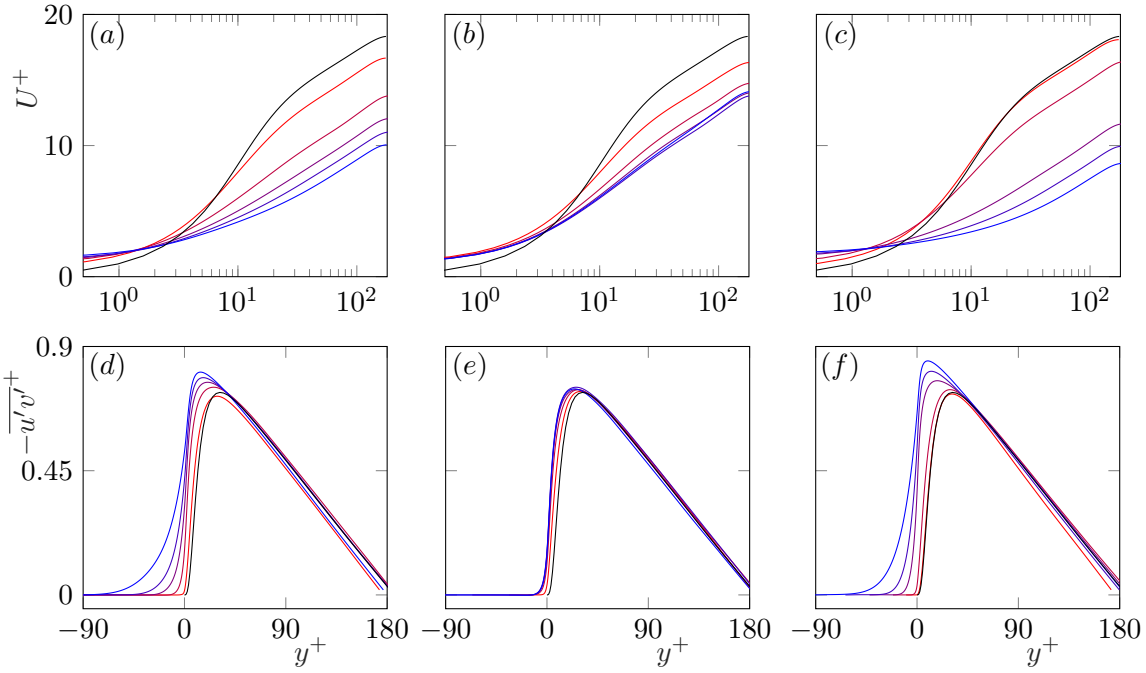

FIGURE 4.9 Profiles of the (*a*–*c*) streamwise mean velocity and (*d*–*f*) Reynolds shear stresses. The lines from red to blue represent (*a*,*d*) cases S10 to S48; (*b*,*e*) cases H16 to H128; and (*c*,*f*) cases G10 to G100. The black lines represent case SC.

streamwise vortices, are predominantly streamwise coherent (Kline *et al.*, 1967; Jiménez & Pinelli, 1999). A breakdown of the streamwise coherent structures in the flow with increasing canopy element spacing can also be observed in the present simulations. This is illustrated in the instantaneous realisations of the wall-normal velocity for the canopies of family G, portrayed in figure 4.5. Below the canopy-tip plane, increasing the element spacing results in an increase in all the components of the velocity fluctuations. The wall-parallel fluctuations, u' and w', drop rapidly below the canopy-tip plane, and their magnitude reaches a plateau in the middle of the canopy before they drop again near the canopy base to meet the no-slip condition. The height over which the fluctuations decay within the canopy and the magnitude of the fluctuations in the middle of the canopy appear to correlate with the element spacing. Note that this plateau in u' and w' within the canopy is asymptotic and requires a sufficiently large canopy depth to occur. Thus, this plateau is essentially absent for the canopy of S48, because of its low canopy height-to-spacing ratio, $h/s \approx 2$. The wall-normal fluctuations within the canopy do not exhibit this plateau and decay gradually below the canopy tip plane to meet the impermeability condition at the canopy base. Let us also note here that the element-induced fluctuations account for less than 10% of the magnitude of the total cross-velocity fluctuations within the canopy. This is consistent with the observations of previous dense canopy studies (Poggi & Katul, 2008).

As noted previously, the differences between the element-induced fluctuations for the fixed-spacing canopies of family H are negligible. However, we do observe changes in the full rms velocity fluctuations for these cases. Above the canopy tips, we observe a decrease in u' and an increase in v' and w' with an increase in the canopy height, similar to the effect of increasing the element spacing, as shown in figures 4.7(b, e, h). Within the canopy, u' and w' for all cases collapse to a single curve, only departing from it to meet the no-slip condition at the canopy base. The magnitude of the wall-normal fluctuations within the canopy, however, increases with the canopy height up to $h/s \approx 6$. For $h/s \gtrsim 6$, the effect of the canopy height on the flow, within and above the canopy, saturates. This is illustrated in figures 4.7(b, e, h) and 4.9(b, e), which show that the velocity fluctuations, Reynolds shear stresses and the mean velocity profiles of cases H96 and H128 with $h/s \approx 6$ and 8, respectively, are essentially the same.

4.3 Kelvin–Helmholtz-like instabilities over dense canopies

The variations observed in the velocity fluctuations for the fixed-element-spacing simulations may, in part, result from the growth of a Kelvin–Helmholtz-like instability, typically reported in dense canopy flows (Finnigan, 2000; Nepf, 2012). In order to assess the presence of this instability in the flow, we compare the pre-multiplied spectral energy densities of the wall-normal velocity at $y^+ \approx 15$ in figures 4.10$(f$–$j)$. For case H16, we observe that the spectral energy densities of the fluctuations above the canopy are similar to those above smooth walls. As the height of the canopy is increased, we observe a progressive increase in the energy in long spanwise wavelengths, $\lambda_z^+ > 100$, for a narrow range of streamwise wavelengths, $\lambda_x^+ \in (150$–$250)$. This range of streamwise wavelengths remains roughly constant for increasing canopy heights. Such a footprint in the spectral energy densities has been previously associated with the presence of spanwise-coherent, Kelvin–Helmholtz-like instabilities over riblets (García-Mayoral & Jiménez, 2011), transitional roughness (Abderrahaman-Elena *et al.*, 2019) and permeable substrates (Gómez-de-Segura & García-Mayoral, 2019). This instability is known to generate strong wall-normal fluctuations and, hence, its signature is most clear in the spectra of the wall-normal velocity fluctuations (García-Mayoral & Jiménez, 2011; Gómez-de-Segura & García-Mayoral, 2019). Above a short canopy, like that of H16, the impermeability condition at the base of the canopy would inhibit the instability by blocking the wall-normal fluctuations (Huerre, 1983; Healey, 2009). Increasing the canopy height weakens this effect, leading to a stronger footprint of the instability, as observed in figures 4.10$(f$–$j)$. The Kelvin–Helmholtz-like instability has also been reported to cause an increase in the Reynolds shear stresses, with an associated increase in the friction drag, over surfaces such as riblets and permeable substrates (García-Mayoral & Jiménez, 2011; Gómez-de-Segura & García-Mayoral, 2019). The increase, and the eventual asymptoting, of the Reynolds shear stresses with increasing canopy heights over the canopies of family H can be observed in figure 4.9(e).

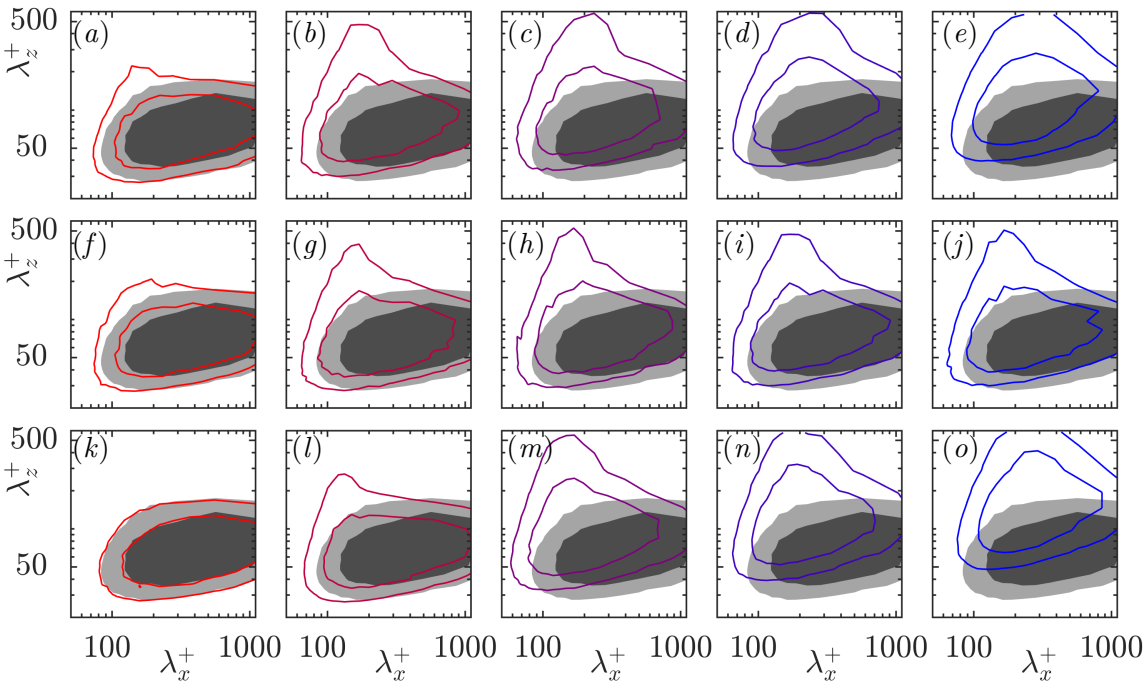

FIGURE 4.10 Pre-multiplied spectral energy densities of the full wall-normal velocity, $k_x k_z E_{v'v'}$, at height $y^+ \approx 15$ normalised by their respective rms values. The line contours represent (*a*–*e*) cases S10 to S48; (*f*–*j*) cases H16 to H128; and (*k*–*o*) cases G10 to G100. The shaded contours represent case the smooth-wall case, SC. The contours are in increments of 0.06 for all the cases.

The shift in the mean-velocity profile for these canopies, which reflects the increase in drag, can be observed in figure 4.9(*b*). The above discussion suggests that the growth of the Kelvin–Helmholtz-like instability is, in large part, responsible for the changes observed in the velocity fluctuations, Reynolds shear stresses and friction drag for the fixed-spacing canopies of family H and that the effect of the element-induced flow is secondary.

The growth of the Kelvin–Helmholtz-like instability near the canopy-tip plane with increasing canopy height also contributes to the increase in the wall-normal velocity fluctuations within the canopy observed in figure 4.7(*e*). This is demonstrated by the wall-normal spectral energy densities of the flow within the canopies, portrayed at $y^+ \approx -10$ for all the canopies of family H, in figures 4.11(*a*–*e*). Note that in calculating the spectra for a region with solid obstacles, we have implicitly assumed that the obstacles are fluid regions with zero flow velocity. As discussed in the previous paragraph, for case H16 the instability is inhibited by the proximity of the canopy-base wall, and the flow above shows similarities to a smooth-wall flow. The energy density within the canopy at $y^+ \approx -10$ for this case also shows some overlapping regions with the smooth-wall spectra, with additional energy in the wavelengths

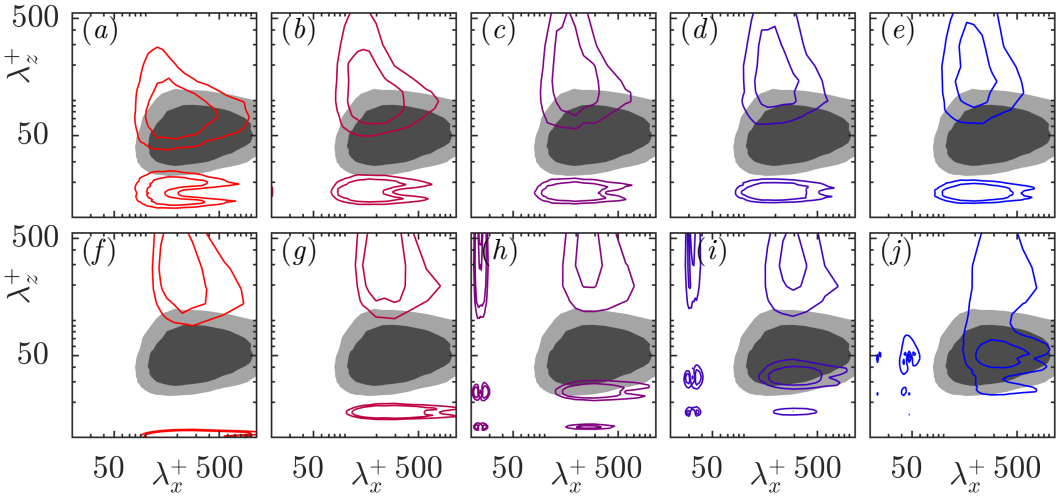

FIGURE 4.11 Pre-multiplied spectral energy densities of the full wall-normal velocity, $k_x k_z E_{v'v'}$, for (a–e) cases H16 to H128 at a height of $y^+ \approx -10$; and (f–j) cases S10 to S48 at a height of $y^+ \approx -40$. The contours are normalised by the rms values of their respective cases. The shaded contours are of case SC at a height of $y^+ \approx 1$, for reference. The contours are in increments of 0.075 for all the cases.

associated with the Kelvin–Helmholtz-like instability. The smooth-wall spectra displayed for reference correspond to $y^+ \approx 1$, which is as low as possible while yielding a non-negligible energy, since no direct comparison with $y^+ \approx -10$ is possible. We also observe some energy in the spanwise wavelength corresponding to the canopy spacing and a broad range of streamwise wavelengths. These regions can be attributed to the modulation of the element-induced flow by the larger scale fluctuations induced by the instability or the overlying turbulence (Abderrahaman-Elena *et al.*, 2019). This suggests that the fluctuations within a short canopy result mainly from the penetration of the overlying turbulence, with additional contributions from the Kelvin–Helmholtz-like instability and the element-induced flow. As the canopy height is increased, and the instability becomes stronger, the deviations in the spectral energy densities from smooth-wall flow become larger. The fluctuations within the canopy in cases H32 to H128 arise mainly from large spanwise wavelengths, likely originating from the Kelvin–Helmholtz-like instability near the canopy-tip plane, along with a contribution of the modulated element-induced flow discussed above. The increasing signature of the instability within the canopy with increasing element height can also be observed in the instantaneous realisations of the wall-normal velocity at $y^+ \approx -10$, portrayed in figure 4.12. The presence of large spanwise wavelengths deep within the canopy can also be noted for the canopies of family S, whose spectral energy densities and realisations of wall-normal velocity at $y^+ \approx -40$ are portrayed in figures 4.11(f–j) and 4.12, respectively. It is also worth noting that even in canopies with small element spacings, such as that of case S10, the wall-parallel velocity fluctuations decay rapidly below the canopy-tip plane, but the

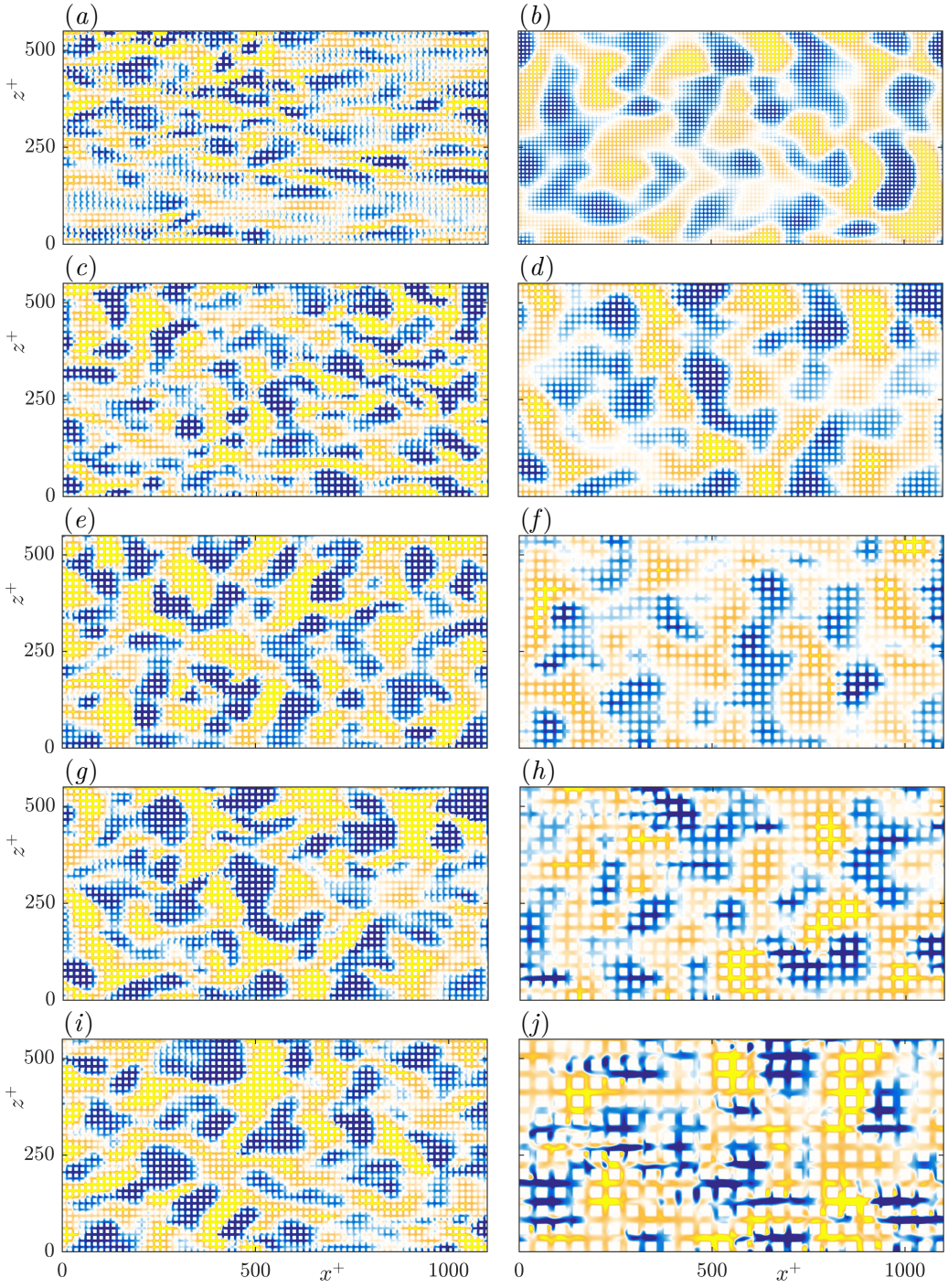

FIGURE 4.12 Instantaneous realisations of the wall-normal velocity at $y^+ = -10$ (left column) and $y^+ = -40$ (right column), normalised by u_τ. From top to bottom, the left column represents cases H16 to H128; and right column, cases S10 to S48. The clearest and darkest colours indicate intensities of $\pm(0.1, 0.2, 0.3, 0.3, 0.3)$ in the left column and, from top to bottom, $\pm(0.05, 0.2, 0.4, 0.4, 0.5)$ in the right column.

wall-normal velocity fluctuations decay much slower, as shown in figure 4.7. This is also illustrated by the velocity fluctuations of the canopies of family H, where the wall-normal velocity fluctuations within the canopy require larger canopy heights to asymptote compared to the wall-parallel fluctuations. The presence of wall-normal fluctuations deep within the canopy is a reflection of the canopy layout obstructing the wall-normal flow less than the tangential flow. It will be shown in §5.3 that, for the present canopies, the effective drag coefficient in the tangential directions can be up to three times larger than in the wall-normal direction. Within a canopy with a large height, the only mechanism to inhibit the velocity fluctuations away from the canopy base is through the effect of the canopy drag. As the canopy geometries studied here exert more drag on the wall-parallel flow than the wall-normal flow, u' and w' decay faster than v' within the canopy.

The formation of the Kelvin–Helmholtz-like instability over canopies is also affected by the spacing between elements. To study this effect, we compare the pre-multiplied spectral energy densities of the wall-normal velocities for the canopies of family S, which have a constant height and different element spacings. For the canopy with the smallest spacing, S10, the energetic wavelengths in the flow at $y^+ \approx 15$ are similar to those in smooth-wall flows, and the footprint of the instability in the flow is weak, as shown in figure 4.10(a). As the element spacing is increased, there is an increase in the energy in wavelengths associated with the Kelvin-Helmholtz-like instability. This suggests that this instability is inhibited in very dense canopies, possibly due to the large drag they exert on the velocity fluctuations (White & Nepf, 2007; Sharma *et al.*, 2017). In addition to the increase in the energy associated with the instabilities, the increase in element spacing also results in a progressive decrease in the overlapping regions in the energy densities of the canopy and smooth-wall flows, with a reduction in the energy in large streamwise wavelengths $\lambda_x^+ \gtrsim 700$. We also observe that, while in the canopies of family H the streamwise wavelength of the instability was roughly constant independently of the canopy height, the increase in the element spacing results in an increase in the streamwise wavelength of the instability from $\lambda_x^+ \sim 140$ for case S10 to $\lambda_x^+ \sim 280$ for case S48. If the element spacing was increased further, the Kelvin–Helmholtz-like instability would eventually weaken, and for sparse enough canopies the flow within would begin to resemble smooth-wall flow perturbed by the element-induced flow of the isolated canopy elements as demonstrated in chapter 3 and in previous studies of sparse canopy flows (Poggi *et al.*, 2004; Pietri *et al.*, 2009; Huang *et al.*, 2009).

Finally, let us focus on the self-similar canopy geometries of family G. The effect of increasing the size of the canopy elements produces similar effects on the pre-multiplied spectral energy densities as for the canopies of family S, discussed in the previous paragraph. For the densest canopy, G10, the spectral energy densities at $y^+ \approx 15$ collapse with those over a smooth wall, as shown in figures 4.13(a–d). As the size of the canopy is increased, we observe a stronger footprint of the Kelvin–Helmholtz-like instability in the energy densities, and there is also a progressive increase in the streamwise wavelengths associated with the

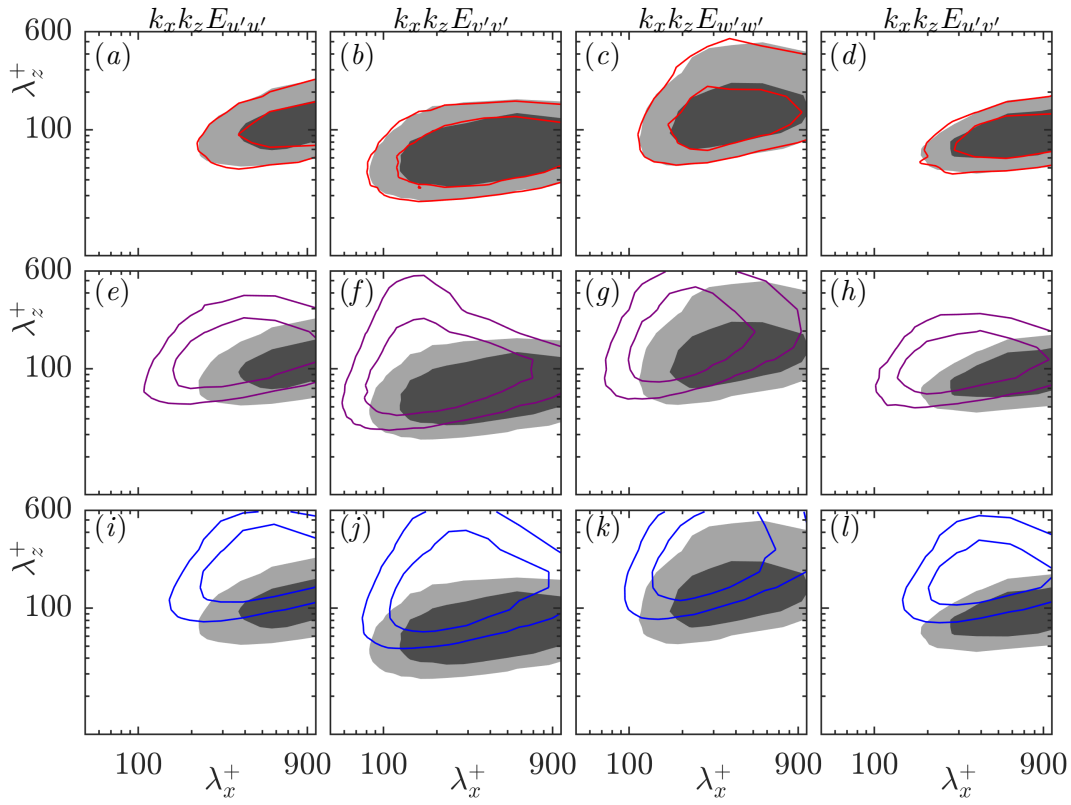

FIGURE 4.13 Pre-multiplied spectral energy densities at $y^+ \approx 15$ normalised by their respective rms value. The line contours represent (a–d) case G10; (e–h) case G40; (i–l) case G100. The filled contours represent case SC. The contours in (a, e, i), (b, f, j), (c, g, k) and (d, h, l) are in increments of 0.075, 0.06, 0.07, and 0.1, respectively.

instability. We also use the canopies of family G to illustrate the effect of increasing the canopy size on the spectral energy densities of the streamwise and spanwise fluctuations, and the Reynolds shear stresses, portrayed in figure 4.13. The distinct region in the wall-normal spectral energy densities associated with the Kelvin–Helmholtz-like instability is not apparent in the energy densities of the other velocity fluctuations and the Reynolds shear stresses. As the canopy size increases, we observe an increase in the energy in streamwise wavelengths associated with the instability, along with a general increase in the energy in large spanwise wavelengths compared to smooth-wall flows. We can also observe these effects qualitatively in the instantaneous realisations of the wall-normal velocity, shown in figure 4.5. For case G10, the structures observed in the instantaneous flow field are predominantly streamwise-coherent, as for smooth walls (Kline *et al.*, 1967; Jiménez & Pinelli, 1999). As the canopy size increases, we observe a gradual breakup of this streamwise coherence and an increase in the presence of spanwise-coherent structures.

The results discussed in this section suggest that the growth of the Kelvin–Helmholtz-like instability depends on both the canopy height and the element spacing. The streamwise wavelength of the instability, however, seems to depend mainly on the element spacing. The streamwise wavelength of the Kelvin–Helmholtz-like instability is determined by the shear length, $L_s = U/(dU/dy)$, calculated at the canopy-tip plane (Raupach *et al.*, 1996; White & Nepf, 2007; Nepf, 2012). Nepf *et al.* (2007) showed that the shear length L_s in canopy flows, in turn, is determined by the mean streamwise canopy drag coefficient. Intuitively, in tall, dense canopies, we would expect this drag coefficient to be a function of the element spacing. Therefore, the canopies of family H, which have a constant element spacing, will have similar mean drag coefficients and, consequently, similar instability wavelengths, as observed in the spectral energy densities of the fixed-spacing canopies. For the canopies of families S and G, increasing the element spacing would decrease the canopy drag coefficient, thereby resulting in the larger instability wavelengths observed. The effect of the canopy spacing on the drag coefficients and the instability wavelengths will be discussed further in §5.3. With regard to the effect of the canopy parameters on the intensity of the instability, White & Nepf (2007) postulated that the growth of the instability over dense canopies was governed by two competing effects, the shear at the canopy tips and the canopy drag. Canopies with closely packed elements would result in larger shear and a stronger inflection point at the canopy-tip plane, which would enhance the instability, but at the same time, a denser canopy would also produce a larger drag, which would inhibit the instability (Sharma *et al.*, 2017). This effect is observed for the canopies of families S and G, where increasing the element spacing, or reducing the canopy drag, results in a stronger footprint of the instability in the flow.

4.3.1 Effect of Re_τ on the Kelvin–Helmholtz-like instability

It was shown in §4.1.1, that the turbulent fluctuations over dense canopies scale in friction units, and therefore similar results are obtained when simulating canopies with the same height and spacing in friction units at different friction Reynolds numbers. In this section, we expand discussion in §4.1.1 to discuss the effect of changing the friction Reynolds number on the Kelvin–Helmholtz-like instability over dense canopy flows. It can be observed in figure 4.4(b) that the signature of this instability in simulations $\mathrm{H32}_{180}$ and $\mathrm{H32}_{400}$ are essentially the same, and that the associated streamwise wavelength for both cases is roughly $\lambda_x^+ \approx 150$. As discussed above, the wavelength and amplification of the instability are governed by the shear at the canopy tips. As the canopy parameters for cases $\mathrm{H32}_{180}$ and $\mathrm{H32}_{400}$ are kept constant in friction units, we can also expect the shear at the canopy tips to also be similar. Therefore, the instability characteristics for both these canopies are essentially the same when scaled in friction units. A similar behaviour has been reported for Kelvin–Helmholtz-like instabilities originating over riblets (García-Mayoral & Jiménez, 2012) and permeable substrates (Gómez-de-Segura & García-Mayoral, 2019).

Chapter 5

Analysis of Kelvin–Helmholtz-like instabilities over dense canopies

Parts of this chapter have been published in Flow, Turbulence and Combustion, 100 (4), 995–1014, with Garazi Gómez-de-Segura and Ricardo García-Mayoral as co-authors. The work presented in §5.1 was done in collaboration with Garazi Gómez-de-Segura.

In chapter 4, the appearance of Kelvin–Helmholtz-like instabilities was observed in the flow for certain dense canopy configurations. In this chapter, we present models based on linear stability analysis to capture these instabilities. The effect of changing canopy parameters on the formation of the instabilities is investigated. Owing to the spanwise coherent nature of the Kelvin–Helmholtz-like instability, we will only consider two-dimensional domains. The effect of the canopies on the flow is modelled using two methods. In the first, the canopy is modelled as an anisotropic permeable substrate governed by Brinkman's equation (Brinkman, 1949). Canopy-like substrates would provide less resistance to the flow in the wall-normal direction than the streamwise direction, and therefore will have a ratio of the streamwise and wall-normal permeabilities less than one. The stability analysis is conducted on a turbulent mean profile in a channel, with the canopies represented by boundary conditions derived from the analytic solution of Brinkman's equations applied at the location of the canopy-tip plane. From this analysis, we find that, for deep substrates, the parameter governing the instability is the geometric mean of the streamwise and wall-normal permeabilities. We also use this model to study the effect of a mean inclination of the canopy elements on the instability. The methodology used and the results obtained for the permeable substrate model are discussed in §5.1. In the second method, the effect of the canopy is modelled as a drag force in the Navier-Stokes equations. Different from the permeable substrate model, the drag force model also represents the mean flow within the canopies. We find that the drag-force model provides a more realistic representation of the instabilities for canopies with very low drag or high permeabilities values. The methodology and results for this model are presented in §5.2. In

the final part of the chapter, §5.3, we compare how well the predictions for the instabilities from the drag model compare with the instabilities observed in the DNSs.

5.1 Permeable-substrate model

In this section, we present the results obtained from a temporal, linear stability analysis of a turbulent mean flow in a symmetric channel bounded by canopies. We will only consider very dense canopies which preclude the penetration of turbulent fluctuations within them. In addition, we also assume that the element spacings are small enough to ensure that inertial effects within the canopy would be negligible. For such canopies, it would be reasonable to assume that the flow within is governed by Brinkman's equation. These equations are solved analytically to obtain a general relation for the velocities and pressure at the canopy free-flow interface. This relation is then used to provide boundary conditions for the flow above the canopy-tip plane. Note that the effect of the canopies on the overlying flow is represented entirely by this boundary condition in this analysis.

5.1.1 Solution of Brinkman's equation

The flow within the canopies is assumed to be governed by Brinkman's equation along with the continuity equation

$$\widetilde{\nu}\nabla^2\boldsymbol{u} - \nu\boldsymbol{K^{-1}}\boldsymbol{u} - \nabla p = 0, \tag{5.1}$$

$$\nabla\cdot\boldsymbol{u} = 0, \tag{5.2}$$

where $\boldsymbol{u}$ is the velocity vector, p is the pressure, $\boldsymbol{K^{-1}}$ is the inverse permeability tensor, ν is the fluid, or the pore-scale, viscosity, and $\widetilde{\nu}$ is an effective macroscale viscosity, which depends on the geometry of the substrate. For canopy-like substrates, where the flow within and outside the substrate is well-connected, that is, where shear can be effectively communicated across the canopy-flow interface, it is reasonable to set $\widetilde{\nu} = \nu$ (Abderrahaman-Elena & García-Mayoral, 2017; Lévy, 1983; Auriault, 2009). As the domain considered is periodic in x, we take a Fourier transform in this direction of equations (5.1) and (5.2) to yield

$$\nu\frac{\mathrm{d}^2\hat{u}}{\mathrm{d}y^2} - \nu\left(\alpha^2 + \frac{1}{K_x}\right)\hat{u} - i\alpha\hat{p} = 0, \tag{5.3}$$

$$\nu\frac{\mathrm{d}^2\hat{v}}{\mathrm{d}y^2} - \nu\left(\alpha^2 + \frac{1}{K_y}\right)\hat{v} - \frac{\mathrm{d}\hat{p}}{\mathrm{d}y} = 0, \tag{5.4}$$

$$i\alpha\hat{u} + \frac{\mathrm{d}\hat{v}}{\mathrm{d}y} = 0, \tag{5.5}$$

where the hatted variables are in Fourier space, α is the streamwise wavenumber, and K_x and K_y are the streamwise and wall-normal permeabilities of the canopy, respectively. These

equations can then be reduced to a single, fourth-order ordinary differential equation for the pressure

$$\frac{\mathrm{d}^4\hat{p}}{\mathrm{d}y^4} - \frac{\mathrm{d}^2\hat{p}}{\mathrm{d}y^2}\left(2\alpha^2 + \frac{1}{K_x}\right) + \hat{p}\left(\alpha^4 + \frac{\alpha^2}{K_y}\right) = 0. \tag{5.6}$$

Equation (5.6) has the characteristic roots

$$\pm r_1 = \pm\sqrt{\frac{2\alpha^2K_x + 1 + \sqrt{4\alpha^2K_x\left(1 - \frac{K_x}{K_y}\right) + 1}}{2K_x}}, \tag{5.7}$$

$$\pm r_2 = \pm\sqrt{\frac{2\alpha^2K_x + 1 - \sqrt{4\alpha^2K_x\left(1 - \frac{K_x}{K_y}\right) + 1}}{2K_x}}. \tag{5.8}$$

These roots, apart from the case where $r_1 = r_2$, yield solutions to equation (5.6) of the form

$$\hat{p} = A_1\exp(r_1y) + A_2\exp(-r_1y) + A_3\exp(r_2y) + A_4\exp(-r_2y), \tag{5.9}$$

where the constants A_i are obtained by applying no-slip and impermeability conditions at the bottom boundary of the canopies $y = -h$, and continuity of pressure and shear at the top boundary of the canopy elements, $y = 0$. We obtain solutions of similar forms for $\hat{u}$ and $\hat{v}$ by substituting the expression for $\hat{p}$ into equations (5.3)–(5.5). This solution to the Brinkman's equation splits into two qualitatively distinct branches depending on whether K_x/K_y is greater or less than $1 + 1/(4\alpha^2K_x)$. If K_x/K_y is greater than this value, then the roots r_1 and r_2 are complex conjugates, and if it is less than this value, r_1 and r_2 are real. In the case of canopies we expect smaller streamwise permeabilities than wall-normal ones, $K_x/K_y < 1$, and with small streamwise permeabilities, so we will mainly focus on the latter condition. Permeable substrates in the opposite limit, $K_x/K_y > 1$, can be used to reduce turbulent skin friction drag, and the results from this limit are discussed in Gómez-de-Segura & García-Mayoral (2019) and Gómez-de-Segura (2019).

In flows governed by Brinkman's equation, the region within the substrate near the substrate-fluid interface is characterised by a penetration depth or the 'Brinkman boundary-layer', which is the thickness of the high shear region below the interface. This penetration depth for the mean flow into isotropic permeable substrates is observed to scale with the square root of the substrate permeability (Saffman, 1971; Battiato, 2012). In the present analysis, however, we consider substrates with anisotropic permeabilities, K_x and K_y, and also scales other than the mean, characterised by their wavenumber, α. In such cases we observe the penetration depth, L_p, to be set by the characteristic roots of equation (5.9), r_1 and r_2. For the cases with $K_x/K_y < 1$, we find that the penetration depth is given by $L_p = 1/r_2$. This is illustrated in figure 5.1, which shows that the normalised velocity and pressure profiles within the permeable substrate collapse when L_p is used to scale the

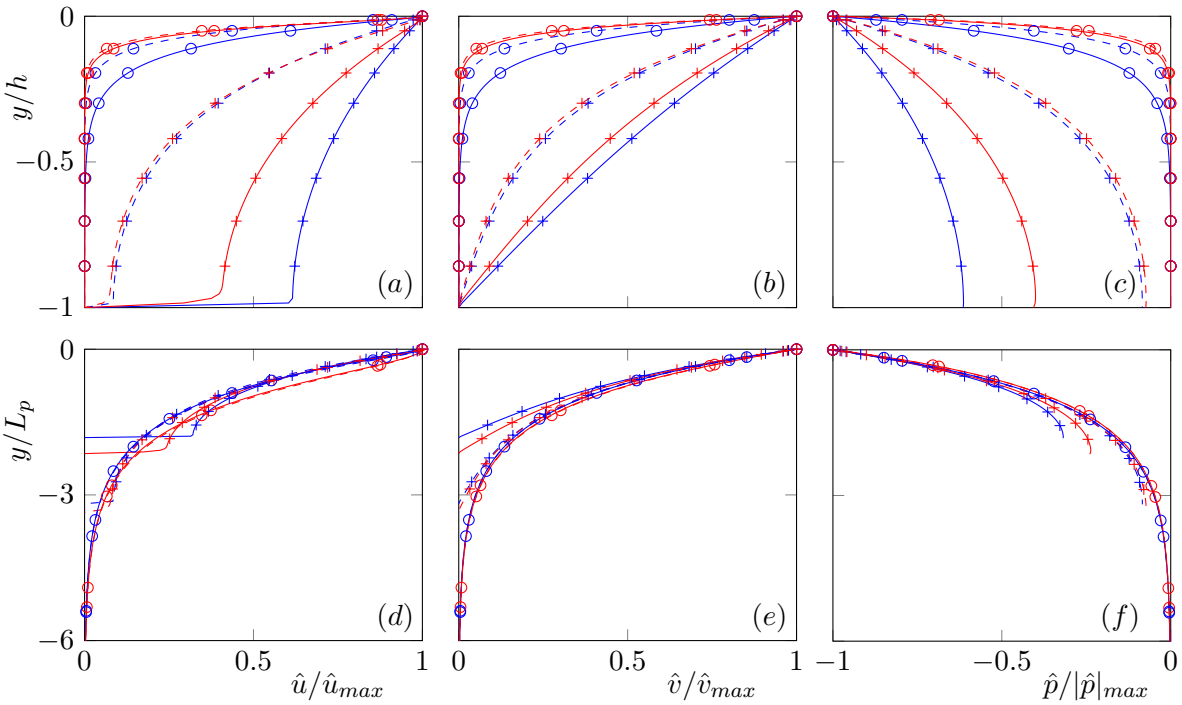

FIGURE 5.1 Normalised velocity and pressure profiles within the substrate, with the wall-normal coordinate scaled by (*a*–*c*) the substrate thickness, $h^+ = 250$, and (*d*–*f*) $L_p = 1/r_2$ from equation (5.8). The blue and red lines represent substrates with $K_x^+ = 1$ and 10, respectively; —, $K_x/K_y = 10^{-1}$; - - -, $10^{-1.5}$; +, $\lambda^+ = 2\pi/\alpha \approx 150$; and ○, $\lambda^+ \approx 30$.

wall-normal coordinate. In the limit where $K_x/K_y << 1$ and $K_x\alpha^2 < 1$, the expression for L_p reduces to

$$L_p = \left(\alpha\sqrt{K_x/K_y + \alpha^2 K_x}\right)^{-1}. \tag{5.10}$$

This suggests that the depth of penetration of the overlying flow into the canopy, even for very low permeability ratios, is set by both K_x and K_y along with the wavelength of the overlying perturbation. For the mean flow, however, this depth is still given by $L_p = \sqrt{K_x}$, which is obtained by substituting $\alpha = 0$ in the expression for r_1 given in equation (5.7).

5.1.2 Governing equations within the channel

The flow within the channel, between the canopy tips, is governed by the Navier-Stokes equations. For the purposes of the stability analysis, these equations are linearised about a mean flow, $U(y)$. The mean flow used here is an approximation of a smooth channel turbulent flow profile given by

$$\frac{\mathrm{d}}{\mathrm{d}y}\left([\nu + \nu_T(y)]\frac{\mathrm{d}U}{\mathrm{d}y}\right) - \frac{\mathrm{d}P}{\mathrm{d}x} = 0, y \in [0, 2\delta] \tag{5.11}$$

where $\nu_T(y)$ is the height-dependent eddy viscosity proposed by Cess (1958) to approximate turbulent smooth-channel flow and ν is the molecular viscosity. This profile has also been used to perform stability analysis over permeable substrates (Jimenez *et al.*, 2001; Abderrahaman-Elena & García-Mayoral, 2017) and riblets (García-Mayoral & Jiménez, 2011). Note that using a smooth-wall mean profile assumes that the canopy elements are very closely packed, and do not allow the overlying turbulence to penetrate within the canopy. Gómez-de-Segura (2019) has compared the results from an inviscid and viscous stability analysis for the domain considered here and observed that both analysis yield similar results, as the Kelvin–Helmholtz instability is essentially an inviscid phenomenon. Therefore, we only discuss results from an inviscid analysis here. The governing equations for the inviscid stability analysis are

$$\frac{\partial u}{\partial t} + U\frac{\partial u}{\partial x} + U'v = -\frac{\partial p}{\partial x}, \tag{5.12}$$

$$\frac{\partial v}{\partial t} + U\frac{\partial v}{\partial x} = -\frac{\partial p}{\partial y}, \tag{5.13}$$

$$\frac{\partial u}{\partial x} + \frac{\partial v}{\partial y} = 0, \tag{5.14}$$

where small letters denote fluctuating components and the capital letters denote mean quantities. The prime symbol denotes the derivative with respect to the wall-normal direction. Assuming wavelike solutions of the form $y = \widetilde{v}e^{i(\alpha x-\omega t)}$, the above equations can be reduced to Rayleigh's equation (Drazin & Reid, 1998; Schmid & Henningson, 2012)

$$[\alpha U(\mathrm{D}^2 - \alpha^2) - \alpha U'']\widetilde{v} = \omega(\mathrm{D}^2 - \alpha^2)\widetilde{v}. \tag{5.15}$$

where D represents the operator $\mathrm{d}/\mathrm{d}y$. Equation (5.15) is an eigenvalue problem, which is solved numerically for complex values of ω and for real values of the wavenumber, α, using Chebyshev pseudospectral discretisation. The real part of ω, ω_r, gives the angular frequency of the instability, and its imaginary part, ω_i, gives the instability growth rate. The instability is considered to be amplified in the flow for positive values of ω_i.

As mentioned in the introduction to this chapter, the flow within the canopies and in the channel are coupled by means of a boundary condition at the canopy-flow interface. This boundary condition is obtained by taking the value of the expression for v within the substrate at the interface, $y = 0$, for a given overlying shear and pressure. As the overlying flow considered is inviscid, the shear is set to zero, which yields the impedance condition $\widetilde{v}|_{y=0} = -\beta\widetilde{p}|_{y=0}$, where β is a function of K_x, K_y, h and α. Note that a similar boundary condition was also used in the studies of Jimenez *et al.* (2001) and Abderrahaman-Elena & García-Mayoral (2017) to represent permeable substrates. Substituting this value for the

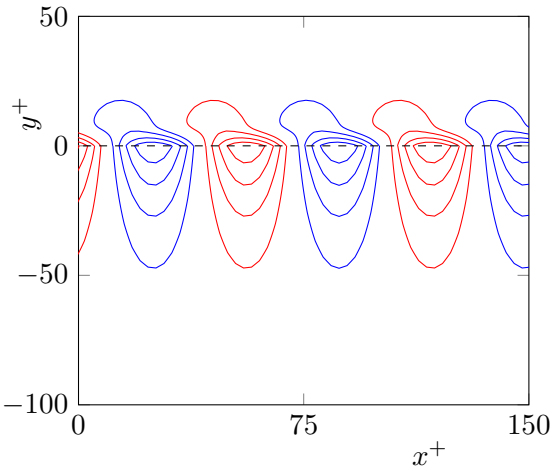

FIGURE 5.2 Contours of the stream function for the most amplified mode for canopy with height, $h^+ = 100$, streamwise permeability, $K_x^+ = 4$ and anisotropy ratio $K_x/K_y = 10^{-1}$. The blue and red lines correspond to clockwise and counter-clockwise rotation, respectively. The horizontal line marks the location of the canopy tips.

pressure in equation (5.12), we obtain

$$\left(\alpha(U\mathrm{D} - U') - i\frac{\alpha^2}{\beta}\right)\widetilde{v} = \omega \mathrm{D}\widetilde{v}, \tag{5.16}$$

which is the boundary condition used to solve equation (5.15). Note that in the mean velocity profile of a real canopy there would be some non-zero mean velocity at the canopy tips, whereas it is zero for the smooth-wall-like Cess profile used. It was noted by García-Mayoral & Jiménez (2011) and Gómez-de-Segura *et al.* (2018*a*), however, that adding a slip velocity at the interface only affects the angular frequency of the instability, ω_r, and not the instability growth rate, ω_i, in which we are primarily interested.

5.1.3 Effect of varying canopy parameters on instability

The relaxation of the impermeability boundary condition at the channel walls by applying the boundary condition given by equation (5.16), results in the growth of a Kelvin–Helmholtz-like instability in the channel, originating at the canopy-channel interface (Jimenez *et al.*, 2001; Abderrahaman-Elena & García-Mayoral, 2017). This instability can be visualised through the contours of the streamfunction of the eigenvector corresponding to the most amplified eigenvalue, obtained from the stability analysis, portrayed in figure 5.2. The canopy instability takes the form of alternating clockwise and counter-clockwise rollers characteristic of the Kelvin–Helmholtz-like instability.

The instabilities with the highest growth rate, for a wide range of substrate permeabilities occur at a wavelength of $\lambda_x^+ \approx 60$, as shown in figure 5.3(a), similar to the results of

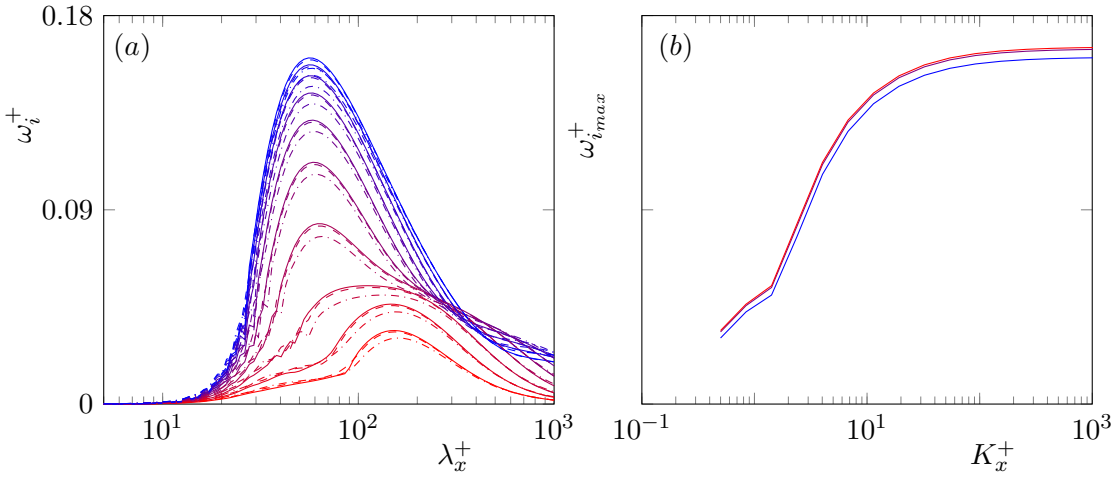

FIGURE 5.3 (*a*) Growth rate, ω_i^+, as a function of the instability wavelength λ_x^+ for canopies with $h^+ = 100$ and $K_x/K_y = 10^{-1}$ for varying permeabilities and friction Reynolds numbers. From red to blue permeabilities increase from $K_x^+ = 0.5$ to 10^5. The lines represent ——, $Re_\tau = 1000$; - - -, $Re_\tau = 550$; and -·-·-, $Re_\tau = 180$. (*b*) Growth rate of wavelength with maximum amplification as a function of the streamwise permeability for different friction Reynolds numbers. The colours from red to blue represent $Re_\tau = 1000, 550$ and 180.

García-Mayoral & Jiménez (2011) and Abderrahaman-Elena & García-Mayoral (2017). The wavelength of the Kelvin–Helmholtz-like instability is generally set by the shear-layer thickness at the canopy-tip plane (Raupach *et al.*, 1996; White & Nepf, 2007; Nepf, 2012). The shear-layer thickness, in turn, is set by the shape of the mean velocity profile. For a Cess profile, this thickness is set by the height above the interface where the vorticity gradient peaks, $y_c^+ \approx 5$–10, (García-Mayoral & Jiménez, 2011). The similarities in the instability wavelength observed in the present study and the studies of García-Mayoral & Jiménez (2011) and Abderrahaman-Elena & García-Mayoral (2017) are, therefore, a possible consequence of using the same mean-velocity profile to perform the stability analysis. García-Mayoral & Jiménez (2011) also noted that as the location of this peak scales in viscous units, the instability also scales in viscous units. This is also demonstrated in figure 5.3, which shows that the results of the stability analysis for substrates with the same parameters in viscous units at different friction Reynolds numbers are essentially the same. The scaling of the Kelvin–Helmholtz-like instability in viscous units was also noted in the results of the DNSs, discussed in chapter 4. It may be noted here that the wavelengths predicted by the current analysis, $\lambda_x^+ \approx 60$, are about half the smallest instability wavelength observed in the dense canopy DNSs, $\lambda_x^+ \approx 100$. A factor of two difference between the predictions of the stability analysis and the DNSs was also noted by García-Mayoral & Jiménez (2011). The underprediction of the instability wavelength is likely due to the fact that the analysis does not have information of the mean-velocity profile within the canopy, and consequently, the contribution of the shear-layer within the canopy to the instability wavelength is ignored.

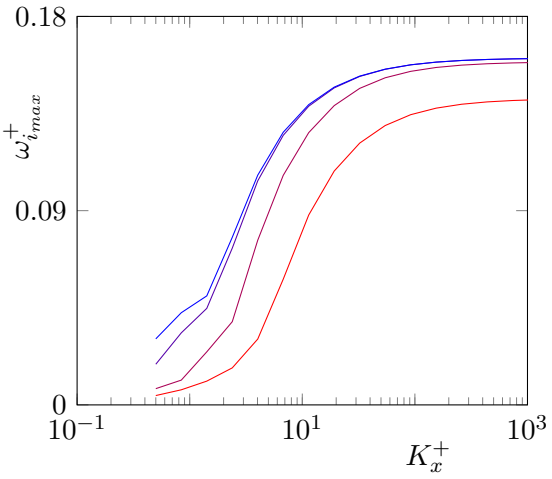

FIGURE 5.4 Growth rate of wavelength with maximum amplification as a function of the streamwise permeability for substrates with $K_x/K_y = 10^{-1}$ for different canopy heights; from red to blue, lines indicate $h^+ = 10, 20, 50$ and 100.

We observe that, for a fixed canopy height, increasing the permeability of the canopy results in a larger instability growth rate, as shown in figure 5.3. The growth rate asymptotes for very large permeabilities. It was noted by Jimenez *et al.* (2001), that in the limit of very large permeabilities the boundary condition used to represent the canopies acts as a mirror condition. The analysis then becomes equivalent to that of a free-shear layer, which provides the maximum instability growth rate. Note that in a real canopy this limit is not achievable, as for very large permeabilities we would recover smooth wall like flow within the canopy region as well, similar to the sparse canopies discussed in chapter 3. This asymptotic behaviour is therefore also a consequence of not representing the mean flow within the canopy region in the analysis. For canopies with very low permeabilities, we observe the amplification of a high wavelength, secondary instability is predicted, as can be observed in figure 5.3, which will be discussed further in §5.2.3.

Varying the canopy height also has an effect on the instability growth rates. In short canopies, the instability is likely restricted by the impermeability condition at the canopy base (Huerre, 1983; Healey, 2009), and therefore result in a smaller asymptotic growth rate at large permeabilities, compared to deep canopies, as illustrated in figure 5.4. The effect of the height asymptotes, when the height becomes larger than the penetration depth of the flow within the canopy, discussed in §5.1.1.

We also find that the effect of varying the different canopy parameters on the instability with the largest growth rate can be characterised by a single, empirically fitted parameter

$$\kappa^+_{Br} = \sqrt{K_x^+ K_y^+}\tanh\left(\frac{h}{2y_c}\sqrt{\frac{K_x}{K_y}}\right)\tanh^2\left(\frac{h}{\sqrt{K_x}}\right), \quad \frac{K_x}{K_y} \lesssim 1. \tag{5.17}$$

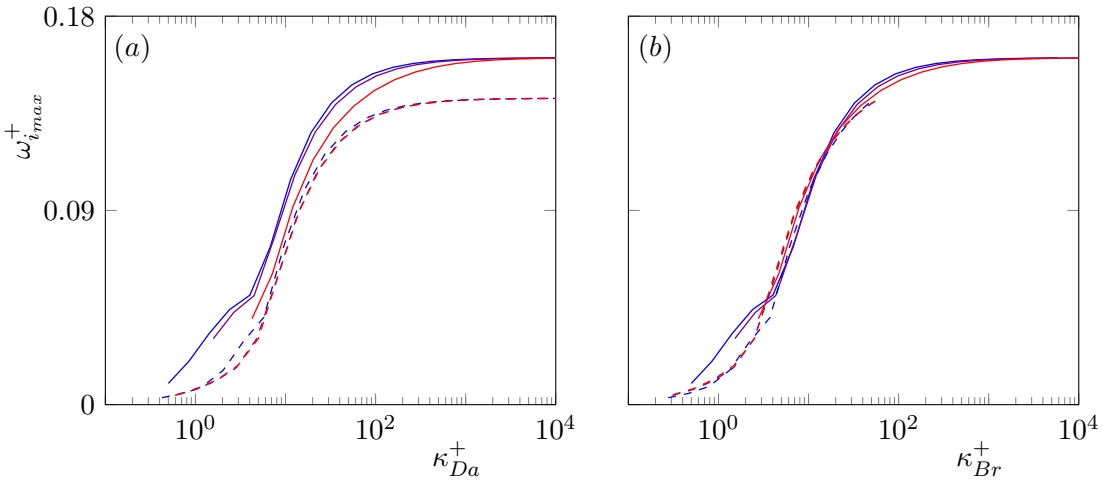

FIGURE 5.5 Growth rate of the wavelength with maximum amplification as a function of (a) κ^+_{Da} and (b) κ^+_{Br} for different canopy heights and anisotropy ratios. The colours from red to blue represent $K_x/K_y = 10^0, 10^{-1}$ and 10^{-2}; - - -, $h^+ = 10$; and ——, $h^+ = 100$.

It can be observed in figure 5.5(b), that the growth rates of the most amplified instability wavelength for canopies with widely varying heights and permeabilities essentially collapse when plotted against κ_{Br}. Note that the above parameter is only valid for cases where $K_x/K_y < 1$. The parameter governing the instability in the opposite limit is $\sqrt{K_y^+}$, and this limit is discussed in Gómez-de-Segura *et al.* (2018*a*) and Gómez-de-Segura (2019). For canopies with large heights, this expression can be simplified to

$$\kappa^+_{Br} \approx \sqrt{K_x^+ K_y^+}. \tag{5.18}$$

Therefore, the present analysis suggests that the growth of the Kelvin–Helmholtz-like instability over canopies depends on both their streamwise and wall-normal permeabilities. Abderrahaman-Elena & García-Mayoral (2017), who performed stability analyses for flow over substrates governed by Darcy's equation observed that the parameter characterising the instability in such flows was

$$\kappa^+_{Da} = \sqrt{K_x^+ K_y^+}\tanh\left(\frac{h}{y_c}\sqrt{\frac{K_x}{K_y}}\right), \tag{5.19}$$

which, for large enough substrate heights, gives the leading order parameter $\sqrt{K_x^+ K_y^+}$, the same as the one obtained for substrates governed by Brinkman's equation. The parameter given by equation (5.19) cannot capture the instability behaviour over substrates with small heights, as can be observed in figure 5.5(a). However, while the analysis of Abderrahaman-Elena & García-Mayoral (2017) predicted the same parameter, $\sqrt{K_x^+ K_y^+}$, characterising the instability for substrates with $K_x/K_y \lesssim 1$, in substrates governed by Brinkman's equation, it

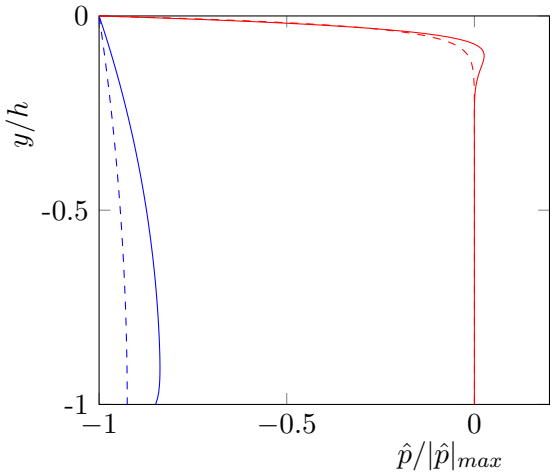

FIGURE 5.6 Variation of the pressure within a substrate governed by Darcy's equation (- - -) and Brinkman's equation (——); with the blue lines representing $K_x/K_y = 10^{-2}$ and red lines $K_x/K_y = 10^2$.

was found that K_y^+ governs the instability for substrates with $K_x/K_y > 1$ (Gómez-de-Segura *et al.*, 2018*a*). This dichotomy in the instability characteristics can be explained by the pressure profiles within the different types of substrates. We compare the pressure profiles for substrates governed by both Brinkman's and Darcy's equations, with K_x/K_y greater than and less than one, in figure 5.6. We observe in this figure that in streamwise-preferential substrates, the pressure decays quickly below the substrate-flow interface owing to their small wall-normal permeabilities. This results in a large pressure gradient in this region, which would, in turn, result in large scale diffusive effects near the interface that cannot be captured by Darcy's equation. For wall-normal-preferential substrates like canopies, however, the decay in the pressure below the substrate-flow interface is very gradual. We would, therefore, expect the large scale diffusive effects to be small, which is reflected by the fact that both Darcy's and Brinkman's equations yield qualitatively similar results for such substrates.

5.1.4 Effect of canopy element inclination

We now investigate the effect that a mean inclination of the canopy elements would have on the instability characteristics. Such an arrangement would be akin to a flexible canopy, with low stiffness, bending under a mean flow, or a canopy with slanted elements. Although in the bending of flexible canopies the height of the canopies would change as they are bent, presently we ignore this effect and the change in height is considered as a different parameter. A schematic of the canopy arrangement studied is portrayed in figure 5.7. For such canopies,

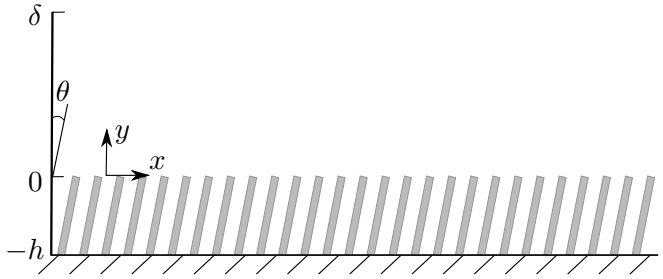

FIGURE 5.7 Schematic representation of rigid canopy elements rotated by an angle θ from the vertical.

the inverse permeability tensor is given by

$$\boldsymbol{K^{-1}} = \begin{bmatrix} \frac{\cos^2\theta}{K_x} + \frac{\sin^2\theta}{K_y} & \sin\theta\cos\theta(\frac{1}{K_x} - \frac{1}{K_y}) \\ \sin\theta\cos\theta(\frac{1}{K_x} - \frac{1}{K_y}) & \frac{\sin^2\theta}{K_x} + \frac{\cos^2\theta}{K_y} \end{bmatrix} = \begin{bmatrix} \frac{1}{K_{11}} & \frac{1}{K_{12}} \\ \frac{1}{K_{21}} & \frac{1}{K_{22}} \end{bmatrix}, \tag{5.20}$$

where K_x and K_y are the permeabilities in the principal directions of a canopy with elements aligned perpendicular to the flow, and θ is mean rotation angle measured from the perpendicular of the rotated canopy elements. The modified Brinkman's equation for such configurations can be obtained by substituting the value of $\boldsymbol{K^{-1}}$ from equation (5.20) into equation (5.1). The modified Brinkman's equations are solved analytically as before. The coupling of the flow within the canopies and the channel is also through the impedance boundary condition described in §5.1.2. We find that rotating the canopy elements does not have a significant effect on the instabilities for rotation angles upto 30°, even for canopies with very small values of K_x/K_y, as shown in figure 5.8. Beyond a rotation angle of 45°, the ratio of the permeabilities in the principal directions for the rotated canopies, K_{11}/K_{22}, becomes larger than one and the substrate becomes streamwise preferential. In addition, the element rotation has a larger effect on the instability for small canopy heights, with an increase in their growth rate observed with increasing rotation angles. The variation in the canopy heights which would result as a consequence of the element rotation may have a larger effect on the instability. Canopies with small heights result in weaker instabilities owing to the blocking effect of the bottom wall, as discussed in §5.1.3.

5.2 Drag-force model

The analysis conducted using the permeable-substrate model did not include the effect of the mean velocity profile within the canopies in the stability analysis. As a consequence, the permeable-substrate model did not have information about the shear-layer thickness within the canopy, which may have led to this model under-representing the instability wavelength. In addition, the permeable-substrate model could not represent well the instabilities in

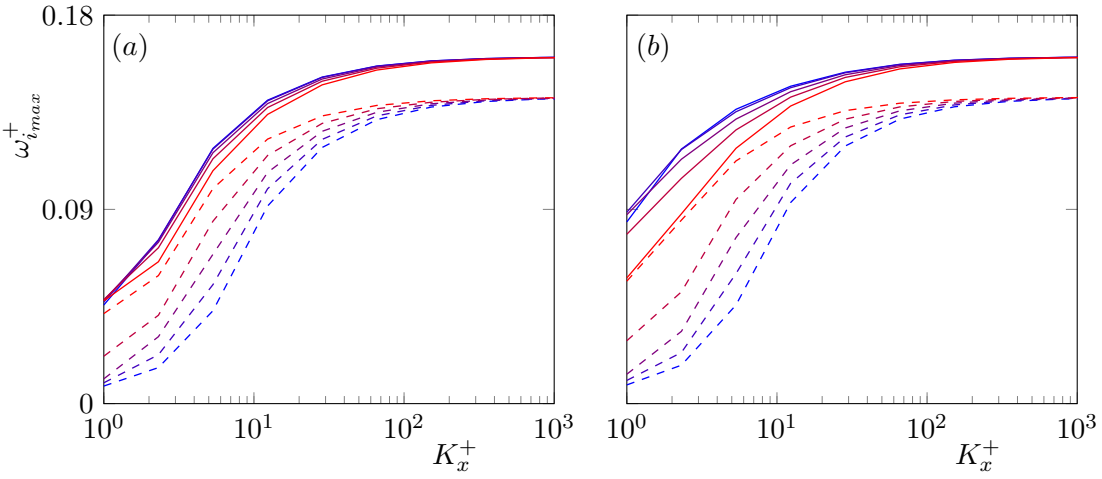

FIGURE 5.8 Growth rate of the wavelength with maximum amplification as a function of streamwise permeability for different element rotation angles, θ for (a) $K_x/K_y = 10^{-1}$ and (b) $K_x/K_y = 10^{-3}$. The colours from red to blue represent $\theta = 0°, 30°, 45°, 60°$ and $90°$; - - -, $h^+ = 10$; and ——, $h^+ = 100$.

canopies with large permeabilities. In this section, we present a model which represents the canopy elements in the stability analysis using a drag force in the Navier-Stokes equations.

5.2.1 Governing equations

We study the stability of flows in symmetric channels with canopy elements on both walls. For the purpose of the stability analysis, we model the effect of the canopy using a drag force in the Navier-Stokes equations, which results in the following governing equations

$$\frac{\partial \mathbf{u}}{\partial t} + \mathbf{u}\cdot\nabla\mathbf{u} = -\nabla p + \nu\nabla^2\mathbf{u} - C_i\mathbf{u}, \tag{5.21}$$

$$\nabla\cdot\mathbf{u} = 0, \tag{5.22}$$

where C_i is the effective canopy drag coefficient in each i^{th} direction, with $i = \{x, y\}$, assumed to be homogeneous over the entire canopy and zero outside it, as in Singh *et al.* (2016).

Linearising the equations (5.21) and (5.22) around the mean flow, $U(y)$, yields

$$\frac{\partial u}{\partial t} + U\frac{\partial u}{\partial x} + vU' = -\frac{\partial p}{\partial x} + \nu\nabla^2 u - C_x u, \tag{5.23}$$

$$\frac{\partial v}{\partial t} + U\frac{\partial v}{\partial x} = -\frac{\partial p}{\partial y} + \nu\nabla^2 v - C_y v, \tag{5.24}$$

$$\frac{\partial u}{\partial x} + \frac{\partial v}{\partial y} = 0. \tag{5.25}$$

These equations are used to obtain a modified Orr-Sommerfeld equation (Drazin & Reid, 1998; White & Nepf, 2007; Singh *et al.*, 2016; Zampogna *et al.*, 2016),

$$\left(\frac{\partial}{\partial t}+U\frac{\partial}{\partial x}+C_y\right)\nabla^2 v-\nu\nabla^4 v=U''\frac{\partial v}{\partial x}-(C_x-C_y)\frac{\partial^2 v}{\partial y^2}. \tag{5.26}$$

Assuming wavelike solutions of the form $v=\widetilde{v}e^{i(\alpha x-\omega t)}$, equation (5.26) reduces to the eigenvalue problem

$$\begin{aligned}(\alpha U-iC_y)(\mathrm{D}^2-\alpha^2)\widetilde{v}-\alpha U''\widetilde{v}-i(C_x-C_y)D^2\widetilde{v}\\ +i\nu(\mathrm{D}^4-2\alpha^2\mathrm{D}^2+\alpha^4)\widetilde{v}=\omega(\mathrm{D}^2-\alpha^2)\widetilde{v},\end{aligned} \tag{5.27}$$

where the prime superscript denotes differentiation with respect to y, and D represents the operator $\mathrm{d}/\mathrm{d}y$. Equation (5.27) is solved to obtain ω for real values of α, subject to no-slip and impermeability boundary conditions at the walls at the base of the canopies at the top and bottom of the channel. The instability is amplified for positive values of the imaginary part of ω. We use a compact finite difference algorithm to discretise equation (5.27), as it allows greater flexibility in determining the grid resolutions within the canopy, unlike the discretisation used in the permeable substrate model that required the use of Chebyshev collocation points which cluster near the channel boundaries.

In order to model the mean velocity profile in dense canopy flows we make the following assumptions. We only consider canopies with small element spacings so that the magnitude of inertial effects within the canopies would be small and are thus neglected. In addition, we also assume that turbulent stresses do not penetrate within (Nepf *et al.*, 2007), and are smooth-wall like above the canopy-tip plane. These assumptions are consistent with the observations from the DNS of flow over very dense canopies, discussed in chapter 4. The mean velocity outside the canopy could then be modelled using a smooth-channel eddy viscosity, with the canopy-tip plane acting as the location of the smooth-wall (Jimenez *et al.*, 2001; García-Mayoral & Jiménez, 2011; Gómez-de-Segura *et al.*, 2018*a*; Gómez-de-Segura & García-Mayoral, 2019). The equation for the mean velocity can then be written as

$$\frac{\mathrm{d}}{\mathrm{d}y}\left([\nu+\nu_T(y)]\frac{\mathrm{d}U}{\mathrm{d}y}\right)-\frac{\mathrm{d}P}{\mathrm{d}x} = 0, y\in[0,2\delta] \tag{5.28}$$

$$\nu\frac{\mathrm{d}^2U}{\mathrm{d}y^2}-C_xU-\frac{\mathrm{d}P}{\mathrm{d}x} = 0, y\in[-h,0)\cup(2\delta,2\delta+h] \tag{5.29}$$

where equation (5.28) is valid outside the canopy region and (5.29) within it. $C_x(y)$ is the average streamwise canopy drag coefficient, which is assumed constant within the canopy and zero outside, $\nu_T(y)$ is the eddy-viscosity proposed by Cess (1958) and is non-zero only outside the canopy, and ν is the molecular viscosity.

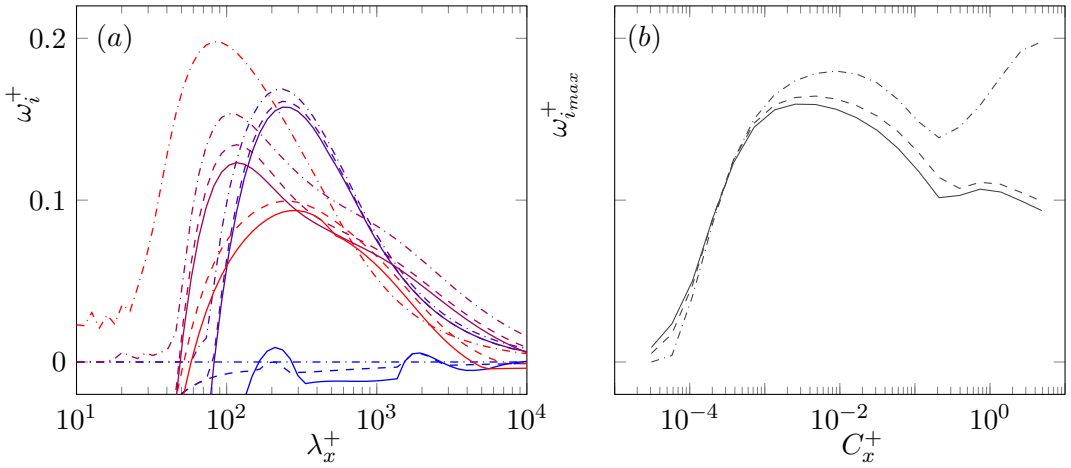

FIGURE 5.9 (*a*) Growth rate, ω_i^+, as a function of the instability wavelength λ_x^+ for canopies with $h^+ = 100$ and $C_x/C_y = 10^1$ for different drag coefficients. From blue to red the colours represent $C_x^+ \approx 10^{-5}, 10^{-3}, 10^{-2}$ and 10^{-1}. (*b*) Growth rate of wavelength with maximum amplification as a function of the streamwise drag coefficient. The lines represent ——, viscous analysis with eddy viscosity; - - -, molecular viscosity alone; and -·-·-, inviscid analysis.

5.2.2 Comparison of viscous and inviscid analysis

We now compare the results from an inviscid and viscous stability analysis of turbulent flow over canopies, performed using the method described above. As the Kelvin–Helmholtz-like instability is essentially an inviscid phenomenon, its main features can be captured using an inviscid stability analysis. The inclusion of viscosity in the analysis, however, results in some modification of the instability characteristics. The major effect of viscosity is on the small wavelengths in the flow, $\lambda_x^+ \sim 10$, which were marginally unstable in the inviscid analysis, but are stable in the viscous analysis, as can be observed in figure 5.9. The damping of small instability wavelengths by viscosity also results in the shift of the most amplified instability wavelength to larger scales and a reduction in the maximum growth rate of the instability, which is most significant for canopies with large drag coefficients. We have also conducted stability analyses including the effect of the eddy viscosity outside the canopy region. The results are essentially the same as the ones obtained using molecular viscosity alone, apart from a slight reduction in the instability growth rates, as can be observed in figure 5.9. The eddy viscosity does not have a larger effect on the instability likely because the flow near the canopy-tip plane, where the instability originates, is predominantly viscous and the value of ν_T is close to zero. As the inclusion of ν_T does not significantly affect the fastest growing instability wavelength or the peak instability growth rate, we only discuss the results the analyses including the molecular viscosity alone in the following sections.

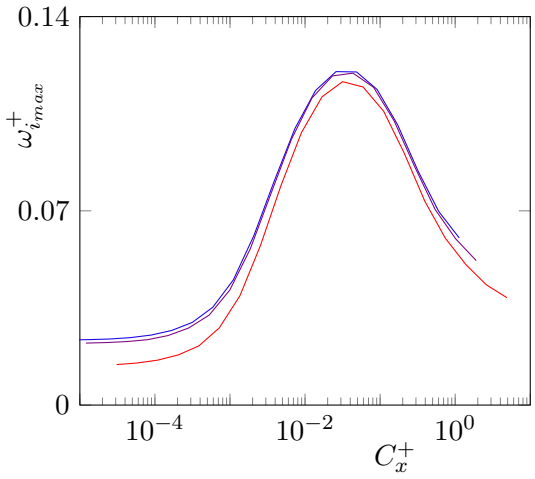

FIGURE 5.10 Growth rate of wavelength with maximum amplification as a function of the streamwise drag coefficient for different friction Reynolds numbers for canopies with $h^+ = 10$ and $C_x/C_y = 10^1$. The colours from blue to red represent $Re_\tau = 1000, 550$ and 180.

5.2.3 Effect of canopy parameters on the instability

We now study the effect of changing the canopy parameters on the Kelvin–Helmholtz-like instability. The effect of the spacing and the shape of the canopy elements are modelled through the mean canopy drag coefficients, C_x and C_y, and the canopy height, h. We only consider rigid canopy elements aligned normal to the flow direction, which would obstruct the streamwise flow more than the wall-normal flow, that is, with anisotropy ratios $C_x/C_y \gtrsim 1$.

The stability analysis using the drag model reaffirms that the canopy-flow instability scales in friction units measured at the canopy-tip plane. This is illustrated in figure 5.10, which shows that the instability growth rate for canopies with fixed parameters in friction units are essentially the same for different friction Reynolds numbers. The predicted instability growth rates for $Re_\tau = 180$ are slightly smaller than those for higher friction Reynolds numbers, but the same trends are observed. Over very dense canopies, such as those considered presently, this shear is also used to define the friction velocity that scales the overlying turbulence, as discussed in chapter 4. As noted in previous canopy studies, the canopy-flow instability also scales with the shear at the canopy-tip plane (Raupach *et al.*, 1996; Finnigan, 2000; Nepf, 2012), which results in the observed scaling of the instability in friction units.

For canopies with large drag coefficients or low permeabilities, the results obtained from permeable-substrate and drag-force model are qualitatively similar. In the case of canopies with very large drag coefficients, we obtain low instability growth rates. As the drag coefficient is decreased, initially we observe an increase in the growth rate of the instability similar to the results obtained from the permeable substrate model. As the drag coefficient is reduced further, the growth rate reaches a maximum value and then reduces again, as shown in figures 5.10 and 5.11. This behaviour of the instability was first noted by White & Nepf

(2007), who postulated that the growth of the instability over dense canopies was governed by two competing effects, the shear at the canopy-tip plane, which decides the strength of the inflection point in the mean velocity profile, and the canopy drag. Canopies with large drags would result in larger shear at the canopy-tip plane, which enhances the instability. At the same time, the canopy drag would also inhibit the fluctuations within it, which would weaken the instability. The strongest canopy-flow instabilities will, therefore, occur at intermediate values of canopy drag, which are sufficient to maintain a strong enough inflection point in the mean velocity, while not inhibiting the instability fluctuations excessively. The permeable substrate model, discussed in §5.1, was unable to capture the variations in the strength of the inflection point as it did not account for the mean velocity profile within the canopy. In addition, while the permeable-substrate model predicted a near constant wavelength of the Kelvin–Helmholtz-like instability, the drag model predicts the increase in the instability wavelength with a reduction in canopy drag. As noted previously, the wavelength of the canopy instability scales with the shear-layer thickness at the canopy-tip plane. As we use the Cess eddy-viscosity to model the effect of turbulence on the mean profile outside of the canopy, the part of the shear length above the canopy is $y_c^+ \approx 5$–10, similar to that for the permeable substrate model. The shear-layer thickness within the canopy would be set by the canopy drag (Nepf *et al.*, 2007). Near the canopy tips, if we consider a purely shear driven flow, equation (5.29) could be written as

$$\nu \frac{\mathrm{d}^2 U}{\mathrm{d}y^2} - C_x U = 0. \tag{5.30}$$

From dimensional arguments, the shear length within the canopy, L_s, would then scale with $\sqrt{\nu/C_x}$. We compare the correlation between L_s and $\sqrt{\nu/C_x}$ for canopies with two different heights for a range of C_x in figure 5.12, which demonstrates that the scaling is $L_s \sim \sqrt{\nu/C_x}$ when the drag lengthscale is smaller than the canopy height, $\sqrt{\nu/C_x} < h$. In the opposite limit, the maximum value of L_s is limited by the canopy height. We would, therefore, expect that the shear layer thickness, and consequently the instability wavelength, would increase when the drag coefficient is reduced. We can observe this effect in figure 5.11(a), where for a canopy with a small height the most amplified instability wavelength ranges from $\lambda_x^+ \approx 150$ for the largest C_x considered, and asymptotes to $\lambda_x^+ \approx 350$ for small values of C_x. For canopies with a large height, however, there is a deviation from this trend for large values of canopy drag. In figure 5.11(b), we observe the amplification of a large-wavelength instability for tall canopies with large drag coefficients. The contours of the instability stream function for this large-wavelength instability, portrayed in figure 5.13, show that it has a large wall-normal span extending up to $y^+ \approx 100$ compared to the instability for a smaller drag coefficient, which only extends up to $y^+ \approx 45$. This large-wavelength instability was also noted by Singh *et al.* (2016), who performed stability analyses similar to the one conducted here, except that the canopy was represented by a drag force varying with the square of the

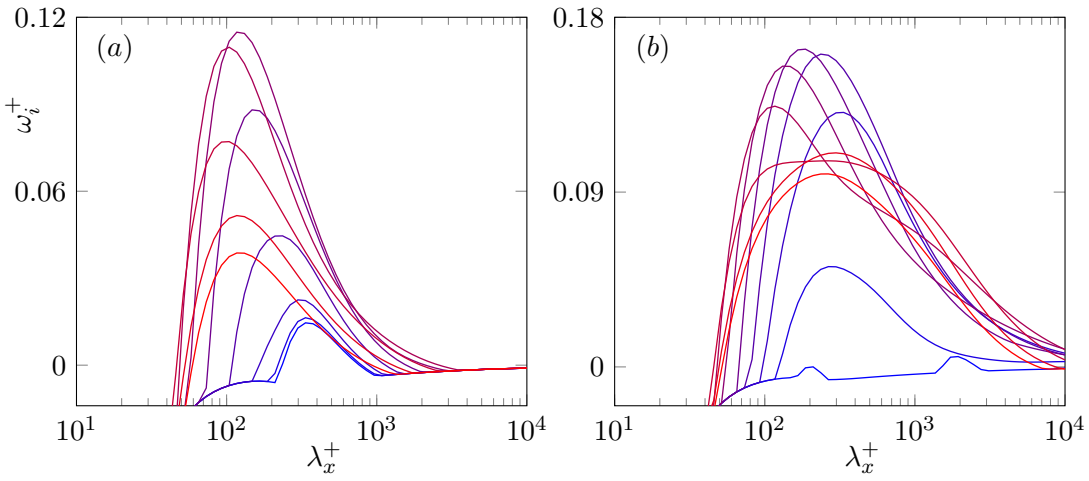

FIGURE 5.11 Growth rate, ω_i^+, as a function of the instability wavelength λ_x^+ for canopies with heights (a) $h^+ = 10$ and (b) $h^+ = 100$ for different drag coefficients. From blue to red the drag coefficient increases from $C_x^+ \approx 5 \times 10^{-5}$ to 5, with $C_x/C_y = 10^1$.

velocity. Singh *et al.* (2016) noted that their analysis predicted two instability modes, one similar to the Kelvin–Helmholtz instability and another originating from the canopy drag included in the analysis. They observed that this secondary instability mode was dominant for canopies with high drag and spanned the entire width of the channel, and its wavelength did not scale with the shear length.

The shear length within the canopy and the strength of the inflection point in the mean velocity profile is governed by the streamwise canopy drag coefficient, whereas both C_x and C_y contribute to the damping of the fluctuations. In all canopy geometries the anisotropy ratio, C_x/C_y, would be fixed by the canopy layout and the element shape. However, in order to examine the relative effect of the drag coefficients on the instability, we consider canopies with a fixed height, $h^+ = 100$ and three different scenarios for the drag on the perturbations. In the first we consider isotropic canopies with $C_x/C_y = 1$, in the second we apply no wall-normal drag on the perturbations, $C_y = 0$, and in the third, we perform analyses which apply a mean streamwise drag alone and no drag on the perturbations, $C_x = C_y = 0$. The results of the analysis with $C_x/C_y = 1$, portrayed in figure 5.14(a), are similar to those for $C_x/C_y = 10$, portrayed in figure 5.11(b) and discussed in the previous paragraph. Comparing the results of the analyses with $C_x/C_y = 1$ and $C_y = 0$, reveals that the addition of wall-normal drag causes a slight increase in the wavelength of the secondary instability discussed above and causes a reduction in the instability growth rate. When the effect of both C_x and C_y on the perturbations is neglected we do not observe the presence of the secondary instability. This is consistent with the observations of Singh *et al.* (2016), who noted that the secondary instability originated from the interaction of the canopy drag with

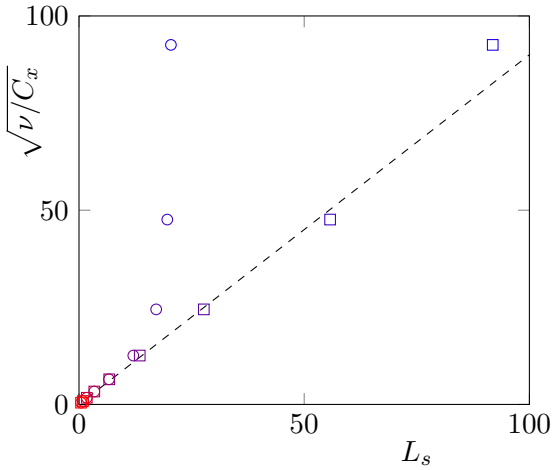

FIGURE 5.12 Drag lengthscale, $\sqrt{\nu/C_x}$, versus the shear-layer thickness within the canopy, L_s. Symbols represent ○, $h^+ = 20$; and □, $h^+ = 100$. - - -, represents the fit $\sqrt{\nu/C_x} = 0.9L_s$.

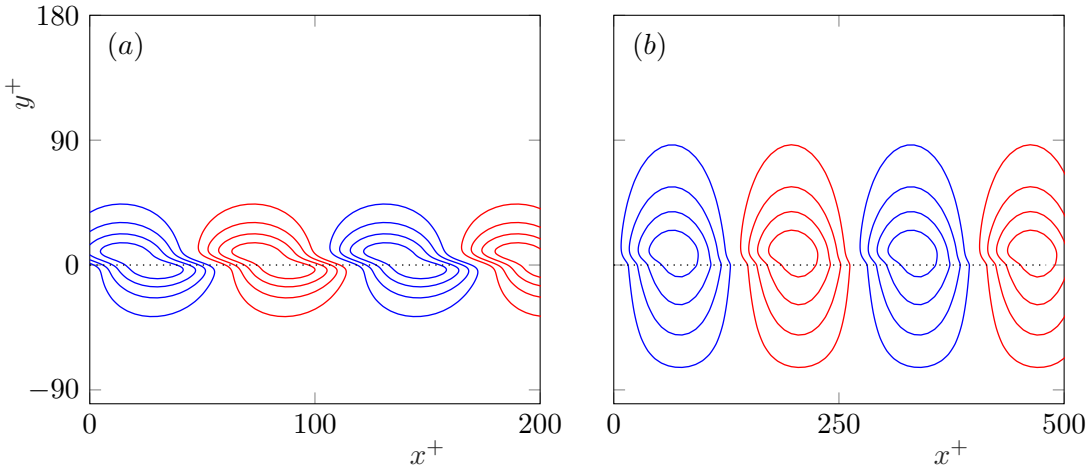

FIGURE 5.13 Contours of the stream function for the most amplified wavelength for canopy with height, $h^+ = 100$, with streamwise drag coefficients (*a*) $C_x^+ \approx 10^{-2}$ and (*b*) $C_x^+ \approx 1$. The blue and red lines correspond to clockwise and counter-clockwise rotation, respectively. The horizontal line marks the location of the canopy tips.

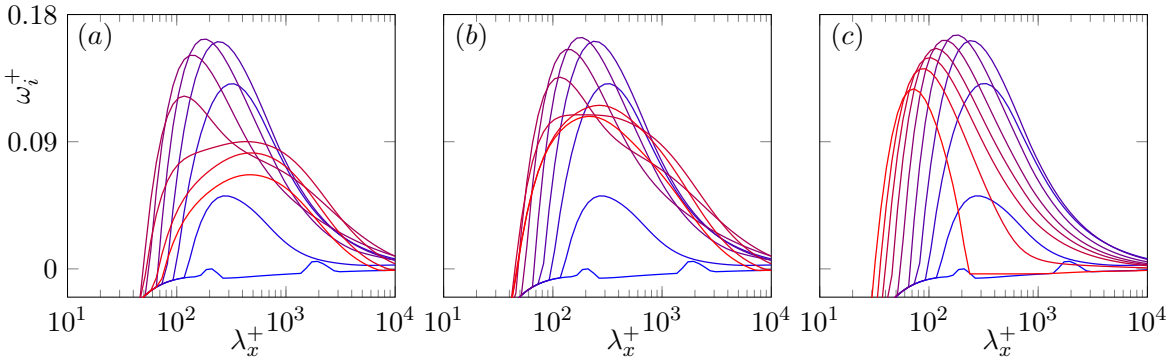

FIGURE 5.14 Growth rate, ω_i^+, as a function of the instability wavelength λ_x^+ for canopies with height, $h^+ = 100$ including the effect on the perturbations of (a) both streamwise and wall-normal drag, $C_x = C_y$; (b) streamwise drag alone, $C_y = 0$; and (c) no drag on perturbations, $C_x = C_y = 0$. From blue to red the drag coefficient increases from $C_x^+ \approx 5 \times 10^{-5}$ to 5.

the fluctuations in the overlying flow. Therefore, for the analysis with $C_x = C_y = 0$ only the Kelvin–Helmholtz-like instability mode is obtained.

The effect of increasing the canopy height on the Kelvin–Helmholtz-like and the secondary instability are also different, as can be observed in figure 5.15. For the Kelvin–Helmholtz-like instability, for a fixed canopy drag-coefficient, the growth rate of the most amplified instability asymptotes for large enough canopy heights. The wavelength of the Kelvin–Helmholtz-like instability also does not change appreciably with the canopy height as it is determined by the canopy shear-layer thickness, which remains constant for a fixed value of C_x. The amplification of the instability wavelengths of the secondary instability, however, does not show asymptotic behaviour, as shown in figure 5.15(b). The most amplified wavelength of the secondary instability also increases with the canopy height, which shows that it does not scale with the shear-layer thickness.

5.3 Comparison with DNS results

We now present the results from the stability analysis conducted using the mean profiles obtained from the DNS of dense canopy flows discussed in chapter 4. Following the results discussed in §5.2, a viscous analysis considering the molecular viscosity alone is performed using mean velocity profiles obtained from the DNSs of dense canopy flows discussed in chapter 4. In the last part of this section, we also compare how well the model described in §5.2 can capture the instabilities observed in the DNSs. Before we can conduct this analysis, however, we need to obtain the effective drag coefficients of the canopy geometries studied in chapter 4. Given the large density of the canopies considered, with maximum spacings $s^+ = \mathcal{O}(10)$, we assume that inertial effects in the flow deep within the canopy are small and can be neglected (Tanino & Nepf, 2008). In the centre of the canopy elements, away from

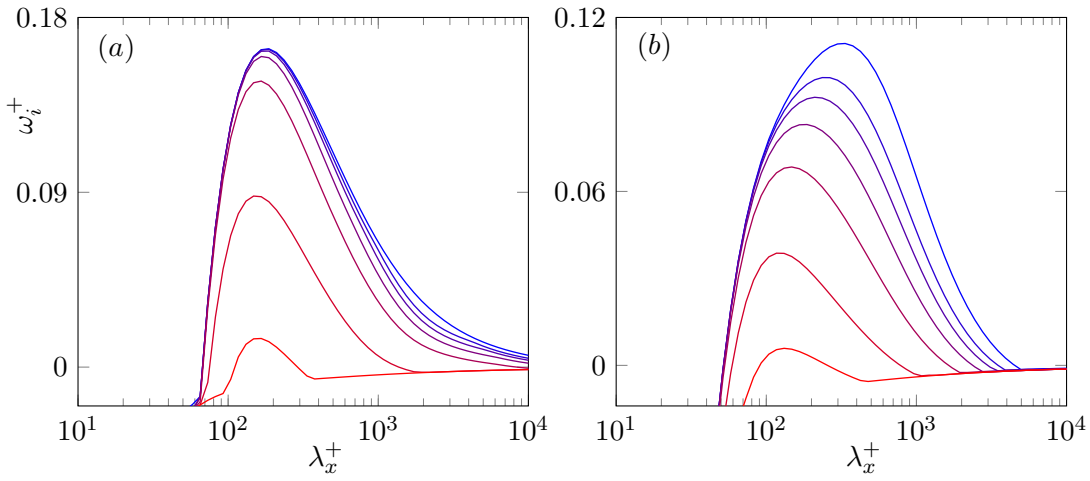

FIGURE 5.15 Growth rate, ω_i^+, as a function of the instability wavelength λ_x^+ for canopies with (a) $C_x^+ \approx 10^{-2}$ and (b) $C_x^+ \approx 1$, with $C_x/C_y = 10^1$ for different heights. The colours from red to blue represent $h^+ = 10, 20, 40, 60, 80, 100$ and 150.

the shear effects at the canopy base and top, the mean momentum equation would reduce to a balance between the canopy drag and the mean pressure gradient

$$C_x U = -\frac{\mathrm{d}P}{\mathrm{d}x}. \tag{5.31}$$

Equation (5.31) is essentially Darcy's equation for flow within permeable substrates (Darcy, 1856), and has been used by Zampogna & Bottaro (2016) to model flow deep within densely packed, rigid fibres. The streamwise drag coefficient, C_x, can be obtained by substituting the values of U and $\mathrm{d}P/\mathrm{d}x$ obtained from the DNSs into equation (5.31). From dimensional arguments, equation (5.31) predicts that the drag coefficient would scale as $C_x \sim \nu/s^2$. This scaling is demonstrated in figure 5.16(a), which suggests that equation (5.31) provides a reasonable approximation for the flow deep within the present canopies, excluding the sparsest canopy S48. Although we can expect the flow within the canopy to be Darcy-like in the wall-normal direction as well, we cannot use the DNS results to obtain C_y, as there is no mean flow in this direction. In order to obtain C_y, we consider separately the Stokes flow along infinitely long canopy elements driven by a constant pressure gradient. The equation for such flow is $(\partial_x^2 + \partial_z^2)v = \mathrm{d}P/\mathrm{d}y$. The wall-normal drag coefficient is then obtained as

$$C_y\langle v\rangle = -\frac{\mathrm{d}P}{\mathrm{d}y}, \tag{5.32}$$

where the angled brackets represent a spatial average. The estimated values of C_y are portrayed in figure 5.16(b) for reference. It may be noted that the ratio of the streamwise to wall-normal drag coefficients for the present canopies is $C_x/C_y \approx 2$–3, which shows that the streamwise flow is more obstructed than the wall-normal flow for the layouts considered.

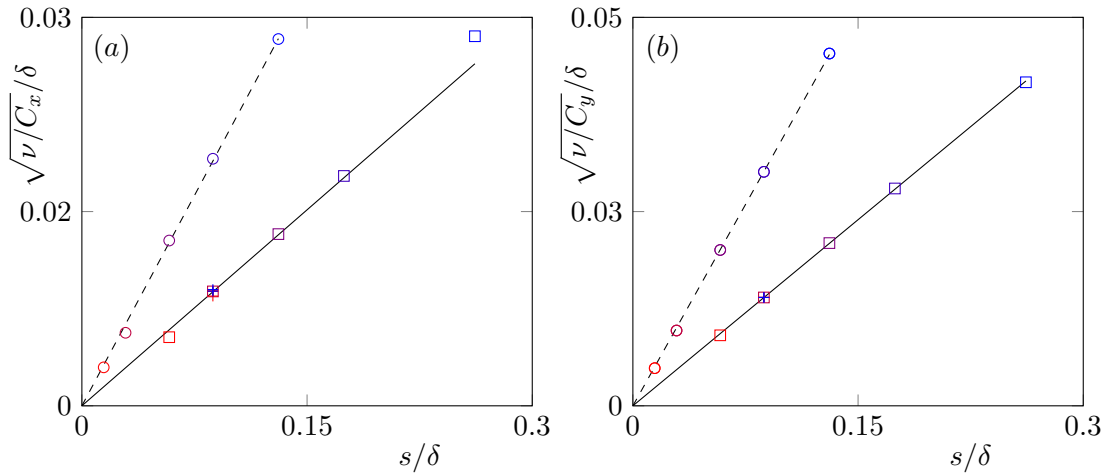

FIGURE 5.16 Variation of the lengthscales derived from the (a) streamwise and (b) wall-normal canopy drag coefficients for different element spacings. The symbols represent the cases studied in chapter 4, □, family S; +, family H; and ○, family G. The colours from red to blue represent cases S10 to S48, H16 to H128 and G10 to G100.

The most amplified wavelengths predicted by the stability analysis only match those observed in the DNSs for canopies with high values of δ/h. This can be observed in figure 5.17, where the most amplified instability wavelengths obtained from the stability analysis are superimposed on the pre-multiplied spectral energy densities of the wall-normal velocity fluctuations obtained from the DNS results, discussed in chapter 4. The growth rates for different perturbation wavelengths from the analysis including the effect of drag on them are portrayed in figures 5.18(a–c), and the wavelengths with the highest growth rates are summarised in table 5.1. The instability wavelengths predicted for cases H16, H32, G10 and G20 show reasonable agreement with the instability wavelengths observed in the DNSs. For canopies with larger heights, however, the analysis predicts wavelengths larger than those observed in the DNSs. For the fixed-spacing canopies of family H, the predicted instability wavelength also increases with increasing canopy height, whereas the DNSs show that the instability wavelength for these cases is essentially independent of the height. The contours of the instability stream function for case H96 for the most amplified wavelength, $\lambda_x^+ \approx 385$, portrayed in figure 5.19(a), show that it has a large wall-normal span, extending up to $y^+ \approx 120$. This suggests that the predicted instability is the large wavelength, secondary mode discussed in §5.2.3, which was observed for tall canopies with large drag coefficients in the stability analysis. It is assumed in the present stability analysis that the drag coefficient experienced by the perturbations is the same as that experienced by the mean flow. It is possible, however, that scales much smaller than the mean, such as those of the instability, perceive a smaller drag coefficient, as discussed in chapter 3 for sparse canopies, thus not exciting this secondary instability. The results from the analysis excluding the drag on the

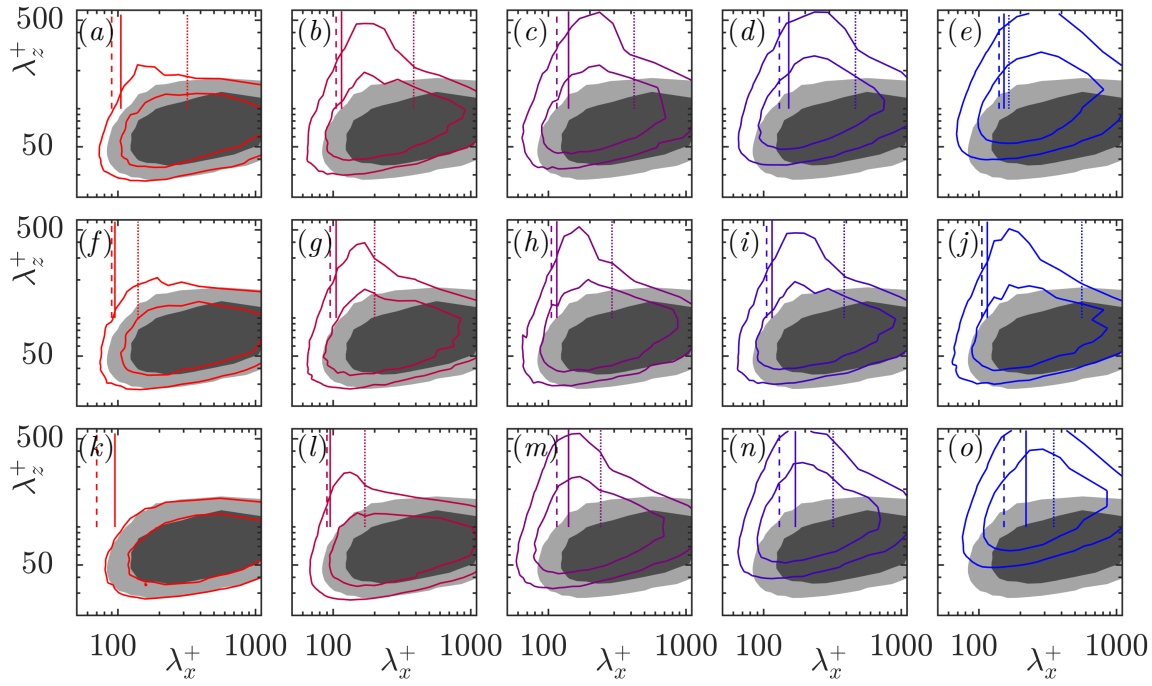

FIGURE 5.17 Pre-multiplied spectral energy densities of the wall-normal velocity, $k_x k_z E_{vv}$, at height $y^+ \approx 15$ normalised by their respective rms values from the dense canopy simulations discussed in chapter 4. The line contours represent (*a*–*e*) cases S10 to S48; (*f*–*j*) cases H16 to H128; and (*k*–*o*) cases G10 to G100. The shaded contours represent case the smooth-wall case, SC. The contours are in increments of 0.06 for all the cases. The vertical lines mark the most amplified wavelength predicted by linear stability analysis; ——, DNS mean profiles without drag on perturbations; ·····, DNS mean profiles with drag on perturbations; - - -, mean velocity profiles synthesised using equations (5.28) and (5.29), with no drag on the perturbations.

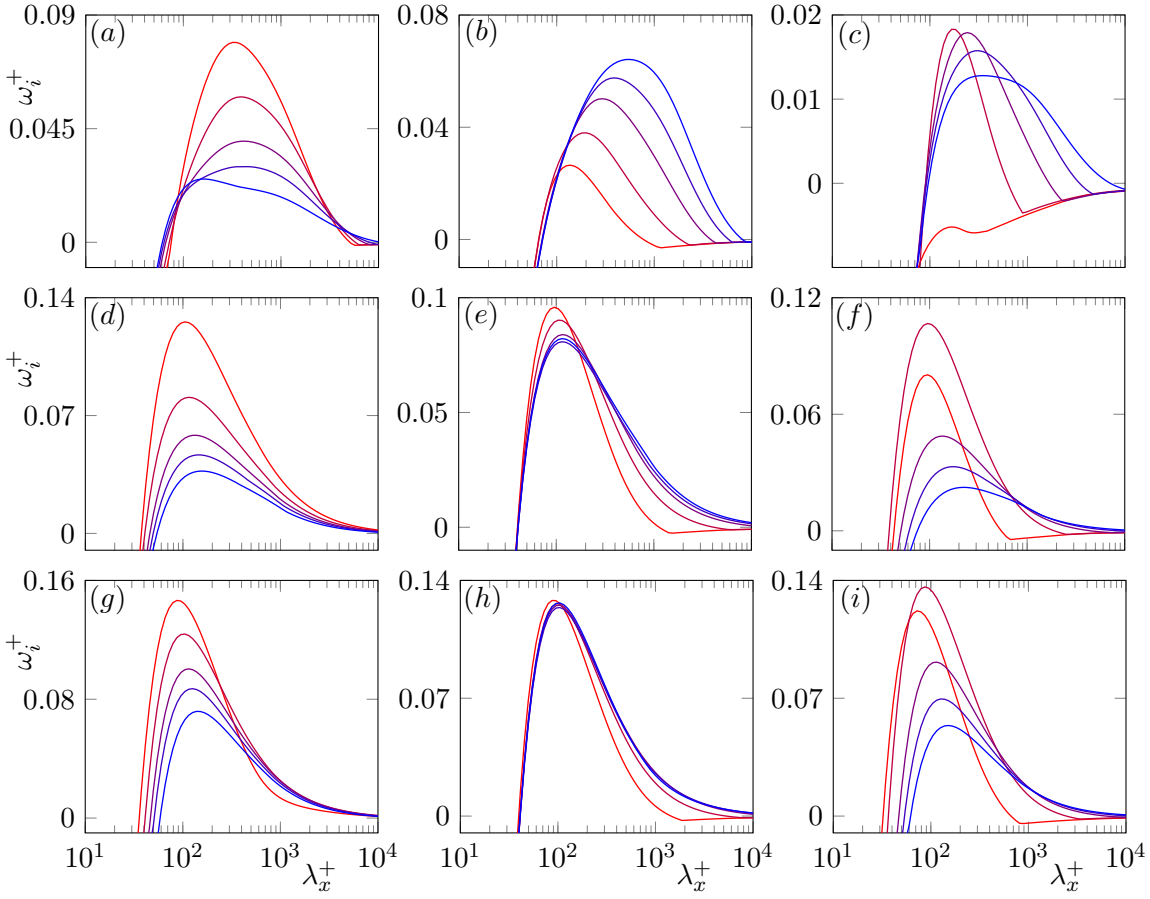

FIGURE 5.18 Growth rates of different perturbation wavelengths obtained from the stability analysis performed on (*a*–*c*) mean profiles obtained from the DNSs, with drag on the perturbations included in the stability analysis; (*d*–*f*) mean profiles obtained from DNSs, with no drag on the perturbations; and (*g*–*i*) mean velocity profiles synthesised using equations (5.28) and (5.29), with no drag on the perturbations. The lines from red to blue represent (*a*,*d*,*g*) cases S10 to S48; (*b*,*e*,*h*) cases H16 to H128; and (*c*,*f*,*i*) cases G10 to G100.

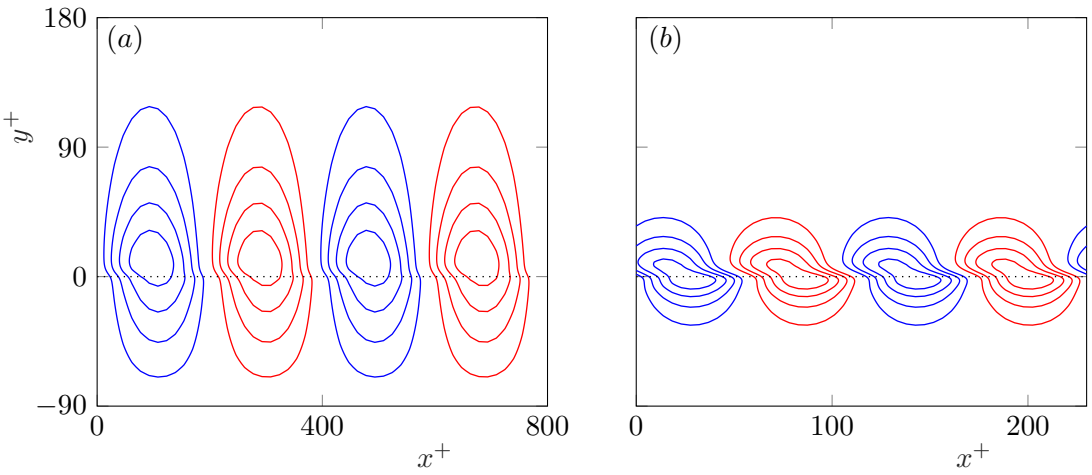

FIGURE 5.19 Contours of the stream function for the most amplified instability for case H96 obtained from the stability analysis (a) with drag and (b) without drag on the perturbations.

perturbations, which would recover the Kelvin–Helmholtz-like instability mode, are portrayed in figure 5.18(d–f) and yield better estimates for the instability wavelengths observed in the DNSs, as shown in figure 5.17. For the canopies of family H, the stability analysis without drag on the fluctuations shows that the most amplified wavelength does not vary significantly with the canopy height, as shown in figure 5.18(e). For the canopies of families S and G, this analysis shows an increase in the most amplified wavelength with increasing element spacing, as can be observed in figures 5.18(d) and (f), owing to the increase in the shear-layer thickness. While neglecting the drag acting on the fluctuations yields better estimates for the most amplified wavelengths for canopies with small spacings, the predictions for larger spacings differ by up to a factor of two from the DNS observations. This is likely due to the assumption that the mean flow is homogeneous in the tangential directions, implicit in the stability analysis, which breaks down for such cases. There may also be some distortion of the instability by the ambient turbulent fluctuations in the DNSs (Rogers & Moser, 1994; Raupach *et al.*, 1996; Finnigan *et al.*, 2009; Bailey & Stoll, 2013).

The stability analysis also indicates that the observed instability scales in friction units, as discussed in §4.1.1. Consistent with the observations in the DNSs, the linear stability analysis for cases $\mathrm{H32}_{180}$ and $\mathrm{H32}_{400}$ also predicts similar instability wavelengths and growth rates in friction units, as shown in figure 5.20.

The results obtained from the DNSs and the stability analysis suggest that there is a dependence on the element spacing of the most amplified wavelength, related to the effect of the spacing on the shear-layer thickness. As discussed previously, the full shear layer thickness of the canopy will be the sum of the contributions within and outside the canopy region. The shear-layer thickness within the canopy is defined as $L_s = U/(\mathrm{d}U/\mathrm{d}y)$, as discussed in the previous section. We observe that even in the DNS mean profiles, the shear-layer thickness

	Case	DNS	SA_{C0}	SAM_{C0}	SA
Fixed height	S10	140	105	90	320
	S16(H96)	160	115	105	385
	S24	200	140	115	420
	S32	230	152	130	465
	S48	250	152	140	165
Fixed spacing	H16	130	95	90	140
	H32	150	105	95	200
	H64	160	115	105	290
	H96(S16)	160	115	105	385
	H128	160	115	105	560
Self-similar geometry	G10	–	95	70	–
	G20	120	95	90	170
	G40	140	140	115	240
	G60	190	170	130	320
	G100	260	220	152	350
Varying Re_τ	$H32_{180}$	140	105	–	180
	$H32_{400}$	140	105	–	180

Table 5.1 Most amplified instability wavelengths observed in the DNSs and predicted by the stability analysis, scaled in friction units. The column labelled 'DNS' lists the approximate streamwise wavelength associated with the instability in the wall-normal spectra portrayed in figure 5.17. SA_{C0}, most amplified wavelengths from stability analysis on DNS mean profiles without drag on fluctuations; SAM_{C0}, mean velocity profiles synthesised using equations (5.28) and (5.29), with no drag on the perturbations.; and SA, on DNS mean profiles with drag on fluctuations

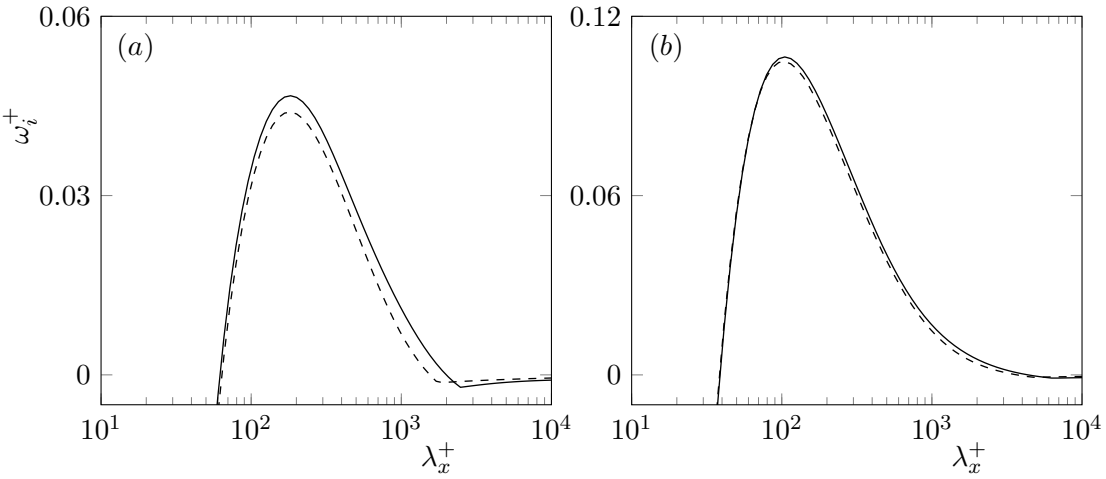

FIGURE 5.20 Growth rate of different perturbation wavelengths from the stability analysis of cases $\mathrm{H32}_{180}$ (solid lines) and $\mathrm{H32}_{400}$ (dashed lines). (a) portrays results from the stability analysis with drag and (b) without drag on the perturbations.

outside the canopy appears to be $y_c^+ \approx 5$. This is illustrated in figure 5.21(a), which shows that the instability wavelengths predicted by the stability analysis correlate well with the full shear length $L_s + y_c$, taking $y_c^+ = 5$. This suggests that the shear-layer semi-thickness above the canopies is roughly constant for most of the geometries considered here, and remains close to the smooth-wall value. The only notable deviation is for the sparsest canopy studied, S48. For canopies with large element spacings, we observe that the peak in $\mathrm{d}^2U/\mathrm{d}y^2$ moves closer to the canopy-tip plane, so $y_c^+ = 5$ may no longer be a reasonable approximation for the shear-layer semi-thickness above. We observe that the height of the shear layer within the canopy, L_s, is set by the mean canopy drag coefficient, $L_s \propto \sqrt{\nu/C_x}$, which in turn depends mainly on the element spacing, as shown in figures 5.21(b) and (c). The correlation of L_s with s, therefore, explains the dependence of the most amplified wavelength on the element spacing observed in the DNS results and the stability analysis.

5.3.1 Analysis on modelled velocity profiles

In this section, we examine how well the stability analysis conducted on these modelled velocity profiles obtained using equations (5.28) and (5.29), compare to the analysis of the DNS profiles. The effective streamwise drag coefficient used to model the velocity profiles are the ones obtained using equation (5.31) and are portrayed in figure 5.16(a). The most amplified wavelengths predicted by the stability analysis conducted on the modelled velocity profiles, with no drag on the fluctuations, are in reasonable agreement with those conducted on profiles obtained from the DNSs. The growth rates predicted are portrayed in figures 5.18$(g$–$i)$. The wavelengths with maximum growth rates are also summarised in table 5.1. It is worth noting that even though this model is able to capture the instability wavelength, the velocity

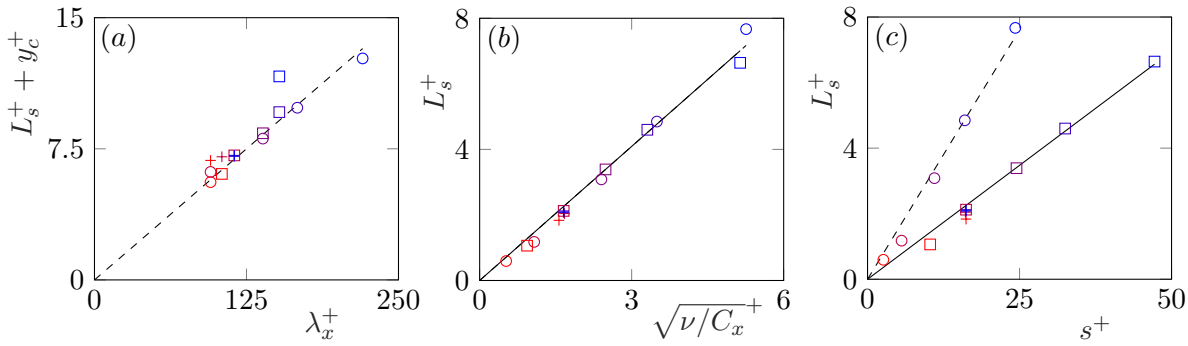

FIGURE 5.21 Relations between (a) the instability wavelength, λ_x^+, obtained from the linear stability analysis and the total shear length, $L_s + y_c$; (b) the shear length and the drag lengthscale; and (c) the shear length and the element spacing. The symbols represent □, cases of S; +, cases of H; and ○, cases of G.

profiles obtained using this model do not match those from the DNSs, apart from those of S10 and G10. This is most likely due to our assumption that the turbulent stresses do not penetrate within the canopy, which fails as the element spacing is increased. As discussed previously, the wavelength of the instability is set by the shear length. The shear length within the canopy, L_s, is set by the canopy drag coefficient, C_x. As this drag coefficient is the same both from the DNSs and for the modelled velocity profiles, we expect L_s to be similar as well. The shear length above the canopy, however, may differ, as the profiles from the DNSs include the effect of the turbulent stresses penetrating into the canopy and deviating from their smooth-wall values, while the modelled velocity profiles do not. The similarity in the instability wavelengths between these analyses, therefore, suggest that, for the dense canopies considered in this work, turbulence is essentially precluded from penetrating within the canopy and the shear length above does not seem to vary significantly from its smooth-wall value.

Chapter 6

Conclusions and future work

In this thesis, we have investigated turbulent flows over canopies using direct numerical simulation. A wide range of canopy parameters have been considered for canopies in both the sparse and dense regimes.

The sparse canopies studied had element spacings larger than the characteristic scales of near-wall turbulence structures, such as streaks, $s^+ \gtrsim 100$, in addition to having low frontal area densities, $\lambda_f \lesssim 0.1$. The key idea was that such canopies would allow the near-wall turbulence to 'live' within the canopy, relatively unhindered by the canopy elements. These canopies were therefore sparse from the point of view of near-wall turbulence as well. Two different canopy element geometries have been studied, each for different element spacings. We have also compared canopies with permeable and impermeable elements in the same arrangement. The flow was decomposed into an element-induced component and a background-turbulence component. It was found that, although the element-induced flow in the permeable and impermeable canopies studied here differ in intensity, the background turbulence was essentially the same. A new scaling for the background turbulence within sparse canopies was proposed. This scaling uses the friction velocity based on the local sum of the viscous and Reynolds shear stresses, τ_f, at each height, rather than the conventional friction velocity, based on the total stress. When scaled with the proposed local friction velocity, the background-turbulence fluctuations and the viscous and Reynolds shear stresses appear more smooth-wall-like, compared to when conventional, total-stress scaling is used. This suggests that the sparse canopy acts in large part on the background turbulence through a change in the local scale, rather than through a direct interaction with the canopy elements. Based on the proposed scaling, we investigated the extent to which a drag force acting only on the mean flow captured the effect of the canopy on the background turbulence. The mean-only drag directly modifies the mean flow alone, which in turn sets τ_f and, hence, the scale for the fluctuations. We show that the mean-only drag is able to capture the background-turbulence fluctuations within the canopies better than a conventional homogeneous drag. Neither approach is, however, sufficient to capture the element-induced flow. We have shown that the

element-induced flow can be partially recovered by redistributing the mean-only drag in a low-order representation of the canopy. While this low-order representation can capture the element-induced velocity fluctuations of the permeable canopy, it still cannot fully capture the deficit of the element-induced Reynolds shear stresses and, consequently, the mean-velocity profile of the resolved canopy simulations. In future work, it would be worth exploring more sophisticated models to capture this deficit. In the present work, the low-order canopy representation only acts on the canopy scales and its harmonics, and cannot capture the effect of the canopy on larger scales in the flow. The present model could be extended also to apply a force on these large scales to account for this interaction.

We have also examined flows over dense canopies. We have studied the effect of the canopy parameters on velocity fluctuations within and above the canopy. Three families of simulations have been conducted. The first with the element height in friction units fixed, the second with the element spacing fixed, and the third with the height-to-spacing ratio fixed. The layouts considered had height-to-spacing ratios greater than one, and elements spacings ranging from $s^+ \approx 2.6$ to 48. We have observed that the height of the roughness sublayer in such canopies was set by the element spacing, and not their height, and extends to approximately two to three times the element spacing. The intensity of the velocity fluctuations within the canopy was also found to be determined by the element spacing. We observed that the element-induced fluctuations were essentially the same for canopies with the same element spacing regardless of their height and increased in magnitude with the spacing. As the element spacing increased, so did the peak intensity of the wall-normal and spanwise velocity fluctuations and the Reynolds shear stresses above the canopy. The peak in the streamwise velocity fluctuations, in turn, decreased with increasing element spacing. These changes were attributed to the modification of the near-wall turbulence through its interaction with the canopy elements, and to the growth of a Kelvin–Helmholtz-like instability at the top of the canopy. At a fixed element spacing, the effect of increasing the height of the canopy was found to asymptote at a height-to-spacing ratio $h/s \approx 6$. While increasing the canopy height at a fixed spacing did not have a significant effect on the element-induced flow, it promoted the formation of the Kelvin–Helmholtz-like instability, which in turn affected the turbulence fluctuations within and above the canopy. Canopies with very small element spacings, $s^+ \lesssim 10$, also inhibited the instability owing to the large drag they exert on the fluctuations and a stronger footprint of the instability could be observed over canopies with larger spacings. We found that the velocity fluctuations deep within the canopy resulted largely from spanwise-coherent scales, suggesting that they originate from the overlying instability as well. In the present work, we have only considered the effect of rigid filaments in the flow. Recently, Sundin & Bagheri (2019) have also performed fully-coupled simulations of turbulent flows over flexible filaments, although they did not find evidence that Kelvin–Helmholtz-like instabilities were dominant in the flow. Now that we have a better understanding of the canopy parameters that can elicit this instability, it

would be interesting to simulate flexible filaments in these regimes. If we could obtain lock-in between the instability and the element-waving frequencies it may be of interest for designing canopies for energy harvesting. Another avenue to extend this research would be to evaluate the effect of these canopies and the associated instabilities on convective heat transfer. The recent study of MacDonald *et al.* (2019) has shown that the increase of heat-transfer caused by rough surfaces asymptotes with the roughness size. It may be possible to enhance the mixing and the heat transfer by employing canopy-like obstacles which allow the formation of Kelvin–Helmholtz-like instabilities.

In the final part of the thesis, we have presented the results from models based on linear stability analysis to characterise the Kelvin–Helmholtz-like instability over dense canopies. We have modelled the flow within the canopies using two methods, the first by analogy to a permeable substrate, and the second as a drag force in the momentum equations. In both models, we have assumed that the canopy was dense enough to preclude the penetration of turbulent eddies within them. In the permeable substrate model, the flow within the canopy was assumed to be governed by the Brinkman equation, and the canopies were parametrised by their permeabilities in the streamwise and wall-normal directions, K_x and K_y, and their height, h. This equation was solved analytically, and the solution was used to provide boundary conditions for the flow above the canopy. We found that the resulting instability over the substrates scaled in friction units, where the friction velocity was measured at the interface between the canopy and the free-flow. For permeability ratios relevant for canopy flows, $K_x/K_y < 1$ and with large heights, the instability depended equally on both the permeabilities and was governed by the parameter $\sqrt{K_x^+ K_y^+}$. The model was also used to show that the mean bending of the canopy elements up to angles of 30° did not have a significant effect on the instability. This model, however, tended to under-predict the wavelength of the instability compared to those observed in the DNSs, and also did not provide an accurate representation of the instabilities for canopies with very high permeabilities. These drawbacks resulted from the fact that the permeable substrate model did not utilise the information about the mean-flow within the canopy elements, which sets the shear-layer thickness that determines the instability wavelength, and the strength of the inflection point, which determines its amplification. The drag-force model, which represented the effect of the canopy as a homogeneous drag force, overcame some of these shortcomings by providing an estimate for the mean flow within the canopy. This analysis also predicted that the shear-layer instability over canopies scaled in friction units, measured at the canopy tip-plane, similar to the permeable-substrate model. The height of the shear layer within the canopy, L_s, is determined by the limiting value between the canopy drag lengthscale, $\sqrt{\nu/C_x}$, and the canopy height, h. This analysis predicted the increase in L_s and, consequently, the instability wavelength as the canopy was made sparser. The analysis also showed that the amplification of the instability was governed by two competing effects arising from the canopy drag. A large drag resulted in a stronger inflection point, which enhanced the instability,

while also inhibiting the fluctuations within the canopy, which suppressed it. The results showed the presence of an optimum drag-coefficient for which the most amplified instabilities could be obtained. For very tall canopies with large drag coefficients, the presence of a large-wavelength, secondary instability that did not scale with L_s was observed. We also extended this analysis to the velocity profiles obtained from the DNSs of dense canopy flows. We found that while the stability analysis predicted the presence of the aforementioned secondary instabilities for several of the dense canopies studied, they were not observed in the DNSs. For these canopies, the stability analysis without any drag on the perturbations provided a better approximation of the instability wavelength. The predicted instability wavelength was shown to scale with the full shear-layer thickness, which included the part of the shear layer within the canopy, L_s, and that outside, y_c. The latter was found to be roughly constant for the dense canopies studied, $y_c^+ \approx 5$, and was likely determined by the location at which the vorticity gradient peaks above the canopy-tip plane, as proposed by García-Mayoral & Jiménez (2011). The shear length within the canopy, L_s, was still set by $\sqrt{\nu/C_x}$ which, in turn, was observed to scale with the element spacing. This analysis was able to capture many features of the instability observed in the DNSs, such as the invariance of the instability wavelength to an increase in canopy height, and its increase with increasing canopy spacing. The analysis still fails for large element spacings, for which the assumption of the flow perceiving the canopy in a homogenised fashion would break down. The stability analysis conducted using the velocity profiles from the proposed drag model yielded similar results to those conducted using the mean profiles obtained from the DNSs. This study provided an *a priori* method to relate the canopy parameters to the characteristics of the Kelvin–Helmholtz-like instability. The proposed models could be used to inform the design of engineered canopies to enhance heat transfer or energy harvesting, which may conceivably benefit from the presence of the instability.

References

Abderrahaman-Elena, N. 2018 Near-wall turbulence in the transitionally rough regime. PhD thesis, Department of Engineering, University of Cambridge.

Abderrahaman-Elena, N., Fairhall, C. T. & García-Mayoral, R. 2019 Modulation of near-wall turbulence in the transitionally rough regime. *Journal of Fluid Mechanics* **865**, 1042–1071.

Abderrahaman-Elena, N. & García-Mayoral, R. 2017 Analysis of anisotropically permeable surfaces for turbulent drag reduction. *Physical Review Fluids* **2** (11), 114609.

Ackerman, J. D. & Okubo, A. 1993 Reduced mixing in a marine macrophyte canopy. *Functional Ecology* pp. 305–309.

Auriault, J. 2009 On the domain of validity of Brinkman's equation. *Transport in porous media* **79** (2), 215–223.

Bai, K., Katz, J. & Meneveau, C. 2015 Turbulent flow structure inside a canopy with complex multi-scale elements. *Boundary-Layer Meteorology* **155** (3), 435–457.

Bailey, B. N. & Stoll, R. 2013 Turbulence in sparse, organized vegetative canopies: A large-eddy simulation study. *Boundary-Layer Meteorology* **147** (3), 369–400.

Bailey, B. N. & Stoll, R. 2016 The creation and evolution of coherent structures in plant canopy flows and their role in turbulent transport. *Journal of Fluid Mechanics* **789**, 425–460.

Balachandar, S., Mittal, R. & Najjar, F. M. 1997 Properties of the mean recirculation region in the wakes of two-dimensional bluff bodies. *Journal of Fluid Mechanics* **351**, 167–199.

Baldocchi, D., Falge, E., Gu, L., Olson, R., Hollinger, D., Running, S., Anthoni, P., Bernhofer, C., Davis, K., Evans, R. & others 2001 FLUXNET: A new tool to study the temporal and spatial variability of ecosystem-scale carbon dioxide, water vapor, and energy flux densities. *Bulletin of the American Meteorological Society* **82** (11), 2415–2434.

Barlow, J. & Coceal, O. 2008 A review of urban roughness sublayer turbulence. Report. U. K. Met Office.

Battiato, I. 2012 Self-similarity in coupled Brinkman/Navier–Stokes flows. *Journal of Fluid Mechanics* **699**, 94–114.

Bejan, A. & Morega, A. M. 1993 Optimal arrays of pin fins and plate fins in laminar forced convection. *Journal of Heat Transfer* **115** (1), 75–81.

Belcher, S. E., Harman, I. N. & Finnigan, J. J. 2012 The wind in the willows: flows in forest canopies in complex terrain. *Annual Review of Fluid Mechanics* **44**, 479–504.

Beneddine, S., Sipp, D., Arnault, A., Dandois, J. & Lesshafft, L. 2016 Conditions for validity of mean flow stability analysis. *Journal of Fluid Mechanics* **798**, 485–504.

Blackwelder, R. F. & Eckelmann, H. 1979 Streamwise vortices associated with the bursting phenomenon. *Journal of Fluid Mechanics* **94** (3), 577–594.

Böhm, M., Finnigan, J. J., Raupach, M. R. & Hughes, D. 2013 Turbulence structure within and above a canopy of bluff elements. *Boundary-layer Meteorology* **146** (3), 393–419.

Brinkman, H. C. 1949 A calculation of the viscous force exerted by a flowing fluid on a dense swarm of particles. *Flow, Turbulence and Combustion* **1** (1), 27.

Brown, G. L. & Roshko, A. 1974 On density effects and large structure in turbulent mixing layers. *Journal of Fluid Mechanics* **64** (4), 775–816.

Busse, A. & Sandham, N. D. 2012 Parametric forcing approach to rough-wall turbulent channel flow. *Journal of Fluid Mechanics* **712**, 169–202.

Canuto, C., Hussaini, M. Y., Quarteroni, A., Thomas Jr, A. & others 2012 *Spectral methods in fluid dynamics*. Springer Science & Business Media.

Cess, R. D. 1958 A survey of the literature on heat transfer in turbulent tube flow. Report 8-0529-r24. Westinghouse Research.

Chan, L., MacDonald, M., Chung, D., Hutchins, N. & Ooi, A. 2015 A systematic investigation of roughness height and wavelength in turbulent pipe flow in the transitionally rough regime. *Journal of Fluid Mechanics* **771**, 743–777.

Coceal, O., Dobre, A., Thomas, T. G. & Belcher, S. E. 2007 Structure of turbulent flow over regular arrays of cubical roughness. *Journal of Fluid Mechanics* **589**, 375–409.

Coceal, O., Thomas, T. & Belcher, S. 2008 Spatially-averaged flow statistics within a canopy of large bluff bodies: Results from direct numerical simulations. *Acta Geophysica* **56** (3), 862–875.

Coceal, O., Thomas, T. G., Castro, I. P. & Belcher, S. E. 2006 Mean flow and turbulence statistics over groups of urban-like cubical obstacles. *Boundary-Layer Meteorology* **121** (3), 491–519.

Cooley, J. W. & Tukey, J. W. 1965 An algorithm for the machine calculation of complex fourier series. *Mathematics of computation* **19** (90), 297–301.

Darcy, H. P. G. 1856 *Les Fontaines publiques de la ville de Dijon. Exposition et application des principes à suivre et des formules à employer dans les questions de distribution d'eau, etc.* V. Dalamont.

Diener, J., Reveret, L. & Fiume, E. 2006 Hierarchical retargetting of 2D motion fields to the animation of 3D plant models. In *Proceedings of the 2006 ACM SIGGRAPH/Eurographics symposium on Computer animation*, pp. 187–195. Eurographics Association.

Drazin, P. G. & Reid, W. H. 1998 *Hydrodynamic stability*. Cambridge University Press (1981 and 2004).

Dupont, S. & Brunet, Y. 2008 Influence of foliar density profile on canopy flow: A large-eddy simulation study. *Agricultural and Forest Meteorology* **148** (6-7), 976–990.

Dupont, S., Gosselin, F., Py, C., De Langre, E., Hemon, P. & Brunet, Y. 2010 Modelling waving crops using large-eddy simulation: comparison with experiments and a linear stability analysis. *Journal of Fluid Mechanics* **652**, 5–44.

Fairhall, C. T. 2018 The influence of superhydrophobic surfaces on near-wall turbulence. PhD thesis, Department of Engineering, University of Cambridge.

Fairhall, C. T., Abderrahaman-Elena, N. & García-Mayoral, R. 2019 The effect of slip and surface texture on turbulence over superhydrophobic surfaces. *Journal of Fluid Mechanics* **861**, 88–118.

Fairhall, C. T. & García-Mayoral, R. 2018 Spectral analysis of the slip-length model for turbulence over textured superhydrophobic surfaces. *Flow, Turbulence and Combustion* **100** (4), 961–978.

Ferziger, J. H. & Peric, M. 2012 *Computational methods for fluid dynamics*. Springer Science & Business Media.

Finnigan, J. J. 2000 Turbulence in plant canopies. *Annual Review of Fluid Mechanics* **32** (1), 519–571.

Finnigan, J. J. & Mulhearn, P. J. 1978 Modelling waving crops in a wind tunnel. *Boundary-Layer Meteorology* **14** (2), 253–277.

Finnigan, J. J., Shaw, R. H. & Patton, E. G. 2009 Turbulence structure above a vegetation canopy. *Journal of Fluid Mechanics* **637**, 387–424.

Flack, K. A., Schultz, M. P. & Connelly, J. S. 2007 Examination of a critical roughness height for outer layer similarity. *Physics of Fluids* **19** (9), 095104.

Flores, O. & Jiménez, J. 2006 Effect of wall-boundary disturbances on turbulent channel flows. *Journal of Fluid Mechanics* **566**, 357–376.

García-Mayoral, R 2011 The interaction of riblets with wall-bounded turbulence. PhD thesis, Universidad Politécnica de Madrid, Madrid.

García-Mayoral, R., Gómez-de-Segura, G. & Fairhall, C. T. 2019 The control of near-wall turbulence through surface texturing. *Fluid Dynamics Research* **51** (1), 011410.

García-Mayoral, R. & Jiménez, J. 2011 Hydrodynamic stability and breakdown of the viscous regime over riblets. *Journal of Fluid Mechanics* **678**, 317–347.

García-Mayoral, R. & Jiménez, J. 2012 Scaling of turbulent structures in riblet channels up to $\mathrm{Re}_\tau \approx 550$. *Physics of Fluids* **24** (10), 105101.

Ghisalberti, M. & Nepf, H. M. 2002 Mixing layers and coherent structures in vegetated aquatic flows. *Journal of Geophysical Research: Oceans* **107** (C2), 3–1.

Ghisalberti, M. & Nepf, H. M. 2004 The limited growth of vegetated shear layers. *Water Resources Research* **40** (7).

Giometto, M. G., Christen, A., Meneveau, C., Fang, J., Krafczyk, M. & Parlange, M. B. 2016 Spatial characteristics of roughness sublayer mean flow and turbulence over a realistic urban surface. *Boundary-layer meteorology* **160** (3), 425–452.

Gómez-de-Segura, G. 2019 Turbulent drag reduction by anisotropic permeable substrates. PhD thesis, Department of Engineering, University of Cambridge.

Gómez-de-Segura, G. & García-Mayoral, R. 2019 Turbulent drag reduction by anisotropic permeable substrates − analysis and direct numerical simulations. *arXiv preprint arXiv:1902.08554* .

Gómez-de-Segura, G., Sharma, A. & García-Mayoral, R. 2018*a* Turbulent drag reduction using anisotropic permeable substrates. *Flow, Turbulence and Combustion* **100** (4), 995–1014.

Gómez-de-Segura, G., Sharma, A. & García-Mayoral, R. 2018*b* Virtual origins in turbulent flows over complex surfaces. In *Proceedings of the 2018 Summer Program*. Center for Turbulence Research, Stanford University.

Gosselin, F. & De Langre, E. 2009 Destabilising effects of plant flexibility in air and aquatic vegetation canopy flows. *European Journal of Mechanics-B/Fluids* **28(2)**, 271–282.

Grimmond, C. S. B. & Oke, T. R. 1999 Aerodynamic properties of urban areas derived from analysis of surface form. *Journal of applied meteorology* **38** (9), 1262–1292.

Hama, F. R. 1954 Boundary layer characteristics for smooth and rough surfaces. *Transactions of the Society of Naval Architects and Marine Engineers* **62**, 333–358.

Harman, I. N., Böhm, M., Finnigan, J. J. & Hughes, D. 2016 Spatial variability of the flow and turbulence within a model canopy. *Boundary-layer meteorology* **160** (3), 375–396.

Healey, J. J. 2009 Destabilizing effects of confinement on homogeneous mixing layers. *Journal of Fluid Mechanics* **623**, 241–271.

Högström, U., Bergström, H. & Alexandersson, H. 1982 Turbulence characteristics in a near neutrally stratified urban atmosphere. *Boundary-Layer Meteorology* **23** (4), 449–472.

Huang, J., Cassiani, M. & Albertson, J. D. 2009 The effects of vegetation density on coherent turbulent structures within the canopy sublayer: A large-eddy simulation study. *Boundary-layer Meteorology* **133** (2), 253–275.

Huerre, P. 1983 Finite amplitude evolution of mixing layers in the presence of solid boundaries. *Journal de Mecanique Theorique et Appliquee Supplement* pp. 121–145.

Ikeda, S. & Kanazawa, M. 1996 Three-dimensional organized vortices above flexible water plants. *Journal of Hydraulic Engineering* **122** (11), 634–640.

Inoue, E. 1955 Studies of the phenomena of waving plants ("honami") caused by wind. *Journal of Agricultural Meteorology* **11** (3), 87–90.

Jackson, P. S. 1981 On the displacement height in the logarithmic velocity profile. *Journal of fluid mechanics* **111**, 15–25.

Jeong, J., Hussain, F., Schoppa, W. & Kim, J. 1997 Coherent structures near the wall in a turbulent channel flow. *Journal of Fluid Mechanics* **332**, 185–214.

Jiménez, J. 2004 Turbulent flows over rough walls. *Annual Review of Fluid Mechanics* **36**, 173–196.

Jiménez, J. 2013 Near-wall turbulence. *Physics of Fluids* **25** (10), 101302.

Jiménez, J. 2018 Coherent structures in wall-bounded turbulence. *Journal of Fluid Mechanics* **842**.

Jiménez, J. & Moin, P. 1991 The minimal flow unit in near-wall turbulence. *Journal of Fluid Mechanics* **225**, 213–240.

Jiménez, J. & Pinelli, A. 1999 The autonomous cycle of near-wall turbulence. *Journal of Fluid Mechanics* **389**, 335–359.

Jimenez, J., Uhlmann, M., Pinelli, A. & Kawahara, G. 2001 Turbulent shear flow over active and passive porous surfaces. *Journal of Fluid Mechanics* **442**, 89–117.

Kim, J. & Moin, P. 1985 Application of a fractional-step method to incompressible navier-stokes equations. *Journal of computational physics* **59** (2), 308–323.

Kline, S. J., Reynolds, W. C., Schraub, F. A. & Runstadler, P. W. 1967 The structure of turbulent boundary layers. *Journal of Fluid Mechanics* **30** (4), 741–773.

Kuwata, Y. & Suga, K. 2016 Lattice boltzmann direct numerical simulation of interface turbulence over porous and rough walls. *International Journal of Heat and Fluid Flow* **61**, 145–157.

de Langre, E. 2008 Effects of Wind on Plants. *Annual Review of Fluid Mechanics* **40** (1), 141–168.

Le, H. & Moin, P. 1991 An improvement of fractional step methods for the incompressible navier-stokes equations. *Journal of Computational Physics* **92** (2), 369–379.

Ledda, P. G., Siconolfi, L., Viola, F., Gallaire, F. & Camarri, S. 2018 Suppression of von Kármán vortex streets past porous rectangular cylinders. *Physical Review Fluids* **3**, 103901.

Leonardi, S. & Castro, I. P. 2010 Channel flow over large cube roughness: a direct numerical simulation study. *Journal of Fluid Mechanics* **651** (1999), 519.

Lévy, T. 1983 Fluid flow through an array of fixed particles. *International Journal of Engineering Science* **21** (1), 11–23.

Ligrani, P. M. & Moffat, R. J. 1986 Structure of transitionally rough and fully rough turbulent boundary layers. *Journal of Fluid Mechanics* **162**, 69–98.

Lozano-Durán, A. & Jiménez, J. 2014 Effect of the computational domain on direct simulations of turbulent channels up to Re_τ= 4200. *Physics of Fluids* **26** (1), 011702.

Luhar, M. & Nepf, H. M. 2013 From the blade scale to the reach scale: A characterization of aquatic vegetative drag. *Advances in Water Resources* **51**, 305–316.

Luhar, M., Rominger, J. & Nepf, H. 2008 Interaction between flow, transport and vegetation spatial structure. *Environmental Fluid Mechanics* **8** (5-6), 423.

Luminari, N., Airiau, C. & Bottaro, A. 2016 Drag-model sensitivity of Kelvin–Helmholtz waves in canopy flows. *Physics of Fluids* **28** (12), 124103.

MacDonald, M., Hutchins, N. & Chung, D. 2019 Roughness effects in turbulent forced convection. *Journal of Fluid Mechanics* **861**, 138–162.

MacDonald, M., Ooi, A., García-Mayoral, R., Hutchins, N. & Chung, D. 2018 Direct numerical simulation of high aspect ratio spanwise-aligned bars. *Journal of Fluid Mechanics* **843**, 126–155.

Michalke, A. 1972 The instability of free shear layers. *Progress in Aerospace Sciences* **12**, 213–216.

Mittal, R. & Iaccarino, G. 2005 Immersed boundary methods. *Annual Review of Fluid Mechanics* **37**, 239–261.

Moin, P. & Mahesh, K. 1998 Direct numerical simulation: a tool in turbulence research. *Annual review of fluid mechanics* **30** (1), 539–578.

Moser, R. D., Kim, J. & Mansour, N. N. 1999 Direct numerical simulation of turbulent channel flow up to Re_τ= 590. *Physics of fluids* **11** (4), 943–945.

Nepf, H. M. 2012 Flow and transport in regions with aquatic vegetation. *Annual Review of Fluid Mechanics* **44** (1), 123–142.

Nepf, H. M., Ghisalberti, M., White, B. & Murphy, E. 2007 Retention time and dispersion associated with submerged aquatic canopies. *Water Resources Research* **43** (4).

Nikuradse, J. 1933 *Laws of flow in rough pipes*. National Advisory Committee for Aeronautics Washington, DC.

Nordström, J., Mattsson, K. & Swanson, C. 2007 Boundary conditions for a divergence free velocity–pressure formulation of the navier–stokes equations. *Journal of Computational Physics* **225** (1), 874–890.

Orlandi, P. & Leonardi, S. 2006 DNS of turbulent channel flows with two-and three-dimensional roughness. *Journal of Turbulence* **7**, N73.

Perot, J. B. 1993 An analysis of the fractional step method. *Journal of Computational Physics* **108** (1), 51–58.

Pietri, L., Petroff, A., Amielh, M. & Anselmet, F. 2009 Turbulence characteristics within sparse and dense canopies. *Environmental fluid mechanics* **9** (3), 297.

Placidi, M. & Ganapathisubramani, B. 2018 Turbulent flow over large roughness elements: effect of frontal and plan solidity on turbulence statistics and structure. *Boundary-layer meteorology* **167** (1), 99–121.

Poggi, D. & Katul, G. G. 2008 The effect of canopy roughness density on the constitutive components of the dispersive stresses. *Experiments in Fluids* **45** (1), 111–121.

Poggi, D., Porporato, A., Ridolfi, L., Albertson, J. D. & Katul, G. G. 2004 The effect of vegetation density on canopy sub-layer turbulence. *Boundary-Layer Meteorology* **111** (3), 565–587.

Py, C., De Langre, E. & Moulia, B. 2006 A frequency lock-in mechanism in the interaction between wind and crop canopies. *Journal of Fluid Mechanics* **568**, 425–449.

Raupach, M. R., Antonia, R. A. & Rajagopalan, S. 1991 Rough-wall turbulent boundary layers. *Applied mechanics reviews* **44** (1), 1–25.

Raupach, M. R., Finnigan, J. J. & Brunet, Y. 1996 Coherent eddies and turbulence in vegetation canopies: the mixing-layer analogy. In *Boundary-Layer Meteorology 25th Anniversary Volume, 1970–1995*, pp. 351–382. Springer.

Raupach, M. R. & Shaw, R. H. 1982 Averaging procedures for flow within vegetation canopies. *Boundary-Layer Meteorology* **22** (1), 79–90.

Reynolds, W. C. & Hussain, A. K. M. F. 1972 The mechanics of an organized wave in turbulent shear flow. Part 3. theoretical models and comparisons with experiments. *Journal of Fluid Mechanics* **54** (2), 263–288.

Rogers, M. M. & Moser, R. D. 1994 Direct simulation of a self-similar turbulent mixing layer. *Physics of Fluids* **6** (2), 903–923.

Rosti, M. E., Brandt, L. & Pinelli, A. 2018 Turbulent channel flow over an anisotropic porous wall–drag increase and reduction. *Journal of Fluid Mechanics* **842**, 381–394.

Sadique, J., Yang, X. I. A., Meneveau, C. & Mittal, R. 2017 Aerodynamic properties of rough surfaces with high aspect-ratio roughness elements: effect of aspect ratio and arrangements. *Boundary-layer meteorology* **163** (2), 203–224.

Saffman, P. G. 1971 On the boundary condition at the surface of a porous medium. *Studies in applied mathematics* **50** (2), 93–101.

Schmid, P. J. & Henningson, D. S. 2012 *Stability and transition in shear flows*. Springer Science & Business Media.

Schoppa, W. & Hussain, F. 2002 Coherent structure generation in near-wall turbulence. *Journal of fluid Mechanics* **453**, 57–108.

Sharma, A. & García-Mayoral, R. 2018 Turbulent flows over sparse canopies. *Journal of Physics: Conference Series* **1001**, 012012.

Sharma, A., Gómez-de-Segura, G. & García-Mayoral, R. 2017 Linear stability analysis of turbulent flows over dense filament canopies. In *TSFP DIGITAL LIBRARY ONLINE*. Begel House Inc.

Sillero, J. A., Jiménez, J. & Moser, R. D. 2013 One-point statistics for turbulent wall-bounded flows at reynolds numbers up to $\delta^+ \approx 2000$. *Physics of Fluids* **25** (10), 105102.

Simens, M 2008 The study and control of wall bounded flows. PhD thesis, Universidad Politécnica de Madrid, Madrid.

Singh, R., Bandi, M. M., Mahadevan, A. & Mandre, S. 2016 Linear stability analysis for monami in a submerged seagrass bed. *Journal of Fluid Mechanics* **786**.

Slingsby, C. 2018 Moya power, https://www.moyapower.com/.

Smith, C. R. & Metzler, S. P. 1983 The characteristics of low-speed streaks in the near-wall region of a turbulent boundary layer. *Journal of Fluid Mechanics* **129**, 27–54.

Sundin, J. & Bagheri, S. 2019 Interaction between hairy surfaces and turbulence for different surface time scales. *Journal of Fluid Mechanics* **861**, 556–584.

Tanino, Y. & Nepf, H. M. 2008 Laboratory investigation of mean drag in a random array of rigid, emergent cylinders. *Journal of Hydraulic Engineering* **134** (1), 34–41.

Taylor, Z. J., Palombi, E., Gurka, R. & Kopp, G. A. 2011 Features of the turbulent flow around symmetric elongated bluff bodies. *Journal of Fluids and Structures* **27** (2), 250–265.

Tennekes, H. & Lumley, J. L. 1972 *A first course in turbulence*. MIT press.

Townsend, A. A. R. 1976 *The structure of turbulent shear flow*. Cambridge University Press.

Tuerke, F. & Jiménez, J. 2013 Simulations of turbulent channels with prescribed velocity profiles. *Journal of Fluid Mechanics* **723**, 587–603.

Turton, S. E., Tuckerman, L. S. & Barkley, D. 2015 Prediction of frequencies in thermosolutal convection from mean flows. *Physical Review E* **91** (4), 043009.

White, B. L. & Nepf, H. M. 2007 Shear instability and coherent structures in shallow flow adjacent to a porous layer. *Journal of Fluid Mechanics* **593**, 1–32.

Wong, C. Y. H., Trinh, P. H. & Chapman, S. J. 2019 Shear-induced instabilities of flows through submerged vegetation. *arXiv preprint arXiv:1904.11981* .

Yan, C., Huang, W., Miao, S., Cui, G. & Zhang, Z. 2017 Large-eddy simulation of flow over a vegetation-like canopy modelled as arrays of bluff-body elements. *Boundary-layer Meteorology* **165** (2), 233–249.

Yang, X. I. A., Sadique, J., Mittal, R. & Meneveau, C. 2016 Exponential roughness layer and analytical model for turbulent boundary layer flow over rectangular-prism roughness elements. *Journal of Fluid Mechanics* **789**, 127–165.

Yu, P., Zeng, Y., Lee, T. S., Bai, H. X. & Low, H. T. 2010 Wake structure for flow past and through a porous square cylinder. *International Journal of Heat and Fluid Flow* **31** (2), 141–153.

Yue, W., Parlange, M. B., Meneveau, C., Zhu, W., van Hout, R. & Katz, J. 2007 Large-eddy simulation of plant canopy flows using plant-scale representation. *Boundary-Layer Meteorology* **124** (2), 183–203.

Zampogna, G. A. & Bottaro, A. 2016 Fluid flow over and through a regular bundle of rigid fibres. *Journal of Fluid Mechanics* **792**, 5–35.

Zampogna, G. A., Pluvinage, F., Kourta, A. & Bottaro, A. 2016 Instability of canopy flows. *Water Resources Research* **52** (7), 5421–5432.